

Many-Body Perturbation Theory Algorithm for Multiband Systems, Floquet Moiré Materials and Beyond

by

©Ibsal Adel Thiab Assi

A thesis submitted to the School of Graduate Studies in partial fulfillment of the
requirements for the degree of

Ph.D.

Department of Physics and Physical Oceanography

Memorial University of Newfoundland

November 16, 2023

St. John's

Newfoundland

Abstract

In the first part of this work we introduce the symbolic determinant method (symDET) for constructing many-body perturbative expansions which is motivated by the Algorithmic Matsubara Integration (AMI) algorithm introduced recently [Taheridehkordi, A., Curnoe, S. H., & LeBlanc, J. P. F. PRB, 99(3), 035120, (2019)]. This algorithm is capable of performing both imaginary and real frequency calculations of physical observables at all coupling parameters, temperatures, etc., making it a promising tool for studying a variety of problems from lattice models to molecular chemistry problems. The current form of our symDET applies to both single and multiband systems with general two-body interactions, but it can be easily extended to beyond two-body interactions by the proper handling of Wick contractions. Although the computational expense increases for multiband problems at higher order perturbation theory, our algorithm is still parallelizable. Furthermore, optimizations still exist. One way could be by following the steps of the connected determinant method (cDET) [R. Rossi, Phys. Rev. Lett. 119, 045701 (2017)] and the minimal determinant algorithms introduced recently [Šimkovic IV, F., & Ferrero, M. PRB, 105(12), 125104, (2022)]. As an illustration, we applied symDET to a variety of problems such as the hydrogen molecule with 2 and 10 bases, the Hubbard dimer model which is an effective 4 bands system, and the Hubbard model with an effective doubly degenerate band.

In the second part of this thesis, we review the Floquet method which is used

to study non-equilibrium systems. In particular, we focused on its application to twisted multilayered systems for which the appearance of flat bands at magic angles is a sign of interesting physical states, such as superconductivity which can be observed experimentally in those systems. As an illustration, we applied this method to twisted bilayer and trilayer graphene systems. For the first example, we considered the twisted trilayer graphene (TTLG) system with different types of light applied vertically onto layers, mainly circularly polarized light and light from a waveguide, and we focused on the topological maps where we found that for the special case of ABC stacking, those maps are dependent on the handedness of the circularly polarized light. This dependence can be captured via optical conductivity measurements. Secondly, we studied the twisted bilayer graphene (TBLG), with the usual tight binding Hamiltonian together with interlayer hopping interactions, and then on top of that we included the Haldane interaction. The application of circularly polarized and waveguide lights were discussed where we considered the effects of light on the band structure of this model. For the Haldane TBLG we found that the band structure depends on the polarization of the incident light, something that was observed in the TTLG with ABC stacking but never seen in the usual TBLG system, hence we owe that to time reversal symmetry breaking.

Lastly, we discuss the possible extensions of symDET to bosonic systems and the possible future application of symDET to twisted multilayer systems that has rich physics with a wide range of applications.

Acknowledgements

First, I would like to thank my PhD supervisor Dr. James LeBlanc for his guidance throughout my program. It was a pleasure working with him and being a member of his group. I indeed learned a lot of things that motivated me for doing further research in the future.

Second of all, I would like to thank Memorial University of Newfoundland and the physics department for granting me the fund to pursue my degree, without their help I wouldn't be able to pursue my program and achieve my goals. Also, Memorial University offered us the good atmosphere during the unprecedented times during the pandemic by providing various resources that helped us go through these difficult moments. I appreciate everything this university have offered and I will always be proud to be one of its students.

Lastly, I extend my appreciation to my family for their continuous support throughout the past six years of me being away from them. Without their encouragements, I would not be able to achieve my goals and finish my PhD program. They have played a central role in making me who I'm today. The words cannot describe how much I'm thankful to them, I can only say I'm so proud to be part of my family.

Table of Contents

Abstract	ii
Acknowledgments	iv
Table of Contents	vii
List of Tables	viii
List of Figures	xiv
List of Abbreviations and Symbols	xiv
1 Introduction	1
2 Symbolic Determinant Method for Equilibrium Many-Body Problems	8
2.1 Basic Concepts for Quantum Many-Body Theory	8
2.1.1 The Schrodinger Equation	9
2.1.2 Second Quantization	10
2.1.3 Real-Time Green's Function	12
2.1.4 Imaginary-Time Green's Function	14
2.1.5 Perturbative Expansion	15

2.1.6	Wick's Theorem	16
2.1.7	Feynman Diagrams	17
2.2	Algorithmic Matsubara Integration	20
2.3	Symbolic Determinant Construction of Perturbative Expansions . . .	24
2.3.1	Motivations: Why symDET?	24
2.3.2	General Model	26
2.3.3	Wick Contractions via Determinant	26
2.3.4	Symbolic Fourier Transform	29
2.3.5	Minimal Sampling of Internal Variables	30
2.4	Applications to Fermionic Systems	31
2.4.1	Molecular Chemistry Problems: H_2	31
2.4.2	The Dimer Model	34
2.4.3	Single-Band Hubbard Model on Square Lattice	38
2.5	Summary	39
3	Floquet Theory for Driven Layered Twisted Systems	42
3.1	Review	42
3.2	Floquet Engineering and Topological Maps in Twisted Trilayer Graphene (TTLG)	46
3.2.1	Why TTLG?	46
3.2.2	Equilibrium Model	47
3.2.3	TTLG Under the Influence of Circularly Polarized Light . . .	52
3.2.3.1	Numerical results of the band structure using the quasi- operator approach	52
3.2.3.2	Band structure via the Van-Vleck approximation . .	55
3.2.3.3	The rotating frame effective Hamiltonian	56
3.2.3.4	Topological phase diagrams	61

3.2.3.5	Experimental proposal	64
3.2.4	The Effect of Waveguide Light on TTLG	67
3.2.4.1	Numerical calculations of dispersions	67
3.2.4.2	Exact versus Van-Vleck results	69
3.3	Haldane-Moiré Model in Driven Twisted Bilayer Graphene (TBLG) .	73
3.3.1	Importance of Haldane Model	73
3.3.2	The Model	75
3.3.3	The Effect of Circularly Polarized Light	78
3.3.4	Waveguide Light	78
3.4	Summary	80
4	Conclusions and future Work	83
A	Steps of the SFT	87
A.1	Sorting Wick's contractions	87
A.2	Array representation of the non-interacting Green's function	88
A.3	The Symbolic Fourier Transform (SFT)	89
B	Fourier Transform of Haldane-Moiré Bilayer Graphene Hamiltonian	93
	Bibliography	94

List of Tables

3.1	Color codes for the topological phase diagrams Figs. 3.8&3.10. Here, the term v represents a band closing that was confirmed up to numerical accuracy. The term ν corresponds to a Chern number that did not converge even when more than 10^4 k points were used in the Chern number computation. RH: right-handed polarized light, and LH: left handed polarized light.	65
-----	---	----

List of Figures

2.1	A draw map of the Feynman diagram setup for first order (top row) and second order (bottom row) perturbation theory.	18
2.2	Flow chart of the symDET steps. First, contractions are generated from the determinant of Eq. 2.54, then the SFT is used to filter contractions and provide the correct conserving labels to contractions that are equivalent to connected diagrams. Thirdly, we sample over all internal non-frequency variables and perform the nested Matsubara summations via the AMI. At this stage, analytic expressions are stored and if real frequency calculations are needed, the analytic continuation is performed exactly from those expressions.	32
2.3	(a) and (b) The real and imaginary parts of the self-energy for H_2 in the STO-6g basis with external band indices $a_{\text{ex}} = b_{\text{ex}} = 0$. (c) and (d) plots of the real and imaginary parts of Σ^{H_2} for $a_{\text{ex}} = b_{\text{ex}} = 1$. Here $\beta = 50.0$. The dashed curves are the corresponding data obtained in Ref. 1	35
2.4	(a) and (b) the real and imaginary parts of Σ_{00} , while (c) & (d) are the components of the self-energy for the second band for H_2 (in the STO-6g basis) on the real frequency axes. Here the regulator is $\Gamma = 0.05$	36

2.5	The spectral function for H_2 in the STO-6g basis is truncated at 4th order. The inset data is a zoom in of the extra peaks with lower intensity. Here the regulator 0.05.	37
2.6	The self-energy for H_2 in the cc-pVDZ basis versus the Matsubara frequency with $\beta = 50.0$. (a) The real part of the self-energy components $(0, 0)$ and $(1, 1)$ truncated at second ($n_{\max} = 2$) and third ($n_{\max} = 3$) orders, and (b) are the imaginary counterparts.	37
2.7	(a) and (b) the real and imaginary parts of the diagonal elements of the self-energy matrix for $n_{\max} = 2, 3$ for the Hubbard Dimer model (Eq.2.58). Here we took $t = 1.0$, $U = 2.5$, $\mu = 0.70$, $H = 0.30$, $U_a = 0.50$, $\mu_a = 0.20$, $H_a = 0.030$, and $\beta = 2.0$	38
2.8	(a) The real part of the (spin up) self-energy of the two dimensional Hubbard model for $t = 1.0$, $U = 3.0$, $\beta = 8.33$, $\vec{k} = (0, \pi)$, and at different values of μ as indicated, and (b) are the imaginary counterparts. 40	40
2.9	(a) and (b) the real and imaginary parts of the self-energy (truncated at third order) versus the real frequency for the 2D Hubbard model evaluated for the parameters choice: $U = 3t = 3.0$, $\beta = 8.33$, and $\vec{k} = (0, \pi)$ with different values of μ as indicated. We took a Monte-Carlo sample of size 1×10^8 and the regulator $\Gamma = 0.2$	40
3.1	(a) The moiré Brillouin zone for a twisted trilayer graphene (TTLG) system with only one layer twisted. (b) Schematic plot of the TTLG system for the AAA stacking with middle layer twist showing the moiré pattern [2].	48

3.2 Band structure of the TTG with equilibrium Hamiltonian (Eq. 3.8) top layer twisted (top row) and middle layer twisted (bottom row) with twist angle $\theta = 1.6^\circ$. (a,c) Starting from AAA stacking and (b,d) starting from ABC stacking [2]. 51

3.3 Band structure (left column) for TTLG driven by circularly polarized light. (a) Starting with AAA stacking with TTLG and parameters $(\theta, Aa_0, \omega) = (1.8^\circ, 0.25, 2\gamma)$, and (b) the ABC with TTLG and $(\theta, Aa_0, \omega) = (1.0^\circ, 0.15, 3\gamma)$. In the above plots, the dash-dotted lines represent the undriven case and the solid lines represent the driven case. The corresponding density of states plots (DOS) are on the right column rescaled by $D_M(E)$ which is the maximum value of the DOS of the driven case [2]. 53

3.4 Reproduction of Fig. 3.3 for the case of middle layer twist (MLT). (a) AAA stacking with $(\theta, Aa_0, \omega) = (1.6^\circ, 0.15, 3\gamma)$, and (b) ABC configuration for the parameters $(\theta, Aa_0, \omega) = (1.6^\circ, 0.15, 3\gamma)$ [2]. 54

3.5 Comparison between the exact quasi-energies and the energies from the VVA for the band structure of the TTLG with AAA stacking and middle layer twisted, driven by circularly polarized light $\theta = 1.6^\circ$, $Aa_0 = 0.4$, and $\Omega = 3\gamma$. Here solid lines represent the VVA results and the dashed lines are the exact quasi-energies Eq. 3.6. 57

3.6 Comparison between the exact quasi-energies and the energies from the rotating frame Hamiltonians for the band structure of the TTLG with AAA stacking and middle layer twisted, driven by circularly polarized light $\theta = 1.6^\circ$, $Aa_0 = 0.4$, and $\Omega = 3\gamma$. Here, the solid lines represent rotating frame results while the dashed lines represent the *exact* results. 60

3.7	Plot of relative error for the gap at the K_1 symmetry point for the TTG system with AAA stacking and middle layer twisted driven by circularly polarized light (a) as function of Aa_0 , with $\theta = 1.6^\circ$, and $\Omega = 2\gamma$, (b) and as a function of ω/γ with $Aa_0 = 0.5$	61
3.8	(Color online) The topological phase diagrams for the TTG system for a range of values Aa_0 and the twist angle θ with $\omega = 2\gamma$. (a) AAA stacking and top layer twist, (b) ABC stacking with top layer twisted, (c) AAA stacking with middle layer twisted, and (d) ABC stacking with middle layer twisted. Each color represents a set of values for the Chern numbers of the central six bands as indicated in Table. 3.1.	63
3.9	Band structure for the ABC MLT showing the six bands labeled $c_1 \rightarrow c_6$. Parameters $Aa_0 = 0.26375$, $\theta = 1.65^\circ$ and $\omega = 2\gamma$ were chosen for the plot.	66
3.10	(Color online) The topological phase diagrams for the TTG system with ABC stacking and top layer twisted where (a) for the left-handed circularly polarized light and (b) the right-handed circularly polarized light, where we took $\omega = 2\gamma$. For color codes, please refer to Table. 3.1.	67
3.11	Sketch of a two laser procedure to create light-induced topological boundaries in ABC TTLG samples.	68
3.12	Left Column: Band structure of the TTG driven by waveguide light with $Aa_0 = 0.3$. (a) The AAA stacking with TLT and $(\theta, \omega) = (2.000^\circ, 2\gamma)$, (b) the ABC configuration with TLT and $(\theta, \omega) = (1.040^\circ, 2\gamma)$. The solid lines are for the driven and the dash-dotted lines for the un-driven case. Right Column: The density of states plots associated with the configurations on the left column rescaled by the maximum value $D_M(E)$ of the driven case.	70

3.13	Left Column: Band structure of the TTG driven by waveguide light with $Aa_0 = 0.3$. (a) AAA with MLT and parameters $(\theta, \omega) = (1.450^\circ, 3\gamma)$, and (b) the ABC stacking with MLT and $(\theta, \omega) = (1.157^\circ, 2\gamma)$. The solid lines are for the driven and the dash-dotted lines for the undriven case. Right Column: The density of states plots associated with the configurations on the left column rescaled by the maximum value $D_M(E)$ of the driven case.	71
3.14	Plot of velocity as function of $1/\theta$ for the center bands near K1 in the twisted TTG system driven by waveguide light compared with the undriven case with $Aa_0 = 0.3$, and $\Omega = 3\gamma$. (a) Starting from AAA stacking middle layer twist (b) starting from ABC stacking middle layer twist. Here, \tilde{v}_x is the velocity at $\theta = 2.0^\circ$	72
3.15	Comparison of the band structure for TTLG with ABA stacking and middle layer twisted driven by waveguide light with $\theta = 1.3^\circ$, $Aa_0 = 0.8$, and $\Omega = 1.5\gamma$. obtained via the quasi-energy operator Eq. 3.6 (dashed lines) versus the zeroth order van Vleck Hamiltonian H_0 (solid lines).	74
3.16	The second nearest neighbor Haldane interaction between the A and B sites in honeycomb lattice.	77
3.17	The equilibrium band structure of TBLG with Haldane interaction (a) $M = 9\sqrt{3}t_2/4$ and (b) $M = 3\sqrt{3}t_2$. Here we took $t_1 = 2360$, $t_2 = 0.05t_1, \theta = 1.05$, and $w_0 = w_1 = 110$	77

3.18 The band structure of TBLG with Haldane interaction showing the static case (solid black lines) versus the case with circularly polarized light (dashed blue lines). (a) $M = 9\sqrt{3}t_2/4$ with RH light, (b) $M = 9\sqrt{3}t_2/4$ with LH light, (c) $M = 3\sqrt{3}t_2$ for RH light and (c) $M = 3\sqrt{3}t_2$ with LH light. Here we took $Aa_0 = 0.4$, $\omega = 2t_1$ and the other values as in Fig. 3.2. 79

3.19 The band structure of TBLG with Haldane interaction for the static case (solid black lines) versus that with waveguide light (dashed blue lines) (a) $M = 9\sqrt{3}t_2/4$ and (b) $M = 3\sqrt{3}t_2$. Here we took $t_1 = 2360$, $t_2 = 0.05t_1$, $\theta = 1.05$, $w_0 = w_1 = 110$, $Aa_0 = 0.4$, and $\omega = 1.5t_1$ 80

List of Abbreviations and Symbols

c_a^\dagger	Fermionic creation operator in the state a
c_a	Fermion annihilation operator in the state a
a_λ^\dagger	Boson creation operator in the state λ
a_λ	Boson annihilation operator in the state λ
ε_a	Fermion/Boson energy in the state a
Σ_{ab}	Self-energy
ω_n	Matsubara frequency
$A(\omega)$	Spectral function
$g_{ab}(i\omega_n)$	Non-interacting Green's function
$G_{ab}(i\omega_n)$	Interacting Green's function
STF	Symbolic Fourier Transformation
AMI	Algorithmic Matsubara Integration
TTLG	Twisted Trilayer Graphene
TBLG	Twisted Bilayer Graphene

Chapter 1

Introduction

In condensed matter systems, collective interactions between the constituent particles or ions give rise to interesting physical properties that make the bulk material hosting these characteristics useful in technology, medicine, and other parts of everyday life. For example, superconductivity (SC) is a state for which the resistance of a conductor drops to zero at certain critical temperatures. According to Bardeen–Cooper–Schrieffer (BCS) theory, the superconducting state is due to the formation of electron pairs via electron-phonon interactions (a.k.a. Cooper pairs) [3–5]. Intensive studies have been ongoing from both experimental and theoretical sides to better understand this behaviour, and most importantly the search for room temperature superconductors for further technological and economical benefits to mankind [6]. For instance, recent discovery of superconductivity of lanthanum hydride at relatively high temperature of 250 K and high pressure of 150 GPa motivates a search for similar behaviour to occur at room temperatures and pressures [7–11]. Collective phenomena occur in other condensed matter systems such as, but not limited to, spin liquid [12–14], spin ice [13, 15, 16], superfluidity [17, 18], insulating state [17, 18], and ferromagnetism [19–21].

Exact solutions of condensed matter problems are very useful in studying materials properties and help us to gain a deep theoretical understanding of microscopic interactions between the constituent particles (e.g. electrons) that lead to different macroscopic behaviours and the possible limitations of the model under study, especially when accompanied by experimental data. Examples of exactly solvable models include the one-dimensional Hubbard model [22], the 1D $t - J$ model [23], and the Kitaev honeycomb model [24].

Most of the realistic condensed matter models in two and three dimensions lack exact solutions. Those limitations are due to the fact that condensed matter systems contain an exponentially large number of particles or ions, whose quantum degrees of freedom make the full Hilbert space too large to obtain exact solutions within the mathematical methods that exist today. Hence the need of approximate numerical approaches to tackle the properties of the physical system of interest.

First, we start with condensed matter systems at equilibrium. Different numerical methods have arisen to treat such systems where the success of some can be limited. The simplest among these is mean field theory (MFT), where each ion in the system is assumed to experience a mean field which then turns the many-body problem into an effective single particle model. Although MFT seems to be an oversimplification, in fact it is useful to at least give qualitative predictions, such as the ferromagnetic to paramagnetic phase transition in the 3D Ising model but fails to predict the exact transition temperature [25]. In other situations the effective one-particle mean field is dynamical, like the case of Weiss treatment of the Ising model [26].

An improved version of MFT is called the dynamical mean field theory (DMFT). In DMFT, local quantum fluctuations are included, which provides a more realistic approach to the physical systems of interest [27–30]. Other iterative schemes were built on top of these approximations, such as the dynamical cluster approximation

(DCA) where short range correlations were included [31–33]. Some numerical methods such as exact diagonalization are only reachable for finite system sizes due to the large number of degrees of freedom and this becomes a bigger obstacle when one moves from one-dimensional to higher dimensional systems [34–37].

For one dimensional problems, one of the most reliable methods today is the density matrix renormalization group (DMRG) introduced in the 1990s by S. R. White [38–40]. DMRG uses exact diagonalization coupled with entanglement as the basis for its algorithm to compute the physical observables of several one dimensional systems [41–43]. The method then was extended to study two dimensional systems [44–46], however its accuracy might be low for some systems [47].

Alternatively, one could rely on other methods to study two dimensional systems such as the projected entangled pair states (PEPS) [48–53] and the multiscale entanglement renormalization ansatz (MERA) [54–56]. The computational cost of the MERA is bigger than that of the PEPS but the advantage of MERA over PEPS is that it allows efficient and accurate evaluation of different observables of interest (refer to Table 1 in [47]). The bigger field that includes the PEPS, MERA, the DMRG and other tensor structures is called tensor networks (TNs) [57–63].

Many body perturbation theory (MBPT) is one of the famous methods that is used to study physical systems in arbitrary dimension in the thermodynamic limit. The basic idea revolves around Wick’s theorem where all the elements of the perturbative series (aka Wick contractions) are evaluated independently [64–66]. Feynman diagrams are graphical representation of those contractions which rely on the basics of graph theory to evaluate the corrections to the physical observable of interest at any arbitrary perturbation order cutoff [67, 68]. Graphically, Wick contractions could be represented by either a connected graph or a disconnected one. However, it turns out that only connected diagrams contribute to the perturbative series. Nonetheless, the

number of contractions that correspond to connected graphs grows exponentially and factorially with perturbation order putting some limitations on the highest order we can reach via the available computational tools. Approximations were also introduced in this regard where the focus is on including certain types of diagrams such as the random phase approximation (RPA) where only bubble diagrams are included, and then the perturbative series computed to an infinite order [69–72] and the GW approximation where the self-energy is approximated in terms of the screened potential W and the single-particle propagator G [73, 74].

One of the ways to treat MBPT numerically is via diagrammatic Monte Carlo (DiagMC) methods which have been used to solve variety of physical systems of interest [75–78]. However, DiagMC methods suffer from the famous sign problem [75], which was suppressed recently by the development of determinant methods [79–81]. Several optimizations have been introduced to overcome the factorial scaling of diagrammatic expansions [1, 82–84]. Those methods, however, require numerical schemes to calculate the dynamic properties of the system on the real frequency axis [85, 85–87].

The recently developed algorithmic Matsubara integration (AMI) algorithm allows the performance of analytic continuation analytically, hence avoiding ill-posed numerical analytical continuation schemes [88, 89]. The AMI has been used to solve different problems such as the two-dimensional Hubbard model [90, 91], and the uniform electron gas [92, 93]. Following the development of the AMI, we developed an algorithm that performs the MBPT symbolically at all coupling constants, temperatures, and at an arbitrary perturbation order. We refer to this algorithm as the symbolic determinant (symDET) method [94]. Our algorithm generates Wick contractions from the determinant structure where we then perform the symbolic Fourier transformation (SFT) after which the AMI is used to perform the summations over

the internal Matsubara frequencies. Between the SFT and the AMI, optimal sampling of internal variables such as band indices, momenta, etc., is performed. The structure of symDET allows it to study generally any multiband system ranging from molecular chemistry problems to a variety of lattice models. Despite the fact that the factorial cost of evaluating Wick contractions is not lifted in the current status of the symDET structure, our method is parallelizable and one can run the codes on more CPU units and for a longer time to perform higher order calculations. However, we should stress that optimizations are always possible, but this is beyond the scope of this thesis.

In the second part of this thesis, we focus on a particular class of non-equilibrium systems (NES). Generally speaking, the main difficulty in the NES is that computing the time evolution operator is extremely hard, hence the difficulty in understanding the physics of those systems theoretically. Despite that, non-equilibrium phenomena are of great interest due to several factors such as the ability to control material properties [95, 96], and the emergence of interesting phases of matter such as superconductivity [97], time crystals [98, 99], topological Floquet phases [100, 101], and others [102–104]. Thus, several theoretical methods were developed to study those systems. For example, tensor networks were used to variety of NES such as the classical 2D systems [105], the Anderson impurity problem [106], XXZ Heisenberg chains [107], and others [108–111]. We should note that some of the previously mentioned methods also have extensions to non-equilibrium problems such as the density matrix renormalization group which was also applied to time-dependent Hamiltonians [112–114]. Several experimental techniques were developed to study those interesting properties of NES for practical applications [95, 115–117]. In practice, equilibrium systems can be brought to non-equilibrium via an application of an external field such as illumination with a laser light which can lift the system to an entirely new phase [118]. Clearly, NES share more physics than their equilibrium counterparts, yet are difficult

to understand from the theoretical point of view due to the fact that solving the problem requires the knowledge of the full Hilbert space which is impossible for most of the condensed matter systems. Hence, approximation methods are necessary.

A very interesting class of non-equilibrium systems are the periodically driven materials where the model Hamiltonians are periodic and thus can be described by Floquet theory [119]. In this theory one basically describes such systems via time-independent Hamiltonian known as Floquet Hamiltonian H_F which is used to describe the physics of the system at experimental time scale. We should note that obtaining such effective Hamiltonian is generally difficult, thereby approximation techniques have been developed to estimate H_F [120–124]. Despite this difficulty, it is worth the effort to engineer an effective H_F that can model interesting physical behaviours such as Floquet topological insulators [125–128], or it could be used to describe new phases that don't occur in equilibrium systems [98, 99].

Recently, experimental tools were developed to manufacture a special class of condensed matter system that is designed precisely and was found to host a rich class of physical phenomena. These systems are referred to as Van der Waals heterostructures [129, 130]. The famous example is the twisted bilayer graphene (TBLG) which is a test bed for strongly correlated physics phenomena [131–140]. Certain choices of the twist angle (known as the magic angle) results in the emergence of flat bands which signals the dominant interaction effects occurring in those systems [141, 142]. Furthermore, it was found that the application of circularly polarized light to TBLG system could induce topological phase transitions and flat bands at higher magic angles observed in the otherwise non-driven system [143, 144]. Magic angles can be tuned via the application of waveguide light on the TBLG planes [145]. We should stress that other similar systems host such properties such as the transition metal dichalcogenide homobilayer [146, 147], and multilayered graphene systems [148, 149].

All of these interesting physical properties found in Van der Waals systems motivate both experimentalists and theorists to investigate such systems thoroughly from both view points, for a better understanding of the corresponding many-body phenomena and also to make use of these systems for practical applications such as in technology and industry.

The thesis is organized as follows. In Chapter 2, we introduce our symDET algorithm in deep details and we then show variety of applications to molecular and lattice models. The material in Ch. 2 including figures is based on results from our article [Assi, I., & LeBlanc, J. P. F. (2023). Symbolic determinant construction of perturbative expansions. arXiv preprint arXiv:2305.09103.] and follows closely the text within. Next, in Chapter 3, we apply Floquet theory to different graphene systems. In particular, we discuss the effect of both circularly polarized light and waveguide light on these systems and we compute the corresponding topological maps in the case of circularly polarized light for the twisted trilayer graphene system. Moreover, we studied the TBLG system with the inclusion of Haldane interactions under the influence of light. The material in Section 3.2 is based on our published work [Assi, I. A., LeBlanc, J. P. F., Rodriguez-Vega, M., Bahlouli, H., & Vogl, M. (2021); Floquet engineering and nonequilibrium topological maps in twisted trilayer graphene; Physical Review B, 104(19), 195429.]; and follows closely the text within. Finally, we give our conclusions and future work in Chapter 4.

Chapter 2

Symbolic Determinant Method for Equilibrium Many-Body Systems

This chapter is organized as follows. In Section 2.1 we review the basic concepts in many-body physics that are important for many-body perturbation theory (MBPT). Next, we review the elements of the algorithmic Matsubara integration (AMI) tool in Section 2.2 which is one of the main parts of our symDET algorithm discussed in Section 2.3. Moreover, we apply our algorithm to a variety of problems in Section 2.4. Finally, we provide a summary in Sec. 2.5.

2.1 Basic Concepts for Quantum Many-Body Theory

This section is organized as follows: In Sec. 2.1.1 we review Schrodinger equation and it's importance in quantum physics. Next, we discuss second quantization and how one can express the general two-body interaction Hamiltonians in terms of Fock-space creation and annihilation operators in Sec. 2.1.2. Thirdly, we go through the

definitions of real and imaginary time Green functions in Sections 2.1.3 and 2.1.4. Furthermore, we present the iterative procedure to obtain solutions of the interacting Green's function in Sec. 2.1.5. Finally, in Sections 2.1.6 & 2.1.7 we go through Wick's theorem and Feynman diagrams as the usual (alternative) methods used to evaluate the time-ordered averages appear in the many-body perturbative series.

2.1.1 The Schrodinger Equation

The dynamics of a system of particles within the quantum theory is governed by the time-dependent Schrodinger's equation,

$$\hat{\mathcal{H}}|\Psi\rangle = i\hbar\frac{\partial}{\partial t}|\Psi\rangle, \quad (2.1)$$

where $\hat{\mathcal{H}}$ is the Hamiltonian operator that models the system of interest, $|\Psi\rangle$ is the wavefunction which signifies the state that the system pertains to, and $\hbar = 6.582119569 \times 10^{-16}$ eV · s is the reduced Planck's constant. The general solution of the above equation for time-independent Hamiltonians is of the form

$$|\Psi(t)\rangle = \sum_n c_n e^{-iE_n t/\hbar} |\phi_n\rangle, \quad (2.2)$$

where $|\phi_n\rangle$ is an eigenstate of the stationary Schrodinger equation,

$$\hat{\mathcal{H}}|\phi_n\rangle = E_n |\phi_n\rangle, \quad (2.3)$$

with E_n being the quantized energy eigenvalue. For orthonormal states $\{|\phi_n\rangle\}$, i.e. $\langle\phi_n|\phi_m\rangle = \delta_{n,m}$, the requirement that the full wavefunction $|\Psi\rangle$ is normalized results in the condition

$$\sum_n |c_n|^2 = 1. \quad (2.4)$$

where $|c_n|^2$ represents the probability that the system is found in the state $|\phi_n\rangle$ with energy E_n . We should note in general, one can expand the solutions in terms of any complete basis and not just the eigenstates of the stationary problem. Once obtained, the wavefunction can be used to calculate the average of any observable \mathcal{O} via

$$\langle \mathcal{O} \rangle = \langle \Psi | \mathcal{O} | \Psi \rangle. \quad (2.5)$$

For the majority of condensed matter problems, it is impossible to solve the wave equation due to the large number of particles and the associated degrees of freedom, making it hard to tackle with the available mathematical tools and the computer resources. Hence, it is necessary to look for approximate numerical solutions that help us in achieving our goal.

2.1.2 Second Quantization

The first quantization is usually referred to the quantum theory described in the previous section where the energy of the particle (E_n) is quantized. However, when extending the theory to fields rather than particles only, the quantization of fields is referred to as second quantization.

For an N particle interacting system, the N -particle wavefunction can be written in symmetrized/antisymmetrized form of single particle states for bosons/fermions. This representation is cumbersome to deal with due to the complexity of the full wavefunction as N increases in a real condensed matter system. Thus, to reduce this complexity one deals with an alternative basis, namely the particle number representation where the states belong to Fock space. The first step to achieve this is by introducing creation and annihilation operators for fermions and bosons. First, for a

system of fermions, those operators (c_s^\dagger and c_s respectively) are defined as

$$c_s^\dagger |0, \phi_{s_1}, \phi_{s_2}, \dots, \phi_{s_N}\rangle = |\phi_s, \phi_{s_1}, \phi_{s_2}, \dots, \phi_{s_N}\rangle. \quad (2.6)$$

which creates a Fermion in state s provided that $s \neq s_j$, otherwise the action of this operator on the state ket is zero. The operator

$$c_s |\phi_s, \phi_{s_1}, \phi_{s_2}, \dots, \phi_{s_N}\rangle = |\phi_{s_1}, \phi_{s_2}, \dots, \phi_{s_N}\rangle, \quad (2.7)$$

annihilates a fermion in the state s . Those operators satisfy the anti-commutation relations

$$\{c_p, c_q\} = \{c_p^\dagger, c_q^\dagger\} = 0, \quad \{c_p, c_q^\dagger\} = \delta_{p,q}, \quad (2.8)$$

where $\{A, B\} = AB + BA$. The basis state of fermion Fock space takes the general form $|n_1, n_2, \dots, n_N\rangle$, with $n_j = \{0, 1\}$.

On the other hand, for bosons, the corresponding creation and annihilation operators a_i^\dagger and a_i respectively, satisfy the commutation relations,

$$[a_p, a_q] = [a_p^\dagger, a_q^\dagger] = 0, \quad [a_p, a_q^\dagger] = \delta_{p,q}, \quad (2.9)$$

where $[A, B] = AB - BA$. However, unlike fermions, there is no limit on the number of bosons that can occupy the same state, i.e. for the basis ket $|n_1, n_2, \dots, n_N\rangle$, the occupancy per lattice site takes possible values $n_j = 0, 1, 2, \dots, N, \forall j$.

The general N -particle Hamiltonian with two-body interactions takes the form

$$\hat{\mathcal{H}} = \sum_{i=1}^N h(i) + \frac{1}{2} \sum_{i \neq j} V(i, j), \quad (2.10)$$

where $h(i)$ is the single particle Hamiltonian while $V(i, j)$ is the interaction potential

between the i^{th} and the j^{th} particles. The first term in the above Hamiltonian is expressed in the second quantization formalism as

$$\sum_{i=1}^N h(i) = \sum_{pq} \langle \phi_p | h | \phi_q \rangle c_p^\dagger c_q, \quad (2.11)$$

whereas the two-particle operator is expressed as

$$\frac{1}{2} \sum_{i \neq j} V(i, j) = \frac{1}{2} \sum_{klmn} \langle \phi_k \phi_l | V | \phi_m \phi_n \rangle c_k^\dagger c_l^\dagger c_n c_m. \quad (2.12)$$

The final expression of the Hamiltonian $\hat{\mathcal{H}}$ in the second quantization form is the type of Hamiltonian of interest to many applications.

In the case of lattice systems, the simplest form of such generic Hamiltonian is the Hubbard model which takes the form

$$\hat{\mathcal{H}} = -t \sum_{i\sigma} [c_{i,\sigma}^\dagger c_{i+1,\sigma} + h.c.] + U \sum_i \hat{n}_{i\uparrow} \hat{n}_{i\downarrow}, \quad (2.13)$$

which represents local Coulomb interactions between electrons in the lattice. Here t is the hopping amplitude between two sites and the onsite interaction of strength U is given by the second term of the Hamiltonian. Here, $h.c.$ stands for the Hermitian conjugate. The number operator $\hat{n}_{i\sigma} = c_{i\sigma}^\dagger c_{i\sigma}$ represents the number of Fermions at the i^{th} site with spin $\sigma = \{\uparrow, \downarrow\}$.

2.1.3 Real-Time Green's Function

The spectrum of a many body system is almost continuous and the full wavefunction is very complicated, and it's not possible to obtain the analytic solution of the wave equation for most problems of interest. The most interesting thing we look for in a given many-body system at equilibrium is how the system responds to small per-

turbations such as an applied electric or magnetic field, or changes in the number of particles etc. The Green's function formalism fulfills such an investigation of the system's response. Considering a many-body system with Hamiltonian $\hat{\mathcal{H}}$ which is allowed to exchange energy and particles with a reservoir, with the system being at temperature $T = \beta^{-1}$, the system is then represented by the grand canonical ensemble where the effective Hamiltonian to be used is $\hat{\mathcal{H}} - \mu\hat{N}$, where μ is the chemical potential, $\hat{N} = c^\dagger c$ is the number operator. For any two operators \mathcal{O} and \mathcal{P} , their correlation function is defined as,

$$C_{\mathcal{O}\mathcal{P}}(t, t') = -i\langle \hat{\mathcal{T}}\mathcal{O}(t)\mathcal{P}(t') \rangle, \quad (2.14)$$

where $\hat{\mathcal{T}}$ is the time ordering operator, and the average of an observable \hat{x} is taken with respect to the grand canonical ensemble with partition function $\mathcal{Z}_G = \text{Tr} [e^{-\beta\hat{\mathcal{H}} + \beta\mu\hat{N}}]$, that is

$$\langle \hat{x} \rangle = \frac{\text{Tr} [e^{-\beta\hat{\mathcal{H}} + \beta\mu\hat{N}} \hat{x}]}{\mathcal{Z}_G}. \quad (2.15)$$

where time enters into these operators via Heisenberg representation with Hamiltonian $\hat{\mathcal{H}} - \mu\hat{N}$. For example, a single particle described by creation and annihilation field operators $\Psi_\sigma^\dagger(\vec{r})$ and $\Psi_\sigma(\vec{r})$, which create or annihilate a particle with spin σ at position \vec{r} , a special case of real-time correlation functions known as the Green's function is defined as

$$G_{\sigma\sigma'}(\vec{r}t, \vec{r}'t') = -i\langle \hat{\mathcal{T}}\Psi_\sigma(\vec{r}, t)\Psi_{\sigma'}^\dagger(\vec{r}', t') \rangle. \quad (2.16)$$

There are other definitions of Green's functions like the *retarded* and *advanced* Green's functions that are useful in certain calculations. Assuming $t > t'$, the physical meaning of the Green's function in Eq. 2.16 is the ensemble average of the propagation amplitude of a particle from a point (\vec{r}', t') at spin σ' to another point at (\vec{r}, t) with

a spin σ . The reverse argument follows when $t < t'$.

Another useful correlation function is the retarded Green's function defined as

$$G_{\sigma\sigma'}^R(\vec{r}t, \vec{r}'t') = -i\theta(t - t')\langle[\Psi_\sigma(\vec{r}, t), \Psi_{\sigma'}^\dagger(\vec{r}', t')]_{\pm}\rangle, \quad (2.17)$$

where $\theta(t - t')$ is 1 when its argument is positive and zero otherwise, and $[A, B]_{\pm} = AB \pm BA$ where the plus is for fermions and the minus for bosons. When this Green's function is transformed via Fourier transformation, its imaginary part gives the spectral density function, $A(\vec{k}, \omega) = -\text{Im}(G_{\sigma\sigma'}^R(\vec{k}, \omega))$.

2.1.4 Imaginary-Time Green's Function

In order to allow perturbative expansions for finite temperature Green's function of an interacting system, the imaginary time Green's functions is introduced,

$$\mathcal{G}_{\sigma\sigma'}(\vec{r}\tau, \vec{r}'\tau') = -\langle\hat{T}\Psi_\sigma(\vec{r}, \tau)\Psi_{\sigma'}^\dagger(\vec{r}', \tau')\rangle, \quad (2.18)$$

where $\{\tau, \tau'\}$ are the imaginary times which are obtained via the replacement $it \rightarrow \tau$ in the Heisenberg representation. For a time-independent and spin-independent interactions with translational symmetry, the imaginary-time Green's function is related to the particle number density as

$$n(\vec{r}) = \pm \sum_{\sigma} \mathcal{G}_{\sigma\sigma'}(\vec{r}\tau, \vec{r}\tau^+), \quad (2.19)$$

where the minus sign is for fermions and the plus sign is for bosons, and $\mathcal{G}_{\sigma\sigma'}(\vec{r}\tau, \vec{r}\tau^+)$ is called the same-time Green's function with $\tau^+ = \tau + 0^+$. Other physical quantities can also shown to be expressed in terms of such correlation functions. Denoting $\mathcal{G}(\vec{k}\sigma, i\omega_n)$ as the spatial and time Fourier transformation of the imaginary time Green's function,

with ω_n being the Matsubara frequency, then one can recover the retarded (real time) Green's function $G^R(\vec{k}\sigma, \omega)$ via analytic continuation $i\omega_n \rightarrow \omega + i0^+$. This analytic recovery of real time propagators is done exactly via the symDET algorithm as will be discussed later in Section 2.3.

2.1.5 Perturbative Expansion

First, we recall that the Heisenberg representation of an operator \hat{A} in the imaginary time (τ) frame is

$$\hat{A}_H(\tau) = e^{\hat{\mathcal{H}}\tau/\hbar} \hat{A} e^{-\hat{\mathcal{H}}\tau/\hbar}, \quad (2.20)$$

where $\hat{\mathcal{H}} = \mathcal{H}_0 + \hat{V}$ is the Hamiltonian of the interacting system with \mathcal{H}_0 being an exactly solvable Hamiltonian (aka the reference Hamiltonian), and \hat{V} is the interaction term. In the interaction picture, the operator \hat{A} is represented as

$$\hat{A}_I(\tau) = e^{\mathcal{H}_0\tau/\hbar} \hat{A} e^{-\mathcal{H}_0\tau/\hbar}. \quad (2.21)$$

To proceed further, we introduce the time evolution operator in the interaction representation

$$\hat{\mathcal{U}}(\tau, \tau') = e^{\mathcal{H}_0\tau/\hbar} e^{-\hat{\mathcal{H}}(\tau-\tau')/\hbar} e^{-\mathcal{H}_0\tau'/\hbar}, \quad (2.22)$$

Note that $\hat{\mathcal{U}}(\tau', \tau') = 1$ and $\hat{\mathcal{U}}(\tau, \tau'') = \hat{\mathcal{U}}(\tau, \tau') \hat{\mathcal{U}}(\tau', \tau'')$. This operator is very useful when expressing perturbative solution of the full propagator as will be shown later. Furthermore, the above operator satisfies the following differential equation

$$\frac{\partial}{\partial \tau} \hat{\mathcal{U}}(\tau, \tau') = -\frac{1}{\hbar} \hat{V}_I(\tau) \hat{\mathcal{U}}(\tau, \tau'). \quad (2.23)$$

where $\hat{V}_I(\tau) = e^{\mathcal{H}_0\tau/\hbar} \hat{V} e^{-\mathcal{H}_0\tau/\hbar}$ is the interaction representation of the perturbation \hat{V} . Without going to any further details, the iterative solution of the above differential

equation is [64]

$$\hat{\mathcal{U}}(\tau, \tau') = \sum_{n=0}^{\infty} \frac{(-1)^n}{n! \hbar^n} \int_{\tau'}^{\tau} d\tau_1 \int_{\tau'}^{\tau} d\tau_2 \cdots \int_{\tau'}^{\tau} d\tau_n \hat{\mathcal{T}} \left[\hat{V}(\tau_1) \hat{V}(\tau_2) \cdots \hat{V}(\tau_n) \right]. \quad (2.24)$$

Using $\tau = \beta \hbar$ and $\tau' = 0$, together with the imaginary time Green's function $\mathcal{G}(\vec{k}\sigma, \tau) = -\langle \hat{\mathcal{T}} c_{\vec{k}\sigma}(\tau) c_{\vec{k}\sigma}^\dagger(0) \rangle$, one finds [64]

$$\mathcal{G}(\vec{k}\sigma, \tau) = -\frac{\langle \hat{\mathcal{T}} \hat{c}_{\vec{k}\sigma}(\tau) \hat{c}_{\vec{k}\sigma}^\dagger(0) \hat{\mathcal{U}}(\beta \hbar, 0) \rangle_0}{\langle \hat{\mathcal{U}}(\beta \hbar, 0) \rangle_0}, \quad (2.25)$$

where $\hat{c}_{\vec{k}\sigma}(\tau)(\hat{c}_{\vec{k}\sigma}^\dagger(0))$ is the interaction representation of $c_{\vec{k}\sigma}(\tau)(c_{\vec{k}\sigma}^\dagger(0))$, and $\langle x \rangle_0$ represents the ensemble average of x with respect to \mathcal{H}_0 . Consequently, the perturbation series of the imaginary time Green's function is

$$\mathcal{G}(\vec{k}\sigma, \tau) = -\frac{\sum_{n=0}^{\infty} \frac{(-1)^n}{n! \hbar^n} \langle \int_0^{\beta \hbar} d\tau_1 \int_0^{\beta \hbar} d\tau_2 \cdots \int_0^{\beta \hbar} d\tau_n \hat{\mathcal{T}} \left[\hat{c}_{\vec{k}\sigma}(\tau) \hat{c}_{\vec{k}\sigma}^\dagger(0) \hat{V}(\tau_1) \hat{V}(\tau_2) \cdots \hat{V}(\tau_n) \right] \rangle_0}{\sum_{n=0}^{\infty} \frac{(-1)^n}{n! \hbar^n} \langle \int_0^{\beta \hbar} d\tau_1 \int_0^{\beta \hbar} d\tau_2 \cdots \int_0^{\beta \hbar} d\tau_n \hat{\mathcal{T}} \left[\hat{V}(\tau_1) \hat{V}(\tau_2) \cdots \hat{V}(\tau_n) \right] \rangle_0}. \quad (2.26)$$

In the next section, we will discuss how to evaluate the above averages using Wick's theorem where we end up with an infinite series in terms of the free particle propagators.

2.1.6 Wick's Theorem

In simple words, Wick's theorem targets ensemble averages of a time ordered product of operators and expresses them in terms of all possible contracted pairs. Basically, if we have n creation and n annihilation Fermionic operators appearing in an ensemble average as $\langle \hat{T} \prod_{i=1}^{i=2n} \mathcal{A}_i \rangle_0$ where \mathcal{A}_i can be a creation or an annihilation operator, then Wick's theorem states that this average can be expressed as a sum of all possible

pair-wise contractions [64]

$$\langle \hat{T} \prod_{i=1}^{i=2n} \mathcal{A}_i \rangle_0 = \sum_{\mathcal{P}} (-1)^{\chi_{\mathcal{P}}} \prod_{jk} \langle \hat{T} \mathcal{A}_j \mathcal{A}_k \rangle_0, \quad (2.27)$$

where $\chi_{\mathcal{P}}$ is the signature of the permutation \mathcal{P} of the Fermionic operators which is +1 for odd permutation and 0 for even rearrangements. The right-hand side of the above equation can be expressed as a product of the imaginary time Green's function of the non-interacting system which has an exact form for a given energy dispersion. We should note that for the bosonic case, we end up with similar equation as Eq. 2.27 without the prefactor $(-1)^{\chi_{\mathcal{P}}}$.

Dealing with the above equation can be cumbersome in this current form, thus we need a more systematic way to treat this equation via Feynman diagrams which will be discussed further in the next section. Alternatively, determinant methods can be used to systematically evaluate those contractions as discussed in Sec. 2.3.

2.1.7 Feynman Diagrams

The non-interacting imaginary-time Green's function can be thought of as a propagator and is represented by an arrow leaving one point (in space and time) and entering another. One can visualize every term in Wick's theorem as a graph called a Feynman diagram. As with any graph, Feynman diagrams can be connected or disconnected, but only connected ones appear in the calculations while the disconnected diagrams cancel out in a perturbative expansion of Eq.2.26 [64]. Thus, Eq. 2.26 can be rewritten as

$$\mathcal{G}(\vec{k}\sigma, \tau) = - \sum_{n=0}^{\infty} \frac{(-1)^n}{n! \hbar^n} \langle \prod_{i=1}^n \int_0^{\beta \hbar} d\tau_i \hat{T} \left[\hat{c}_{\vec{k}\sigma}(\tau) \hat{c}_{\vec{k}\sigma}^\dagger(0) \prod_{i=1}^n \hat{V}(\tau_i) \right] \rangle_{0,c}, \quad (2.28)$$

where the subscript c stands for connected diagrams. For further details on the proof of this result, the reader is advised to refer to Ref. 64.

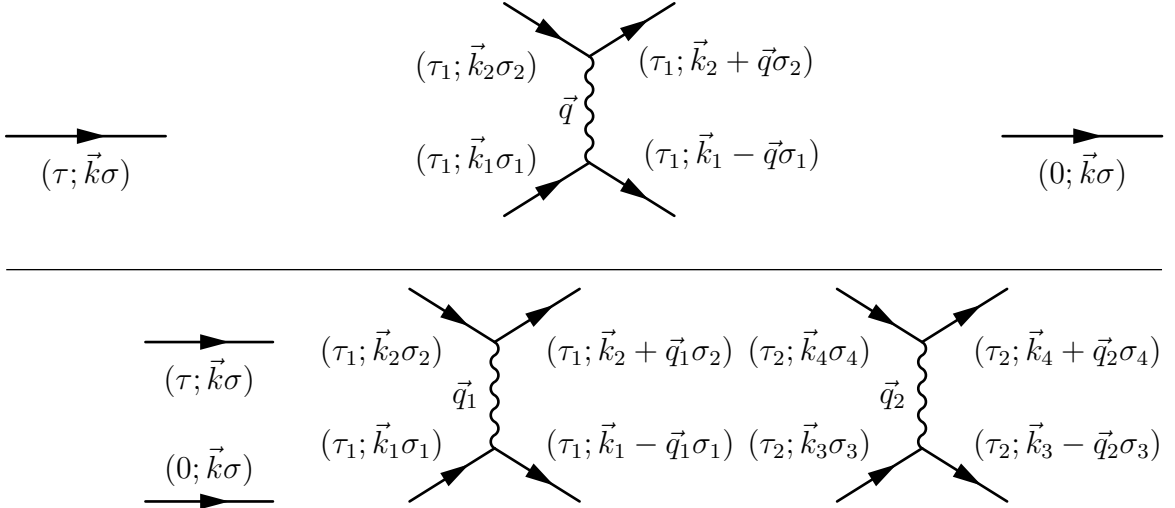


Figure 2.1: A draw map of the Feynman diagram setup for first order (top row) and second order (bottom row) perturbation theory.

Considering a two-body interaction of the form

$$\hat{V}(\tau) = \frac{1}{2} \sum_{\vec{q}} \sum_{\vec{k}_1, \vec{k}_2, \sigma_1, \sigma_2} V_q \hat{c}_{\vec{k}_1 + \vec{q}, \sigma_1}^\dagger(\tau) \hat{c}_{\vec{k}_2 - \vec{q}, \sigma_2}^\dagger(\tau) \hat{c}_{\vec{k}_2, \sigma_2}(\tau) \hat{c}_{\vec{k}_1, \sigma_1}(\tau), \quad (2.29)$$

let us assume that we want to calculate the imaginary-time Green's function (Eq. 2.26). In this case, all the possible Wick contractions can be understood graphically as follows: At first order, $n = 1$, these contractions correspond to all possible ways of connecting an arrow leaving one vertex (external or internal) to another arrow entering the same or different vertex as shown in Fig.2.1 (top row). This will result in four connected and two disconnected graphs, where the latter are to be excluded following Eq. 2.28. Similarly, for $n = 2$, the graphs that describe the Wick contractions can be generated from Fig. 2.1(bottom row) which will be 80 connected diagrams and 40 disconnected ones where the latter is to be excluded. The number of Feynman diagrams grows factorially with the perturbation order, in fact, at every perturbation

order n , there are total of $(2n + 1)!$ diagrams (connected and disconnected) for the case of the imaginary-time Green's function.

In standard diagrammatics, simplifications can be done as follows. First, one has to filter the disconnected diagrams when studying a given observable. The next is to identify the distinct topologies for the given graphs which reduces the computational costs. In fact, if there are M connected diagrams at a given perturbation order n for the case of general two-body interaction Hamiltonian, then the number of distinct topologies is $M/2^n n!$. Of course identifying those topologies might be computationally expensive to find, but it is a great reduction whenever possible.

For the purpose of our calculations, we would like to stick with the frequency-momentum space representation of Green's functions where we perform the Fourier transformation

$$\mathcal{G}(\vec{k}\sigma, \tau) = \frac{1}{\beta\hbar} \sum_{n=-\infty}^{n=+\infty} \mathcal{G}(\vec{k}\sigma, i\Omega_n) e^{-i\Omega_n\tau}, \quad (2.30)$$

where Ω_n is the Matsubara frequency. For fermions $\Omega_n = (2n + 1)/\beta\hbar$, and for bosons we have $\Omega_n = 2n/\beta\hbar$, where those frequencies are the complex poles of Fermi and Bose functions. This transformation also applies to the non-interacting imaginary-time Green's functions $\mathcal{G}^{(0)}(\vec{k}\sigma, \tau)$ which occur due to the Wick's theorem in the perturbative expansion Eq.2.28. Consequently, the time integrals in Eq. 2.28 will disappear and the only thing left is to use the correct frequency label for every fermion line so that the conservation laws at every vertex hold. This procedure is done systematically using our labeling scheme discussed in Section 2.3.4. Moreover, an important step in this representation is to evaluate the discrete summations over the internal Matsubara frequencies with the help of the residue theorem using the algorithmic Matsubara integration [88].

Lastly, we would like to state the Feynman rules for the diagrams in the momentum-frequency space for two-body interactions (Eq. 2.29) [64]:

1. Draw all of the $2n + 1$ Fermion lines for a given n^{th} order contraction.
2. The two external lines with coordinates $(\vec{k}\sigma, \omega_{\text{ex}})$ are denoted by $\mathcal{G}^{(0)}(\vec{k}\sigma, i\omega_{\text{ex}})$, while any of the internal Fermion line with coordinates $(\vec{p}\sigma, i\Omega_n)$ is denoted by $\mathcal{G}^{(0)}(\vec{p}\sigma, \Omega_n)$.
3. We apply conservation laws at each internal vertex to obtain the correct frequency label of each propagator.
4. Multiply all of the Green's functions together with the corresponding V_q 's, then summing over all internal variables (spin, momenta, frequency, etc.).
5. Multiply the above result by $(-1/\beta\hbar^2)^n (-1)^F$, where n is the perturbation order and F is the number of closed Fermion loop. The prefactor $(-1)^F$ serves as the sign of the Wick contraction represented by a Feynman graph.

2.2 Algorithmic Matsubara Integration

The starting point of the AMI procedure is the evaluation of a general term that takes the following form

$$\mathcal{J}_n = \frac{1}{\beta^n} \sum_{\Omega_1} \sum_{\Omega_2} \cdots \sum_{\Omega_n} \prod_{\ell=1}^{\ell=2n-1} \mathcal{G}_\ell^{(0)}(\vec{\alpha}_\ell, \varepsilon_\ell), \quad (2.31)$$

where n is the perturbation order, β is the inverse temperature and $\mathcal{G}_\ell^{(0)}(\vec{\alpha}_\ell, \varepsilon_\ell)$ is the non-interacting Green's function,

$$\mathcal{G}_\ell^{(0)}(\vec{\alpha}_\ell, \varepsilon_\ell) = \frac{1}{i\vec{\alpha}_\ell \cdot \vec{\Omega} - \varepsilon_\ell}, \quad (2.32)$$

where $\vec{\alpha}_\ell = (\alpha_1^\ell, \alpha_2^\ell, \dots, \alpha_n^\ell, \alpha_{n+1}^\ell)^t$ with $\alpha_j^\ell = \{0, \pm 1\}$, $\vec{\Omega} = (\Omega_1, \Omega_2, \dots, \Omega_n, \omega_{\text{ex}})^t$ with Ω_j and ω_{ex} being the internal and the external Matsubara frequencies, respectively, and ε_ℓ being the dispersion. For example, in first order perturbation theory one could have

$$\mathcal{J}_1 = \frac{1}{\beta} \sum_{\Omega_n} \frac{1}{i\Omega_n - \varepsilon} \quad (2.33)$$

where ε could depend on the external frequency. In order to evaluate \mathcal{J}_1 , we use the contour integration method and the residue theorem where we end up with [64]

$$\mathcal{J}_1 = f(\varepsilon) \text{Res}\left\{\frac{1}{z - \varepsilon}\right\}_{z=\varepsilon} = f(\varepsilon) \quad (2.34)$$

where $\text{Res}\{h(z)\}_{z=z_0}$ is the residue of $h(z)$ at $z = z_0$ and $f(\varepsilon) = (e^{\beta\varepsilon} + 1)^{-1}$ is the Fermi-Dirac distribution function. Generally speaking, the nested summations in \mathcal{J}_n could have more than one pole each of which can have multiplicity greater than 1. Hence, a single Matsubara summation in \mathcal{J}_n is evaluated via the following standard equation

$$\frac{1}{\beta} \sum_{i\Omega_s} h(i\Omega_s) = \sum_{z_p} f(z_p) \text{Res}\{h(z)\}_{z=z_p} \quad (2.35)$$

for the set of poles $\{z_p\}$ and the residue has the following general formula

$$\text{Res}\{h(z)\}_{z=z_p} = \frac{1}{(M-1)!} \lim_{z \rightarrow z_p} \frac{d^{(M-1)}}{dz^{M-1}} \{(z - z_p)^M h(z)\} \quad (2.36)$$

where $M = 1, 2, \dots$ is the multiplicity of the pole z_p .

The AMI algorithm uses the above equations to evaluate the general summation in Eq. 2.31 where at each step it identifies the poles of the integrand and then uses the residue theorem to find the result at every step. This process will contain lots of nested terms due to the use of the residue theorem at every step, thus a careful analysis is needed to do these calculations symbolically. As a starting point, the

non-interacting Green's function is expressed in the following array form

$$\mathcal{G}_\ell^{(0)}(\vec{\alpha}_\ell, \varepsilon_\ell) := [\varepsilon_\ell, \vec{\alpha}_\ell]. \quad (2.37)$$

Consequently, we have

$$\prod_{\ell=1}^{\ell=N} \mathcal{G}_\ell^{(0)}(\vec{\alpha}_\ell, \varepsilon_\ell) := [[\varepsilon_1, \vec{\alpha}_1]; [\varepsilon_2, \vec{\alpha}_2]; \dots; [\varepsilon_N, \vec{\alpha}_N]], \quad (2.38)$$

which is an array of size $N \times (n + 1)$. Suppose that we start by evaluating the summation over the j^{th} internal frequency,

$$\mathcal{J}^{(j)} = \frac{1}{\beta} \sum_{\Omega_j} \prod_{\ell=1}^{\ell=N} \mathcal{G}_\ell^{(0)}(\vec{\alpha}_\ell, \varepsilon_\ell). \quad (2.39)$$

If the product in the above summation has r_j simple poles, then due to the residue theorem we end up with a sum of r_j terms which can be expressed in an array of size $r_j \times (N - 1) \times (n + 1)$. At every later step, the size of this three-dimensional array is changing where r_j increases while N decreases until we finish the procedure with a final array of size $r_1 r_2 \dots r_n \times 1 \times (n + 1)$ which will be a function of the external frequency (ω_{ex}). Algorithmically, this recursive procedure is done first by introducing three arrays R , P , and S defined as follows [88]. First, the R_j array represents the configurations of the Green's functions obtained after summing over the j^{th} frequency, i.e. the three dimensional array discussed above. Second, P_j is the array of poles of the Green's functions obtained in the previous summation R_{j-1} ,

$$P_j := [P_j^{(1)}, P_j^{(2)}, \dots, P_j^{(r_{j-1})}], \quad (2.40)$$

where

$$P_j^{(q)} := \left[z_{jq}^{(i_1)}, z_{jq}^{(i_2)}, \dots, z_{jq}^{(i_{r_q})} \right]. \quad (2.41)$$

The third array, which has the size of P_j , is

$$S_j := \left[S_j^{(1)}, S_j^{(2)}, \dots, S_j^{(r_{j-1})} \right], \quad (2.42)$$

where

$$S_j^{(q)} := \left[\alpha_{jq}^{(i_1)}, \alpha_{jq}^{(i_2)}, \dots, \alpha_{jq}^{(i_{r_q})} \right]. \quad (2.43)$$

with $\alpha_{jq}^{(i_m)} = \{\pm 1, 0\}$. Consequently, the final result of the summation in Eq. 2.31 is [88]

$$\mathcal{J} = K \cdot R_n, \quad (2.44)$$

where

$$K = [S_1 \star f(P_1)] \times [S_2 \star f(P_2)] \times \dots \times [S_n \star f(P_n)], \quad (2.45)$$

with $f(P_j)$ being the Fermi function of an array,

$$[f(P_j)]_\ell^i = f(z_{j\ell}^{(i)}). \quad (2.46)$$

It is important to define the operations between the arrays that provides the final result in Eq. 2.44 [88]

$$(\mathcal{F} \star \mathcal{G})_i^j = \mathcal{F}_i^j \mathcal{G}_i^j \equiv \mathcal{O}_i^j, \quad (2.47)$$

$$(\mathcal{O} \times \mathcal{H})_i^j = \mathcal{O}_i \mathcal{H}_i^j, \quad (2.48)$$

$$\mathcal{H} \cdot \mathcal{Q} = \sum_i \mathcal{H}_i \mathcal{Q}_i. \quad (2.49)$$

where objects with two indices are 2 dimensional arrays and the location of the indices is just for our own convention. We should mention that some of the poles can have multiplicity greater than 1. In this case, one needs to account for that by performing automatic derivatives [88]. This will increase the sizes of the arrays P and R with the array S having entries $\pm \frac{1}{(M-1)!}$ instead of ± 1 and the final AMI result in Eq. 2.44 is still valid.

2.3 Symbolic Determinant Construction of Perturbative Expansions

2.3.1 Motivations: Why symDET?

Perturbation theories are a fundamental tool in a physicist’s arsenal for tackling interacting electron systems. In many body perturbation theory (MBPT), physical observables are expressed as an infinite series where each subsequent order is represented by an exponentially large number of contractions generated from Wick’s theorem. Each contraction requires the evaluation of integrals over the set of all internal variables. There are several ways to treat MBPT numerically, the most popular perhaps being Diagrammatic Monte Carlo (DiagMC) algorithms [75,78,150,151]. Standard DiagMC methods suffer from the fermionic sign problem that results from the large number of contractions (diagrams) with alternating sign. [75,150] In recent years, determinant methods have been introduced that can somewhat mitigate this issue. [79–81] The connected determinant diagrammatic Monte Carlo (CDet) method was introduced to treat perturbative expansions and avoids the factorial scaling of

diagrams at exponential cost [1, 82, 84].

Those methods, however, are based on the Matsubara formalism for finite temperatures and require numerical forms of analytic continuation in order to produce dynamical properties in real-frequency or real-time. More recently the advent of algorithmic Matsubara integration (AMI) [88, 152] method allowed us to symbolically evaluate summations over Matsubara frequencies and has been successfully applied to a number of physical problems such as the 2D Hubbard model [77, 90, 91, 153] as well as the uniform electron gas. [92, 93] AMI provides access to real frequency calculations via textbook analytic continuation, the replacement $i\omega_n \rightarrow \omega + i\Gamma$ with the regulator $\Gamma \rightarrow 0^+$, which avoids ill-posed numerical analytic continuation schemes [154]. It reduces the sampling space of internal variables minimizing the effect of the curse of dimensionality and reducing overall numerical uncertainty.

Taking into account the advantages of both determinantal methods as well as the AMI, we introduce a fully algorithmic approach which we call the symbolic determinant method (symDET) that can treat a very general class of Hamiltonians that are relevant to quantum chemistry and condensed matter physics. We start by generating Wick contractions symbolically via determinant and then proceed to Fourier transform those contractions also symbolically. We then perform the integrals over the internal variables with the use of AMI for evaluating the Matsubara summations. We discuss all of the elements of this algorithm in the next few sections. We then apply symDET to several applications for fermionic systems in Section 2.4 [94]. Finally, we provide a summary at the end of this chapter.

2.3.2 General Model

The current structure of our symDET algorithm assumes the following very general two-body interaction Hamiltonian

$$\mathcal{H} = \sum_a \varepsilon_a f_a^\dagger f_a + \frac{1}{2} \sum_{abcd} V_{abcd} f_a^\dagger f_c^\dagger f_d f_b, \quad (2.50)$$

where a, b, c, d are general indices that could represent orbital quantum numbers in molecular chemistry problems, or can be a combination of momentum and spin indices for lattice models, ε_a is the free particle dispersion, f_a^\dagger (f_a) is the creation (annihilation) operator of fermions and V_{abcd} is the general two-body interaction strength. We always assume the quadratic part of the Hamiltonian to be diagonal (of the form $f_a^\dagger f_a$) which is very important for the AMI part of the algorithm [88].

2.3.3 Wick Contractions via Determinant

The main goal of MBPT is to calculate the m th order correction to the imaginary time Green's function,

$$G_{ba}^{(m)}(\tau) = \frac{(-1)^m}{m!} \left\langle \hat{\mathcal{T}} \left[\prod_{\ell=1}^m \int_0^\beta d\tau_\ell H_V(\tau_\ell) \right] f_b(\tau) f_a^\dagger(0) \right\rangle_0 \quad (2.51)$$

, where $H_V(\tau_\ell)$ is the quartic part of the general Hamiltonian (Eq. 2.50) in the interaction picture. We see that at order m we must compute the expectation value of a sequence of $4m$ creation and annihilation operators attached to times τ_m , in addition to the external operators $f_b(\tau)$ and $f_a^\dagger(0)$.

This expectation value can be evaluated using Wick's theorem, replacing the expectation value with a sum of all possible contractions of creation and annihilation operators. This is typically accomplished in matrix form with rows and columns

represented by annihilation and creation operators, respectively. One can then generate all possible contractions - while also keeping correct track of the fermionic sign arising from commuting fermionic operators - by just taking the determinant of said matrix [82, 84].

For this we define \mathbf{G} to be a $(2m + 1) \times (2m + 1)$ matrix in which the rows (columns) correspond to the $2m$ annihilation (creation) operators plus an additional entry in each for the external vertices. We introduce column and row indices ℓ, s such that

$$\begin{aligned} \{a_\ell\} &:= \{a_1, c_1, a_2, c_2, \dots, a_m, c_m, a_{out}\}, \\ \{b_s\} &:= \{b_1, d_1, b_2, d_2, \dots, b_m, d_m, b_{in}\}, \end{aligned} \tag{2.52}$$

and define the matrix elements [1]

$$\mathbf{G}_{s\ell} := -\langle f_{b_s}(\tau_s) f_{a_\ell}^\dagger(\tau_\ell) \rangle_0 = g_{b_s a_\ell}(\tau_s - \tau_\ell + 0^-) = g_{\ell s}. \tag{2.53}$$

The full matrix can then be written

$$\mathbf{G} := \begin{bmatrix} g_{11} & g_{12} & \cdots & g_{1M} \\ g_{21} & g_{22} & \cdots & g_{2M} \\ \vdots & \vdots & \ddots & \vdots \\ g_{M1} & g_{M2} & \cdots & g_{MM} \end{bmatrix}, \tag{2.54}$$

where $M = 2m + 1$.

This construction has been presented numerous times and forms the basis for determinant Monte Carlo methods applied to many-body systems [1, 82, 82, 84, 155]. In the standard prescription, the \mathbf{G} matrix is populated in real space and imaginary-time. The determinant procedure is typically evaluated numerically by inserting numerical

values for the imaginary time Green's function, and sampling over all continuous times τ_m . There is one caveat to doing this is that the terms generated represent both connected and disconnected Feynman graphs. Removing the disconnected components can be accomplished with the recent method described by Rossi et al. [82].

When creating a symbolic representation of the matrix form of Eq. (2.54) each element with row and column indices ℓ and s is just a function of those indices. We can therefore generate a symbolic representation by replacing the entries with their row and column indices, $\mathbf{G}_{\ell s} \rightarrow (\ell, s)$.

If we can take a determinant of this matrix and store each term separately, we will have generated the expressions that represent the $n!$ connected and disconnected diagrams. Evaluation of numerical determinants can be accomplished in $O(n^3)$ time, an advantage of modern determinantal methods [82, 156, 157], but since we want to proceed symbolically there is no obvious route to such fast evaluations. Instead, we take the most pedantic approach and simply store the explicit parameters of each term in the determinant. While this factorial scaling sounds problematic, the tradeoff is an analytic expression that is exact to machine precision. This is in lieu of stochastic methods that, while they can evaluate determinants quickly, must perform temporal integrals via Monte-Carlo sampling, a process that for high accuracy requires typically 10^6 to 10^8 samples. We expect that for low orders we will arrive at a precise numerical result with fewer operations despite this factorial scaling. Furthermore, using our symDET algorithm one can recover the real-frequency observables analytically via the replacement $i\omega_{\text{ex}} \rightarrow \omega_{\text{ex}} + i0^+$.

To proceed we use the Leibniz formula for an $n \times n$ matrix, A with elements $a_{i,j}$:

$$\det(A) = \sum_{p \in \mathcal{P}_n} \left((-1)^p \prod_{i=1}^n a_{i,p_i} \right). \quad (2.55)$$

In this expression, $p = (p_1, p_2, \dots, p_n)$ is a permutation of the set $\{1, 2, \dots, n\}$ and \mathcal{P}_n

is the set of all such permutations. Finding the permutations of p and the associated signs is a straightforward computational problem. To do this symbolically we generate a permutation p and then store the indices of a_{i,p_i} , i.e. (i, p_i) for each i . Each term in Eq. 2.55 is then completely defined by a vector of such pairs, and a single $+1/-1$ sign prefactor.

This represents a major departure from typical determinantal QMC methods [83, 158] where such a matrix is filled with numerical values. In our case we have yet to assign values to the entries and instead we want to store the information required to later symbolically construct the expression.

2.3.4 Symbolic Fourier Transform

A very interesting and useful property of Feynman diagrams is that the set of possible diagram topologies is independent of coordinate and temporal labelling of each vertex. However, in the contractions of Eq. 2.54 each topology may appear multiple times - as is famously the case for a single-band problem where the $m!$ denominator is precisely cancelled by $m!$ duplicates of each topology. Since we have each contraction - we are free to represent each as a graph in momentum and Matsubara frequency space. However, in doing so one would need to develop an internally consistent labelling of each graph - a process that is fundamentally non-local in diagram topology and also is not unique.

Instead we choose to mimic the analytic process and have devised an analytic representation of the temporal Fourier transform. The procedure, detailed in Appendix A, sorts the contraction pairs (i, j) that represent imaginary time Green's functions spanning between internal times $\tau_{\lfloor \frac{i}{2} \rfloor}$ and $\tau_{\lfloor \frac{j}{2} \rfloor}$. The pairs are then separated into three lists A , B , and C . Graphically, A contains all edges $(n - 1)$ of a directed tree that connects the internal n vertices, B contains the external edges that

connects internal vertices to the external vertex, and C has the remaining edges of the full directed graph. Since the contraction pairs are effectively source/target sets, the connectivity of the contraction can be determined directly as is done in graph theory, identical to a depth first search, at minimal expense, scaling with the number of vertices, n , which is typically small and scales as 2^n for perturbation order n . If at the end of the process the number of pairs in A is $n - 1$, in B is 2 and in C we have n pairs, then the diagram is connected. Now, the symbolic Fourier transform (SFT) of the time integrals is done by simply converting those three lists to matrices as described in Appendix A. The advantage of this is that one obtains a unique set of internal labels that obey energy and momentum conservation at all vertices. The main result is given in Eq. A.13 which is a matrix with entries zero, and ± 1 . We should stress that our SFT procedure does two jobs at once. First, if the sizes of the A , B , and C lists match the above listed sizes then the contraction is equivalent to a connected Feynman diagram and it automatically gives the conserving frequency labels, else it omits the contraction as it is equivalent to a disconnected Feynman diagram.

2.3.5 Minimal Sampling of Internal Variables

Once the proper frequency labels are assigned, our n^{th} order perturbative expansion is of the form

$$G_{ba}^{(n)}(\omega_{\text{ex}}) = \frac{(-1)^n}{n!} g_b(i\omega_{\text{ex}}) g_a(i\omega_{\text{ex}}) \times \sum_{e_1, \dots, e_{2n-1}} \sum_{\{\Omega_n\}} \sum_{c \in \mathcal{C}} \text{sgn}(c) \prod_j^{2n-1} g_{e_j}^j(\boldsymbol{\alpha}_j \cdot \boldsymbol{\omega}) \quad (2.56)$$

where the first summation is over the internal variables e_i (e.g. orbital numbers, momenta, spin, or a mix of them), where the space of such variables reduces from N^{4n} to N^{2n-1} with N being the size of such basis, the second summation is over the

set of internal Matsubara frequencies, and the last is over all contractions belonging to the set \mathcal{C} obtained from the determinant of the matrix Eq. 2.54 with contractions equivalent to disconnected diagrams omitted via the SFT procedure, and $\text{sgn}(c)$ being the sign of the corresponding contraction. Here α_j is the j^{th} row in Eq. A.13, $\omega = (\Omega_1, \dots, \Omega_n, \omega_{\text{ex}})^T$ and

$$g_{e_j}^j(\alpha_j \cdot \omega) = \frac{1}{i\alpha_j \cdot \omega - \varepsilon_{e_j}} \quad (2.57)$$

is the Fourier transformed free propagator. The usual process of evaluating the above nested summation is done with the use of the Monte Carlo sampling of the internal variables $\{e_i, \Omega_i\}$ [78, 159, 160]. To reduce this larger space of samples, one only samples over $\{e_i\}$ while the summations over the Matsubara frequencies $\{\Omega_i\}$ at every sample of $\{e_i\}$ is performed analytically via the algorithmic Matsubara integration (AMI) [88, 152]. In the case of molecular problems, or generically *discrete* systems, one performs the e_i summations directly such that our algorithm gives the exact value of the perturbative expansion. However, in the case of lattice problems, we use stochastic sampling over momenta and we obtain results with stochastic error bars. In both cases, the Matsubara summations are evaluated exactly using the AMI. We summarize the symDET procedure in Fig. 2.2.

2.4 Applications to Fermionic Systems

2.4.1 Molecular Chemistry Problems: H_2

Molecular hydrogen is the simplest system to consider as a test-bed for method development and here we start with the simplest representation in the Slater-type orbitals basis STO-6g which describes the interaction between the two hydrogen atoms having

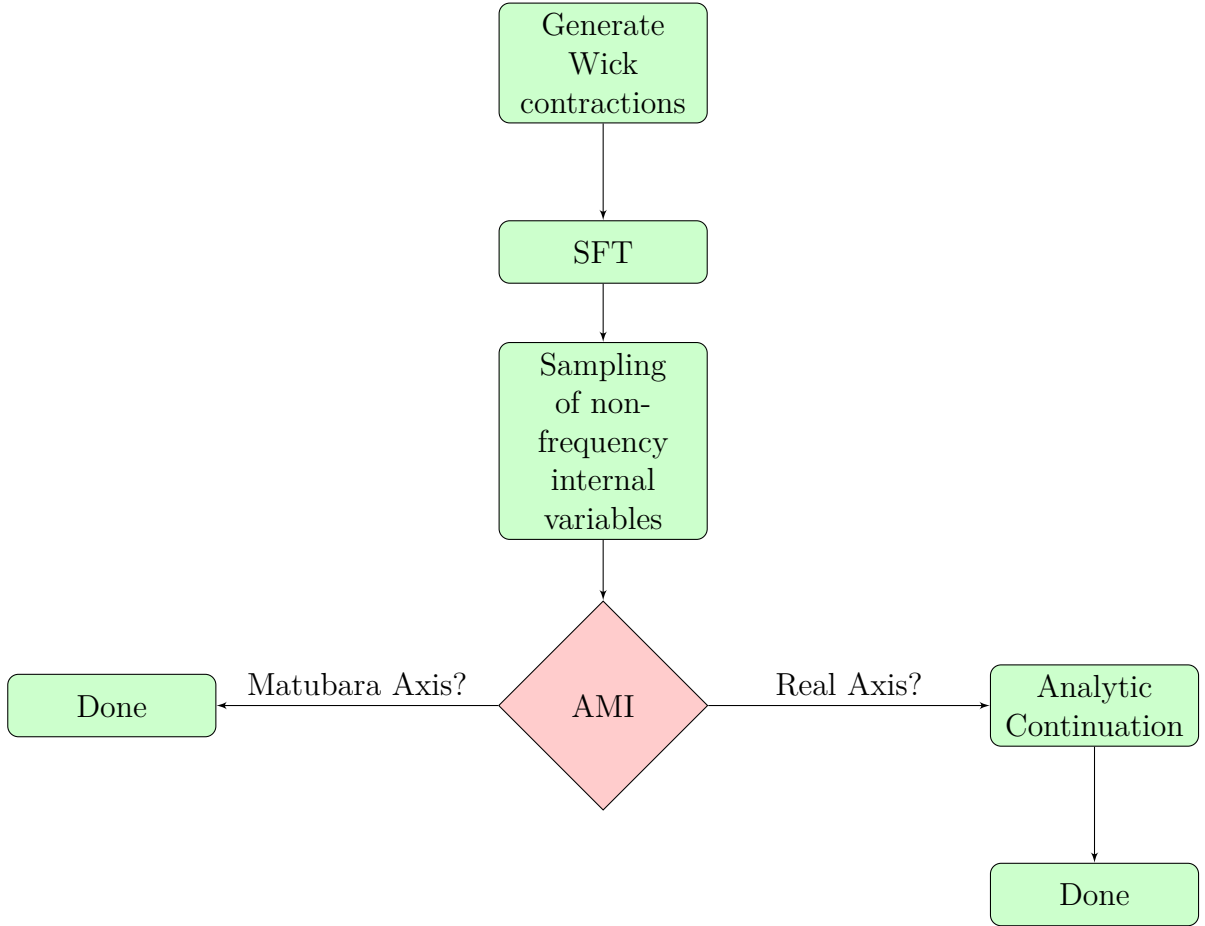


Figure 2.2: Flow chart of the symDET steps. First, contractions are generated from the determinant of Eq. 2.54, then the SFT is used to filter contractions and provide the correct conserving labels to contractions that are equivalent to connected diagrams. Thirdly, we sample over all internal non-frequency variables and perform the nested Matsubara summations via the AMI. At this stage, analytic expressions are stored and if real frequency calculations are needed, the analytic continuation is performed exactly from those expressions.

only 1s orbitals. In particular, we will see later in Section 2.4.3 that the two state problem is the basic component of a single-band with spin \uparrow/\downarrow and therefore correct results for the STO-6g basis are paramount in developing the method beyond simple problems. We use the Python-based Simulations of Chemistry Framework (PySCF) package [161] to obtain the Hartree-Fock solutions for the STO-6g basis from which we compute the self energy on the Matsubara axis illustrated in Fig. 2.3. We compare our results in detail to those in Ref. [1] and find that our exact result is within stochastic error bars of that work. Different from their result, our starting eigenstates are asymmetric, resulting in distinct values of Σ_{00} and Σ_{11} , while the off-diagonal self energy terms are zero in this case. While we stop at fourth order, there is no conceptual hurdle to evaluating higher orders or larger basis sets. However, the computational expense is factorial in order and exponential in basis. Nevertheless, the procedure is easily parallelizable.

The real advantage to our approach is the direct evaluation of real frequency properties. By symbolically replacing $i\omega_n \rightarrow \omega + i\Gamma$ we can plot the self energy in real frequencies shown in Fig. 2.4 for a particular choice of Γ that can be made arbitrarily small. Here we focus on a relevant frequency range where there is an expected new peak that is created by a sharp feature in $\text{Re}\Sigma(\omega)$ such that the interacting Green's function gains one or more additional poles. This is seen in the spectral function $A(\omega) = \text{Im}\{G(\omega)\}$ as shown in Fig. 2.5. The dominant peaks remain those of the non-interacting dispersion while additional peaks - shown in the insets - appear at energies offset by the peak difference $\Delta E = h_{11} - h_{00}$ which is expected based on the second order expansion. At fourth order shown, there are two additional poles instead of a single peak near $\omega = \pm 2$ as we can see in Fig.2.5 which accounts for interactions.

As an example for a larger basis set, we compute the self-energy for H_2 in the 10 orbital cc-pVDZ basis representation as shown Fig.2.6. This basis is five times

larger than its STO-6g counterpart, stressing our ability to study larger molecules with symDET.

An interesting implication of these calculations is the ability to perform self-consistent perturbation theory beyond the well-known second order Green's Function method (GF₂)₀ [158]. In GF₂, one uses the truncated Green's function at second order as the starting free propagator for the next iteration and this process is repeated until convergence occurred. For molecular chemistry problems, this implementation of GF_n (where $n \geq 2$) is exact at each order and is valid at finite or zero temperatures, and at any physical parameters. For example, the binding energy for molecules is obtained by generating the poles of the full propagator which is easy via the AMI part of our code.

2.4.2 The Dimer Model

To demonstrate the versatility of our approach we study the Hubbard dimer. The model consists of two sites each of which has a spin 1/2 particle. The model we use is [87]

$$H = H_0 + H_U + H_H + H_{SB} - \mu \sum_{i,\sigma} c_{i\sigma}^\dagger c_{i\sigma} \quad (2.58)$$

where $H_0 = -t \sum_{\sigma=\uparrow,\downarrow} (c_{0\sigma}^\dagger c_{1\sigma} + c_{0\sigma} c_{1\sigma}^\dagger)$ is the hopping term for electrons between the two sites, $H_U = U \sum_i n_{i\uparrow} n_{i\downarrow} - \frac{U}{2} \sum_{i\sigma} n_{i\sigma}$ describes the onsite interaction, $H_H = H \sum_i (n_{i\uparrow} - n_{i\downarrow})$ is the interaction due to an applied magnetic field, and $H_{SB} = U_a (n_{0\uparrow} n_{0\downarrow} - n_{1\uparrow} n_{1\downarrow}) + \mu_a (n_{0\uparrow} + n_{0\downarrow} - n_{1\uparrow} - n_{1\downarrow}) + H_a (n_{0\uparrow} - n_{0\downarrow} - n_{1\uparrow} + n_{1\downarrow})$ is a symmetry-breaking term. The quadratic part of the above Hamiltonian is not diagonal, hence we perform the proper diagonalization to bring it to the form in Eq. 2.50 with an effective four-bands system (two spin orientations and two sites). In this example, the self-energy in this basis is not diagonal but rather block-diagonal. As an

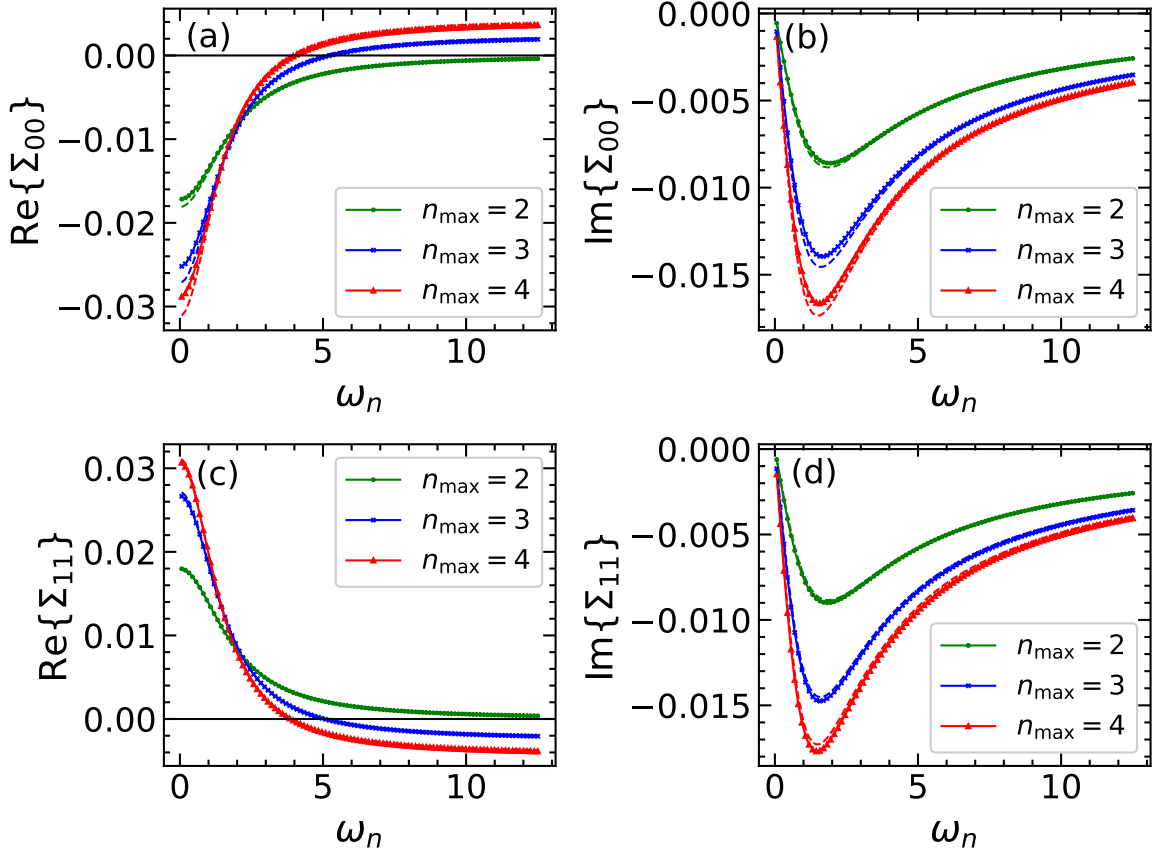


Figure 2.3: (a) and (b) The real and imaginary parts of the self-energy for H_2 in the STO-6g basis with external band indices $a_{\text{ex}} = b_{\text{ex}} = 0$. (c) and (d) plots of the real and imaginary parts of Σ^{H_2} for $a_{\text{ex}} = b_{\text{ex}} = 1$. Here $\beta = 50.0$. The dashed curves are the corresponding data obtained in Ref. 1

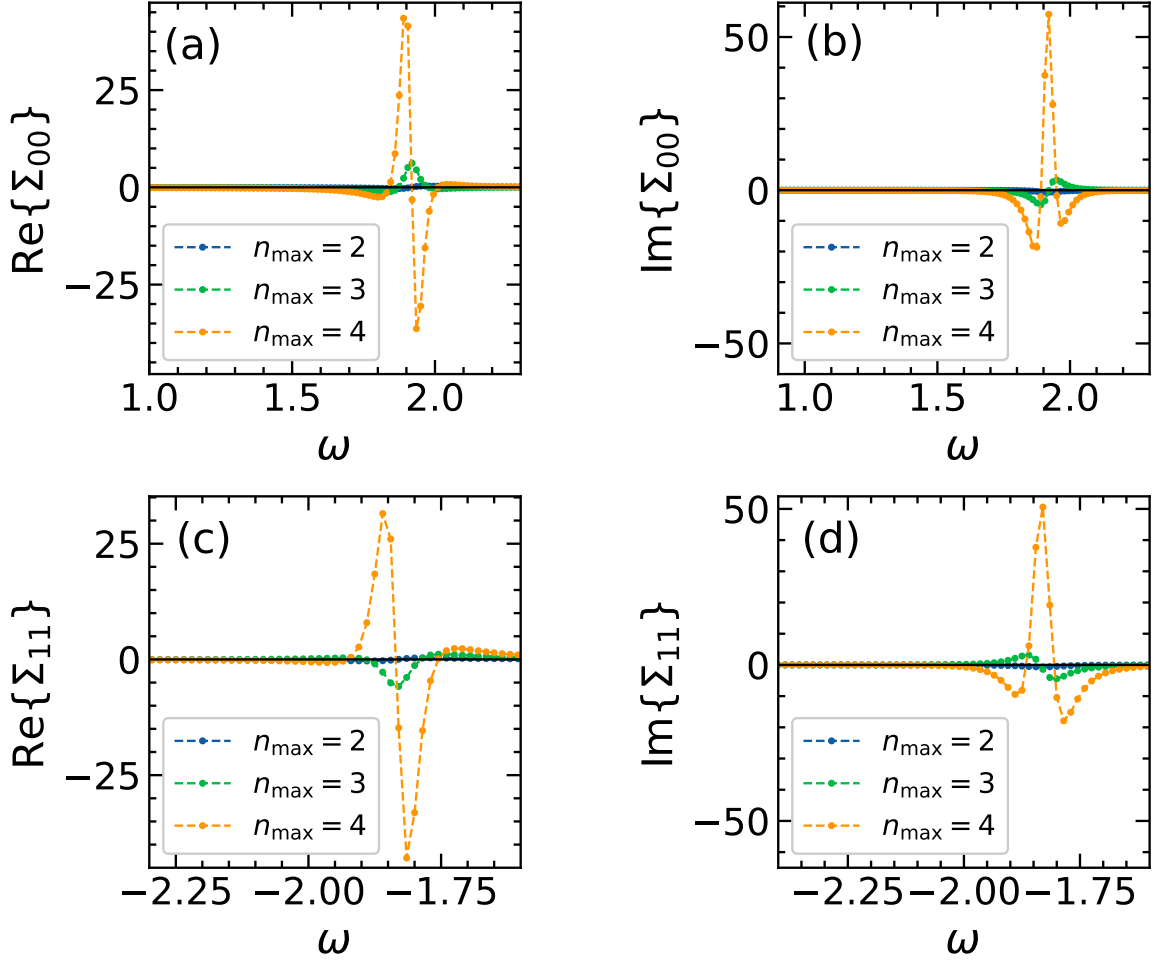


Figure 2.4: (a) and (b) the real and imaginary parts of Σ_{00} , while (c) & (d) are the components of the self-energy for the second band for H_2 (in the STO-6g basis) on the real frequency axes. Here the regulator is $\Gamma = 0.05$

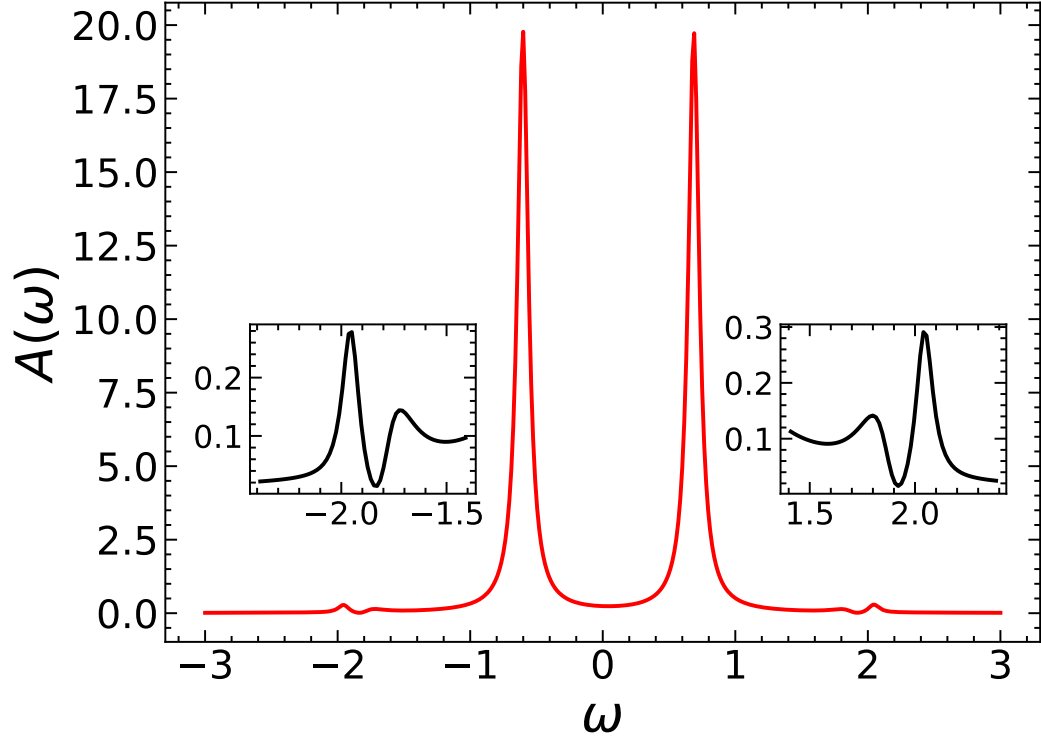


Figure 2.5: The spectral function for H_2 in the STO-6g basis is truncated at 4th order. The inset data is a zoom in of the extra peaks with lower intensity. Here the regulator 0.05.

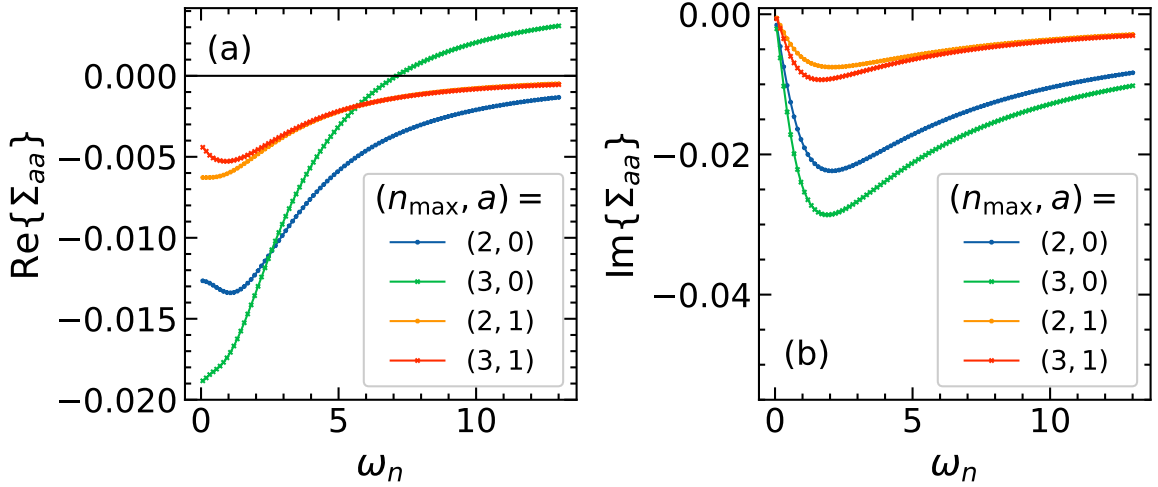


Figure 2.6: The self-energy for H_2 in the cc-pVDZ basis versus the Matsubara frequency with $\beta = 50.0$. (a) The real part of the self-energy components (0,0) and (1,1) truncated at second ($n_{\max} = 2$) and third ($n_{\max} = 3$) orders, and (b) are the imaginary counterparts.

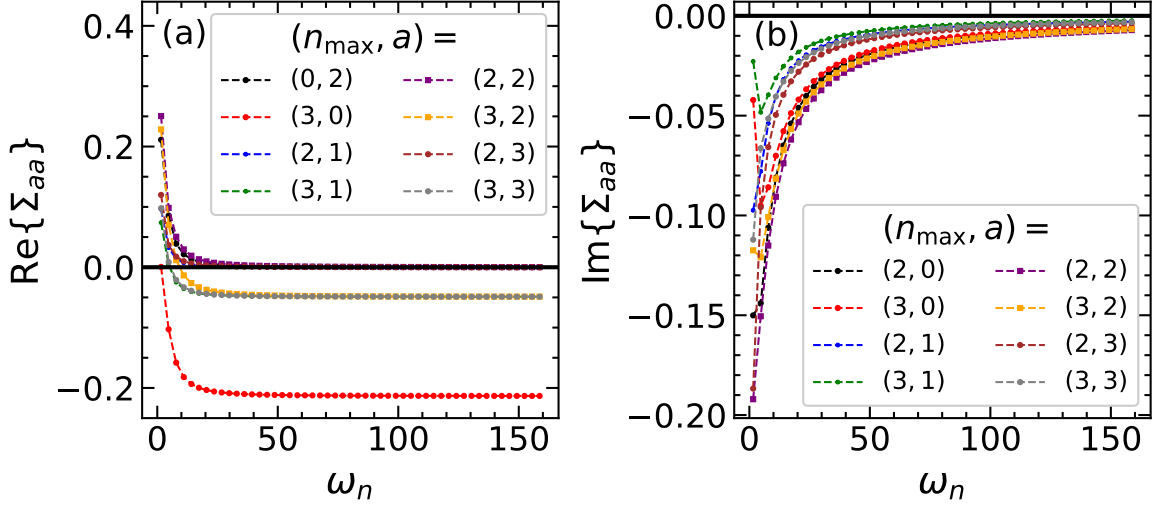


Figure 2.7: (a) and (b) the real and imaginary parts of the diagonal elements of the self-energy matrix for $n_{\max} = 2, 3$ for the Hubbard Dimer model (Eq.2.58). Here we took $t = 1.0$, $U = 2.5$, $\mu = 0.70$, $H = 0.30$, $U_a = 0.50$, $\mu_a = 0.20$, $H_a = 0.030$, and $\beta = 2.0$.

illustration, we plot the imaginary and real parts of Σ_{00} and Σ_{01} up to fourth order for $U = 2.5t = 5.0$, $\mu = 0.7$, $H = 0.30$, $U_a = 0.5$, $\mu_a = 0.20$, $H_a = 0.030$ and $\beta = 2.0$ in Fig.2.7.

2.4.3 Single-Band Hubbard Model on Square Lattice

The simplest starting point for considering a lattice Hamiltonian is the single-band Hubbard model of spin-1/2 Fermions on a square lattice. The model is typically written in real-space notation as

$$H = \sum_{\langle ij \rangle} \sum_{\sigma} t_{ij} c_{i\sigma}^{\dagger} c_{j\sigma} + U \sum_i n_{i\uparrow} n_{i\downarrow}, \quad (2.59)$$

where t_{ij} is the hopping amplitude, $c_{i\sigma}^{(\dagger)}$ is the annihilation (creation) operator at site i , $\sigma \in \{\uparrow, \downarrow\}$ is the spin, U is the onsite Hubbard interaction, $n_{i\sigma} = c_{i\sigma}^{\dagger} c_{i\sigma}$ is the number operator, μ is the chemical potential, and $\langle ij \rangle$ restricts the sum to nearest neighbors.

For a 2D square lattice we take $t_{ij} = -t$, resulting in the free particle energy

$$\epsilon(\mathbf{k}) = -2t[\cos(k_x) + \cos(k_y)] - \mu. \quad (2.60)$$

Mapping this problem to Eq. 2.50 leads to an effective model of two degenerate bands with states $\uparrow := (k, \sigma = \uparrow)$ and $\downarrow := (k, \sigma = \downarrow)$ and the band indices are then summed over up and down basis. This leads to a diagonal and spin independent $h_{ab} = \epsilon_k \delta_{ab}$ and an interaction term independent of momentum with entries $U_{\uparrow\uparrow\downarrow\downarrow} = U_{\downarrow\downarrow\uparrow\uparrow} = U$ and all other elements of U are zero.

Due to the additional k -indices, after processing with AMI each m^{th} order Wick contraction contains an m -dimensional integral over internal momentum vectors which requires approximate numerical integration methods to evaluate. Otherwise the procedure is unchanged from the two-band case of H_2 in the STO-6g basis which highlights the importance of that problem as a benchmark. As an illustration, we have calculated the self-energy for the 2D square lattice on the Matsubara axis shown in Fig. 2.8 for doped cases ($\mu \neq 0$). Moreover, the exact same expressions can be used to generate the matching real-frequency results which we show in Fig 2.9.

2.5 Summary

In this chapter we have presented an algorithm which we developed that can evaluate the coefficients of the many-body perturbation series for single and multiband problems with a general two-body interaction models at equilibrium. The steps to our determinant method are: (1) Generate contractions by evaluating the determinant of Eq.2.54, (2) perform the symbolic Fourier transform, (3) perform AMI to evaluate the Matsubara summations exactly, (4) sum or sample any remaining internal degrees of freedom. If we are interested in real-frequency calculations, analytic continuation is

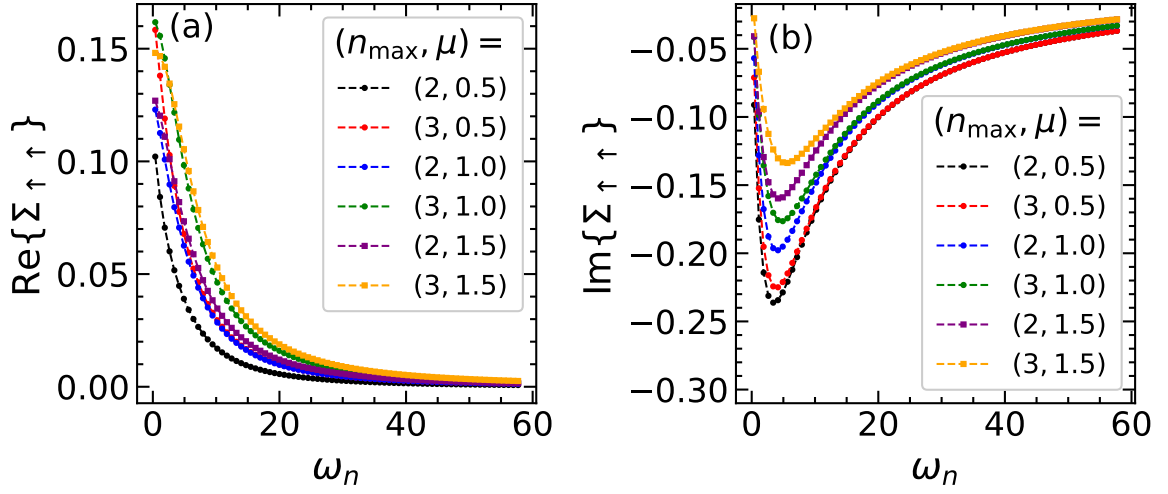


Figure 2.8: (a) The real part of the (spin up) self-energy of the two dimensional Hubbard model for $t = 1.0$, $U = 3.0$, $\beta = 8.33$, $\vec{k} = (0, \pi)$, and at different values of μ as indicated, and (b) are the imaginary counterparts.

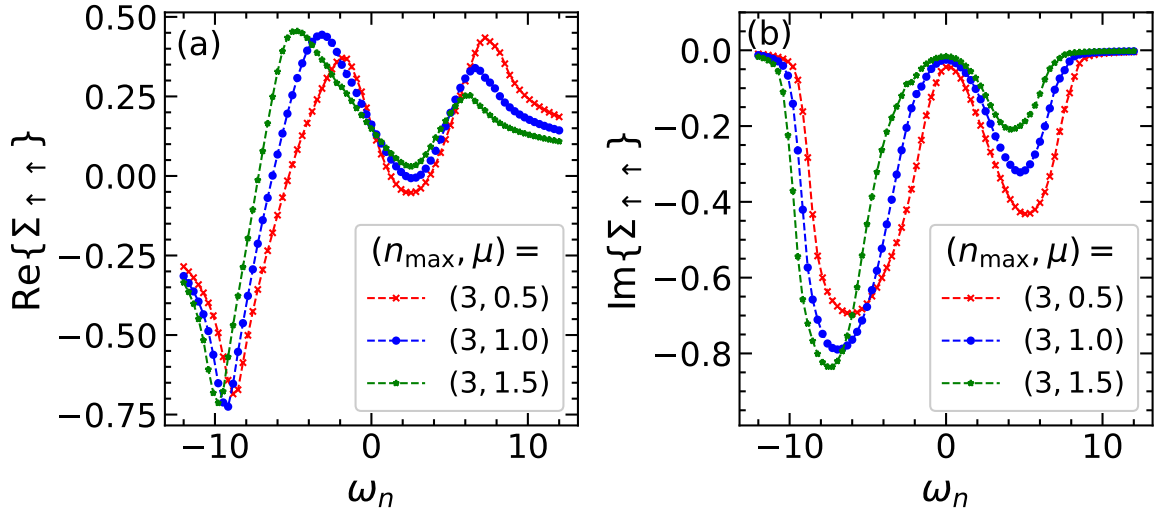


Figure 2.9: (a) and (b) the real and imaginary parts of the self-energy (truncated at third order) versus the real frequency for the 2D Hubbard model evaluated for the parameters choice: $U = 3t = 3.0$, $\beta = 8.33$, and $\vec{k} = (0, \pi)$ with different values of μ as indicated. We took a Monte-Carlo sample of size 1×10^8 and the regulator $\Gamma = 0.2$.

automatically applied in the analytic expressions.

We have applied our algorithm to a variety of problems from molecular chemistry to lattice models up to fourth order perturbation theory. The method is therefore flexible and can solve different models in both real and imaginary frequency domains allowing it to be of great importance for both quantum chemistry and lattice system applications. The bottleneck in computation of lattice systems remains the numerical integration over remaining spatial degrees of freedom. When the numerical regulator Γ is small this becomes difficult due to the sharp nature of the integrands. The use of renormalized perturbation theory might help alleviate these difficulties. [91] Finally, our algorithm, equivalent to a single shot GF_n exceeds what is currently available within the second-order Green's function method (GF_2) [158]. Although we limited ourselves to fourth order calculations, higher order corrections can be achieved, since the algorithm is valid at any arbitrary perturbation order and system size. Of particular interest is molecular problems where we are able to evaluate each perturbative order exactly to machine precision. In these cases, regardless of the computational expense of higher orders, since the result is exact it needs only be computed once.

Chapter 3

Floquet Theory for Driven Layered Twisted Systems

3.1 Review

In the previous chapter, we have shown how one can solve the generic two-body interaction Hamiltonian using symDET. This Hamiltonian spans a class of Hubbard-like models that describes electron interactions in twisted graphene systems at equilibrium [162–164]. In this chapter, we will study these twisted systems in the non-equilibrium case using Floquet theory within the non-interacting limit. The possible connection between Floquet theory and symDET is discussed in the next chapter.

A Floquet system is a physical system that is described via a periodic Hamiltonian $H(t)$, i.e. $H(t + T) = H(t)$ for some period T . One example is a graphene layer interacting with circularly polarized light. The system evolves in time according to the Schrodinger equation $H(t) |\psi(t)\rangle = i\hbar\partial_t |\psi(t)\rangle$. To solve this equation, one generally follow two choices: (1) the time evolution operator approach and (2) the quasi-energy operator method. For the first method, we recall that the time-evolution

operator $\mathcal{U}(t)$ satisfies the following first order differential equation

$$i \frac{\partial \mathcal{U}(t)}{\partial t} = H(t) \mathcal{U}(t) \quad (3.1)$$

where the above equation has the following general solution (a.k.a. time ordered exponential),

$$\mathcal{U}(t) = \hat{\mathcal{T}} \exp \left(-i \int dt H(t) \right) = \lim_{\delta t \rightarrow 0} \prod_{j=1}^{j=t/\delta t} \exp(-i \delta t H(n \delta t)) \quad (3.2)$$

where $\hat{\mathcal{T}}$ is the time-ordering operator. In Floquet methods, we generally focus on the physics averaged over a time interval, typically over one or more full periods. Hence, one can conclude the following property of the time evolution operator

$$\mathcal{U}(nT) = [\mathcal{U}(T)]^n \quad (3.3)$$

which leads us to define the Floquet Hamiltonian H_F as

$$U(T) = e^{-i H_F T} \quad (3.4)$$

As we can tell, this is similar to the situation of the time-independent Schrodinger equation. Hence the Floquet Hamiltonian is an effective time-independent Hamiltonian that describes the non-equilibrium system. Such a coarse-grained Hamiltonian can be used to describe different phases of the original physical system (modeled by $H(t)$) without the need to rely on the methods of time-dependent quantum mechanics. However, it can be challenging to obtain such a Hamiltonian due to the fact that computing the time evolution operator at stroboscopic times (multiples of period T) is still hard and finding the logarithm of a matrix is a difficult task (Eq.3.4). However,

approximations can be used to simplify the computations which gives solutions that are valid in high, low, and medium frequency regimes [165].

On the other hand, in the quasi-energy approach one adopts a general Bloch wavefunction (in the time domain) of the form $\psi(t) = e^{-i\varepsilon t}u(t)$, for some periodic function $u(t)$ and ε is the quasi-energy. Hence, the Schrodinger equation reduces to the following eigenvalue equation

$$[H(t) - i\partial_t] u(t) = \varepsilon u(t), \quad (3.5)$$

where $\mathcal{Q}(t) = H(t) - i\partial_t$ is the quasi-energy operator. Expanding $u(t)$ in the Fourier basis as $u(t) = \sum_n e^{in\omega t}u_n$, the above eigenvalue equation reduces to

$$\sum_{\ell} [H^{(j-\ell)} + \delta_{\ell,j} \ell\omega] u_{\ell} = \varepsilon u_j, \quad (3.6)$$

where $H^{(M)} = T^{-1} \int_0^T dt e^{-iM\omega t} H$ and $T = 2\pi/\omega$ [165]. Consequently, the problem becomes equivalent to a time-independent system. However, the price is that the corresponding matrix is infinite and hence truncations are a must. Thus, obtained solutions are limited to a range of frequency regimes. In the limits of high frequency regime, Eq. 3.6 predicts multiple copies of the non-interacting system shifted by the same frequency and this was confirmed experimentally [166, 167].

So far we have seen the complexity of such non-equilibrium systems. Hence, approximations are necessary means to move forward. One example of approximations is the Van Vleck expansion where, to first order approximation, the effective Hamiltonian reads [122, 168]

$$H_{\text{vV}}^{(1)} = H^{(0)} + \sum_{m \neq 0} \frac{H^{(-m)} H^{(m)}}{m\omega}, \quad (3.7)$$

where $H^{(m)}$ is the Fourier transform of $H(t)$. Other approximations work for larger

frequency regimes such as the rotating frame approximation which was used to study twisted bilayer and trilayer graphene systems under the influence of circularly polarized and waveguide lights [2, 169]. For further details on different kinds of approximations, it is recommended to read Ref. 165 and references therein.

An interesting class of materials where one can apply the above methods is the twisted layered graphene systems. The relative twist between the layers results in the appearance of moiré patterns which can be observed experimentally via scanning tunneling microscopy tools [170]. Moiré materials are characterized by magic angles at which flat bands appear in the band structure, for the case of twisted bilayer graphene this angle was found to be $\theta \approx 1.05$ degrees [171]. These flat bands are signature of strong electron-electron interactions, hence the possibility of different interesting states of matter to emerge. The vast majority of interesting states of matter appear in systems where electrons interact strongly with each other. Examples of such many body phenomenon are: heavy fermions [172], spin liquids [173], and high temperature superconductivity [174]. Thus, great efforts have been invested in investigating twisted materials near magic angles especially after the discovery of superconductivity in twisted bilayer graphene (TBLG) [175]. Moving forward, moiré materials were found to host variety of strongly correlated phases such as correlated insulators and ferrimagnetism [175–192].

An alternative approach to modify the band structure in graphene systems is to apply different forms of light onto the system such as circularly polarized light [193–197]. In this context, one needs to solve the associated time-dependent wave equation via Floquet methods, perturbative methods and other techniques [122–124, 198–202]. In recent years, both Floquet and moiré methods were combined resulting in additional features such as modified band structures, light-induced flat bands, and other interesting topological properties were theoretically predicted [143–146, 169, 203–

205].

In the next sections, we will apply Floquet engineering methods to two interesting physical systems. Firstly, we study the twisted trilayer graphene system under the influence of circularly polarized light and waveguide light and compute the topological maps in the case of circularly polarized light [2]. Secondly, we investigate the twisted bilayer graphene system with the inclusion of Haldane interactions along with the same forms of light and compute the band structure for the equilibrium and non-equilibrium cases.

3.2 Floquet Engineering and Topological Maps in Twisted Trilayer Graphene (TTLG)

3.2.1 Why TTLG?

Motivated by the recent experimental realization of twisted trilayer graphene (TTLG) and the observed superconductivity that is associated with its flat bands at specific angles [206], we study trilayer graphene under the influence of different forms of light in the non-interacting limit. Specifically, we study four different types of stacking configurations with a single twisted layer. In all four cases, we study the impact of circularly polarized light and longitudinal light coming from a waveguide. We derive effective time-independent Floquet Hamiltonians and review light-induced changes to the band structure. For circularly polarized light, we find band flattening effects as well as band gap openings. We emphasize that there is a rich band topology, which we summarize in Chern number maps that are different for all four studied lattice configurations. The case of a so-called ABC stacking with top layer twist is especially rich and shows a different phase diagram depending on the handedness of

the circularly polarized light. Consequently, we propose an experiment where this difference in typologies could be captured via optical conductivity measurements. In contrast, for the case of longitudinal light that is coming from a waveguide, we find that the band structure is very closely related to the equilibrium one but the magic angles can be tuned in-situ by varying the intensity of the incident beam of light.

The next few sections are organized as follows. In Sec. 3.2.2 we describe twisted trilayer graphene in equilibrium, introduce the model, and review some of its properties. In Sec. 3.2.3, we focus on circularly polarized light where we first analyze the band structures for the different TTLGs. We then derive effective time-independent Hamiltonians that allow for less computationally costly treatment of light-driven TTLG. These effective Hamiltonians are then used to study the band topology and suggest an experimental setup to test some of our predictions. Finally, in section 3.2.4 we consider longitudinal light coming from a waveguide. Here, we focus exclusively on changes to band structure and the effective Hamiltonian. We find that this type of light makes it possible to tune the magic angles, where flat bands appear. The effective Hamiltonian allows us to gain insight into the mechanism behind this observation.

3.2.2 Equilibrium Model

The system we will study in this work is twisted trilayer graphene in its various stacking configurations subjected to different forms of light. Here, we briefly review some of its equilibrium properties.

Trilayer graphene is formed by three layers of graphene stacked on top of one another. If two sheets are stacked in such a way that all the carbon atoms of one layer are exactly on top of an atom in the layer below this is called AA stacking. The case where only half of the atoms in the top layer have an atom exactly below it is referred to as either AB or BA stacking (there are two possible orderings). For trilayer

graphene there can be various possible configurations such as AAA, ABA and ABC stacking. To obtain twisted trilayer graphene each of these stackings can then have either the top or middle layer rotated with respect to the other layers, which will lead to a moiré pattern that is associated with a smaller moiré Brillouin zone (MBZ), as we show in Fig. 3.1.

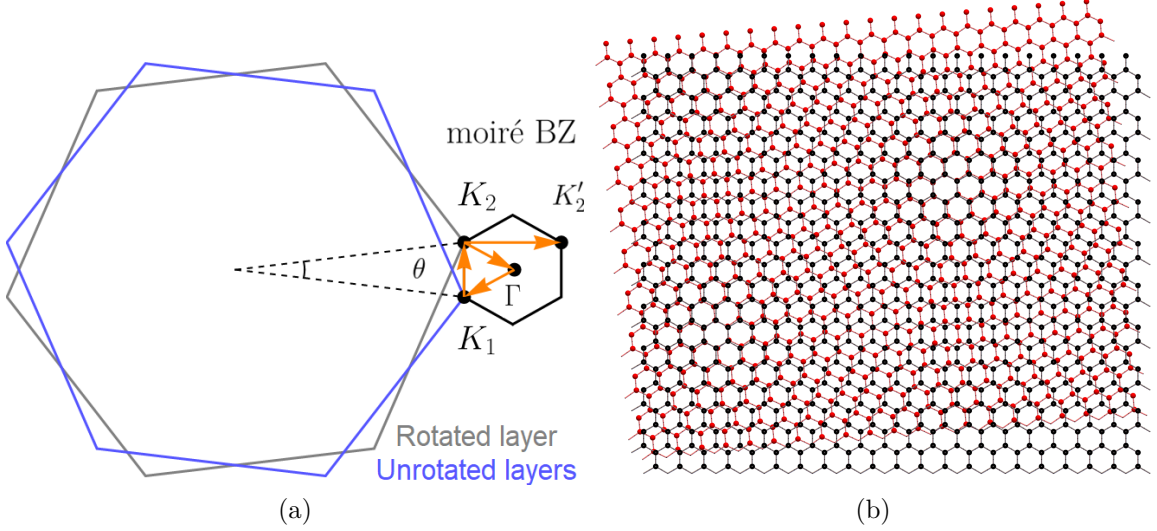


Figure 3.1: (a) The moiré Brillouin zone for a twisted trilayer graphene (TTLG) system with only one layer twisted. (b) Schematic plot of the TTLG system for the AAA stacking with middle layer twist showing the moiré pattern [2].

The static Hamiltonian for twisted trilayer graphene we will work with is based on the Hamiltonian introduced in earlier works [207, 208]. It is given as

$$H(\vec{x}, \vec{k}) = \begin{pmatrix} h_1(\theta_1, \vec{k} - \vec{\kappa}_1) & T_{12}(\vec{x}) & 0 \\ T_{12}^\dagger(\vec{x}) & h_1(\theta_2, \vec{k} - \vec{\kappa}_2) & T_{23}(\vec{x}) \\ 0 & T_{23}^\dagger(\vec{x}) & h_3(\theta_3, \vec{k} - \vec{\kappa}_3) \end{pmatrix}, \quad (3.8)$$

where

$$h_\ell(\theta_\ell, \vec{k}) = \gamma \begin{pmatrix} 0 & f(R(\theta_\ell)\vec{k}) \\ f^*(R(\theta_\ell)\vec{k}) & 0 \end{pmatrix}, \quad (3.9)$$

is the single layer graphene Hamiltonian with hoppings between graphene's sublattices given as $f(\vec{k}) = e^{-i2a_0k_y/3} + 2e^{ia_0k_y/3} \sin(a_0k_x/\sqrt{3} - \pi/6)$, $R(\theta_\ell)$ as the rotation matrix in the layer plane, and $\gamma = \hbar v_F/a_0 = 2.364$ eV is the strength of the interlayer hopping, where $v_F = 10^6$ m/s is the Fermi velocity and $a_0 = 0.246\text{\AA}$ is the lattice constant [209]. Here, we used the bounded tight binding form of $f(\vec{k})$ for single layer graphene rather than a linearized dispersion used in Ref. [208] because bounded Hamiltonians are more well-behaved for the purposes of Floquet theory.

The Hamiltonian above can be used to model the various possible configurations of twisted trilayer graphene we will consider. Particularly at twist angle θ , a top layer twist (TLT) can be modelled with parameter choices $\theta_1 = -\theta_2 = -\theta_3 = \theta/2$, $\vec{\kappa}_1 = \vec{\kappa}_-$ and $\vec{\kappa}_{2,3} = \vec{\kappa}_+$ where $\vec{\kappa}_\pm = \frac{k_\theta}{2} (-\sqrt{3}, \pm 1)$ and $k_\theta = 8\pi \sin(\theta/2)/3a_0$. Similarly, for a middle layer twist (MLT), one would have to set $\theta_1 = -\theta_2 = \theta_3 = \theta/2$, $\vec{\kappa}_{1,3} = \vec{\kappa}_-$ and $\vec{\kappa}_2 = \vec{\kappa}_+$.

The $\vec{\kappa}_\pm$ shifts were introduced into the Hamiltonian through a unitary transformation that ensures that the momenta in all three layers are measured with respect to the Γ point in the moiré Brillouin zone seen in Fig. 3.1. This transformation is also the reason why our $T(\vec{x})$ matrices, where x is the spatial coordinate, at first glance seem to differ by the choice of \vec{q} vectors from those used in [208] as we will see below. The advantage of this approach is that an expansion of the Hamiltonian in terms of plane waves can be done in a conventional way (without the need to introduce additional phases for the different layer components of the wavefunction). In our case, the T matrices for a middle twist are given as $T_{12}(\vec{x}) = \sum_{\ell=1}^3 e^{-i\vec{q}_\ell \cdot \vec{x}} T_\ell$, $T_{23}(\vec{x}) = \sum_{\ell=1}^3 e^{+i\vec{q}_\ell \cdot \vec{x}} T_\ell$. The case of a top twist differs in that $T_{23}(\vec{x}) = \sum_{\ell=1}^3 T_\ell$. In addition, we have $\vec{q}_{1,2} = \frac{\sqrt{3}k_\theta}{2} (\pm 1, \sqrt{3})$ and $\vec{q}_3 = (0, 0)$. Finally, the matrices T_ℓ are

defined as follows [208]

$$T_\ell^{AB} = [T_\ell^{BA}]^\dagger = \begin{pmatrix} w_0 e^{i\frac{2\ell\pi}{3}} & w_1 \\ w_1 e^{-i\frac{2\ell\pi}{3}} & w_0 e^{i\frac{2\ell\pi}{3}} \end{pmatrix}, \quad (3.10)$$

$$T_\ell^{AA} = \begin{pmatrix} w_0 & w_1 e^{-i\frac{2\ell\pi}{3}} \\ w_1 e^{i\frac{2\ell\pi}{3}} & w_0 \end{pmatrix} \quad (3.11)$$

where the superscripts refer to the type of stacking we have which can be AA , AB , or BA stacking. We choose the tunneling parameters $w_1 = 110$ meV and $w_0 \approx 0.8w_1$ so that they are close to those in twisted bilayer graphene where distortions in a relaxed lattice can be modelled this way [145, 203], which is expected to happen for twisted trilayer graphene if we neglect next nearest layer interactions.

To provide a reference for our discussion of the non-equilibrium case, we remind the reader of some equilibrium properties of twisted trilayer graphene. We plotted the band structure for the AAA and ABC stacked twisted trilayer graphene with top and middle layers twisted as shown in Fig. 3.2. We have omitted the ABA stacking case because we find that top layer twisted ABA TTG has a band structure that for small twist angles is equivalent to the top layer twisted ABC case. Similarly, the middle layer twisted ABA case has a band structure that is equivalent to middle layer twisted AAA TTG. This phenomenon is similar to twisted bilayer graphene where for small twist angles it does not matter whether one started from AA stacking or AB stacking. This property is also preserved once we introduce circularly polarized light and longitudinal light coming from a waveguide.

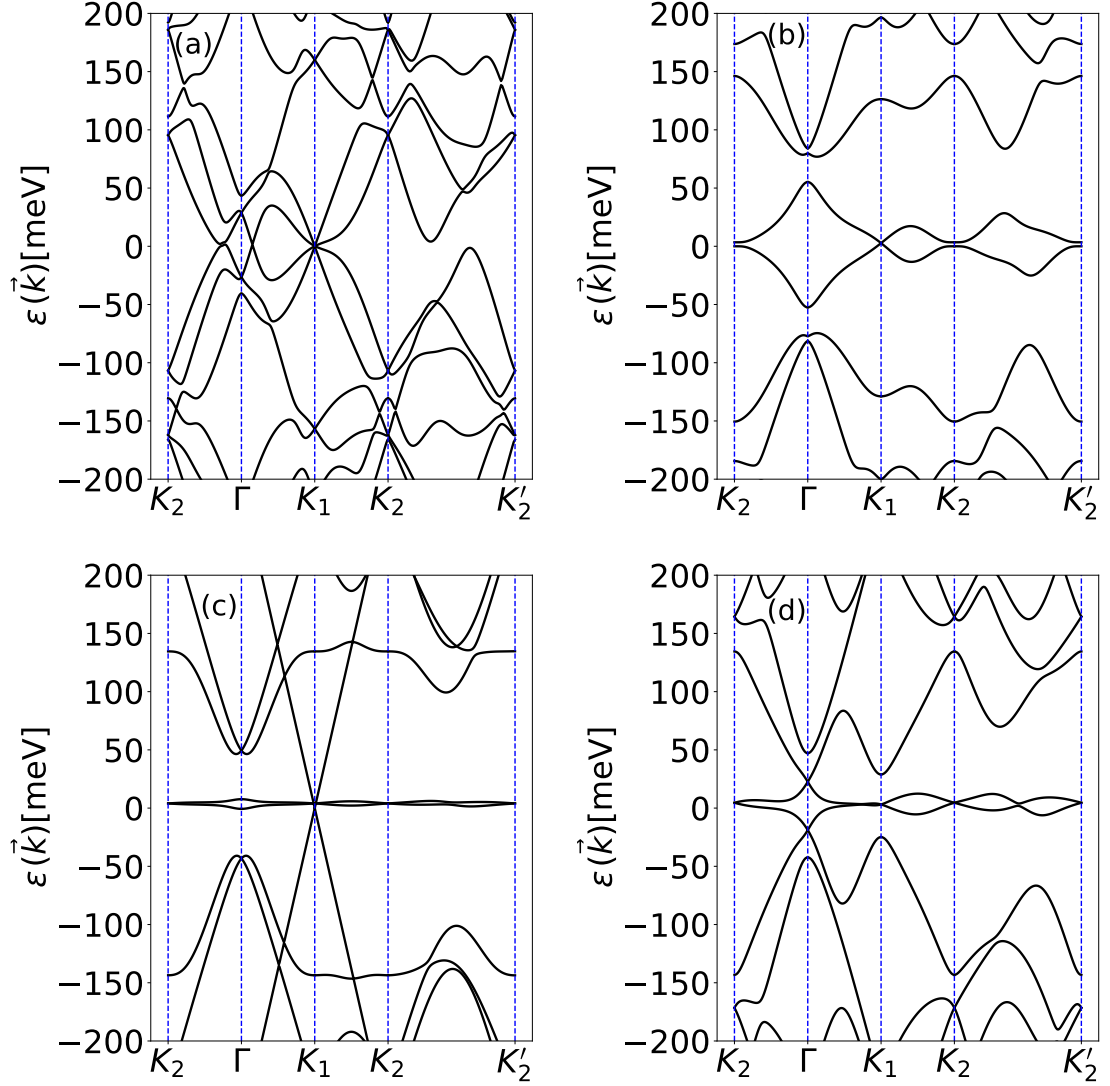


Figure 3.2: Band structure of the TTB with equilibrium Hamiltonian (Eq. 3.8) top layer twisted (top row) and middle layer twisted (bottom row) with twist angle $\theta = 1.6^\circ$. (a,c) Starting from AAA stacking and (b,d) starting from ABC stacking [2].

3.2.3 TTLG Under the Influence of Circularly Polarized Light

If this light is applied perpendicular to the graphene layers, at frequency ω and driving strength A , then we include its effect in a semi-classical fashion - assuming large photon numbers- by making use of the minimal substitution prescription $k_x \rightarrow k_x - A \cos(\omega t)$ and $k_y \rightarrow k_y - A \sin(\omega t)$ [169]. Thus, we have a time-periodic Hamiltonian satisfying $H(\vec{x}, \vec{k}, t) = H(\vec{x}, \vec{k}, t + 2\pi/\omega)$. We should mention that small deviations from normal incidence leads to small corrections in the high-frequency limit, which is the case in this work, and thus it can be neglected. For a study of oblique incidence light in bilayer graphene, see [210]. In the next few sections we discuss our numerical results for both band structure and topological phase diagrams of the TTLG under the influence of this form of light.

3.2.3.1 Numerical results of the band structure using the quasi-operator approach

In this section we study the effects that circularly polarized light has on the band structure of the various twisted trilayer graphene systems. To do this we evaluate the Floquet-Schrödinger equation (3.6) numerically.

In Figs. 3.3 & 3.4 we plotted the band structure for different driving strengths, driving frequencies and twist angles in the vicinity of the magic angle of the TTG. We show both the driven case as well as the undriven case to allow for a comparison. The cases we consider are twisted configurations that start from both AAA and ABC stacking and in each case we consider both top layer and middle layer twists.

An interesting effect of circularly polarized light is that for certain choices of the twist angle, driving strength A and the driving frequency ω , one can flatten the central bands making it a very interesting candidate for strongly correlated phases because one can expect interactions to be dominant in this case. For example, in Fig. 3.4 (a),

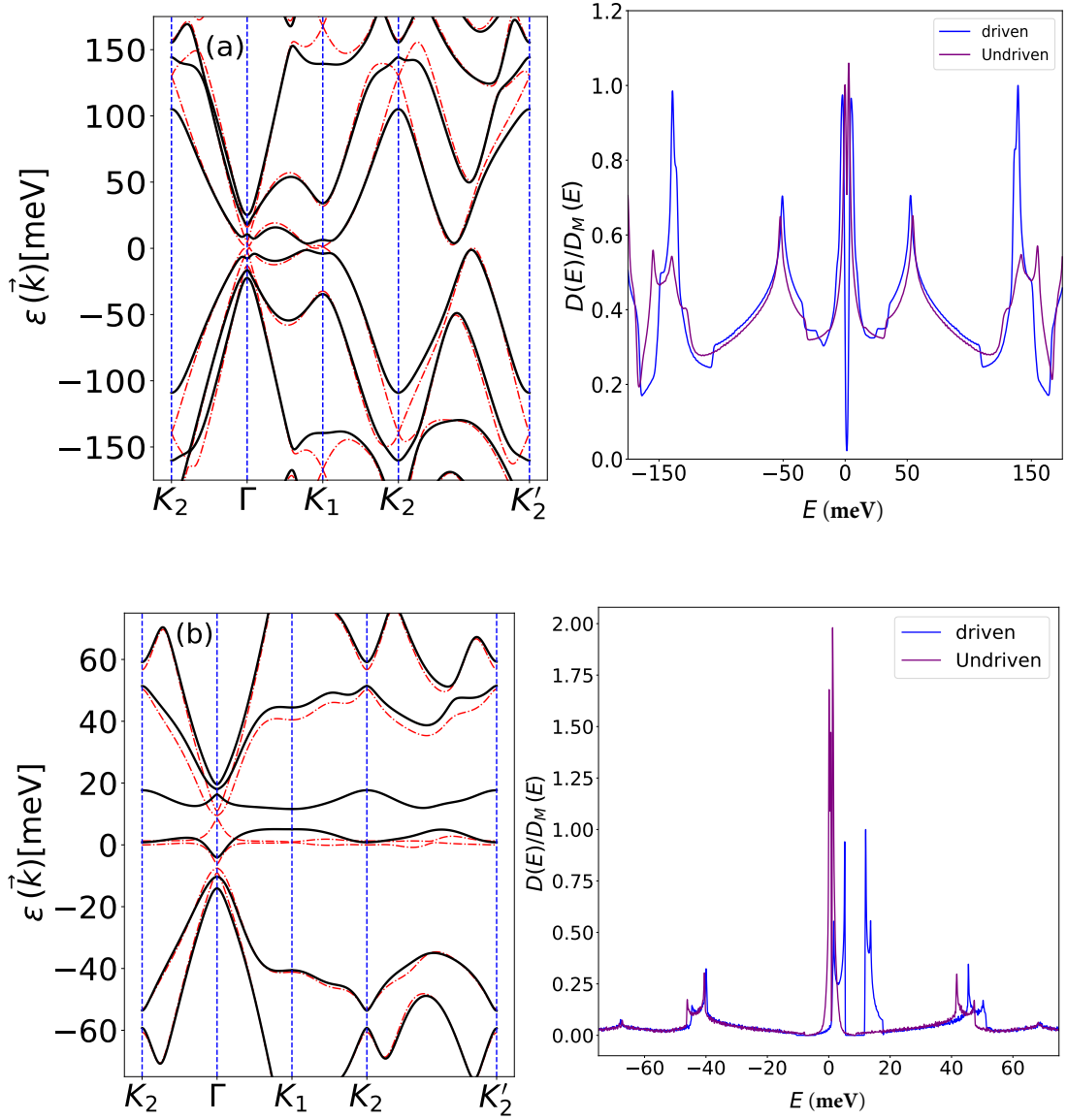


Figure 3.3: Band structure (left column) for TTLG driven by circularly polarized light. (a) Starting with AAA stacking with TTLG and parameters $(\theta, Aa_0, \omega) = (1.8^\circ, 0.25, 2\gamma)$, and (b) the ABC with TTLG and $(\theta, Aa_0, \omega) = (1.0^\circ, 0.15, 3\gamma)$. In the above plots, the dash-dotted lines represent the undriven case and the solid lines represent the driven case. The corresponding density of states plots (DOS) are on the right column rescaled by $D_M(E)$ which is the maximum value of the DOS of the driven case [2].

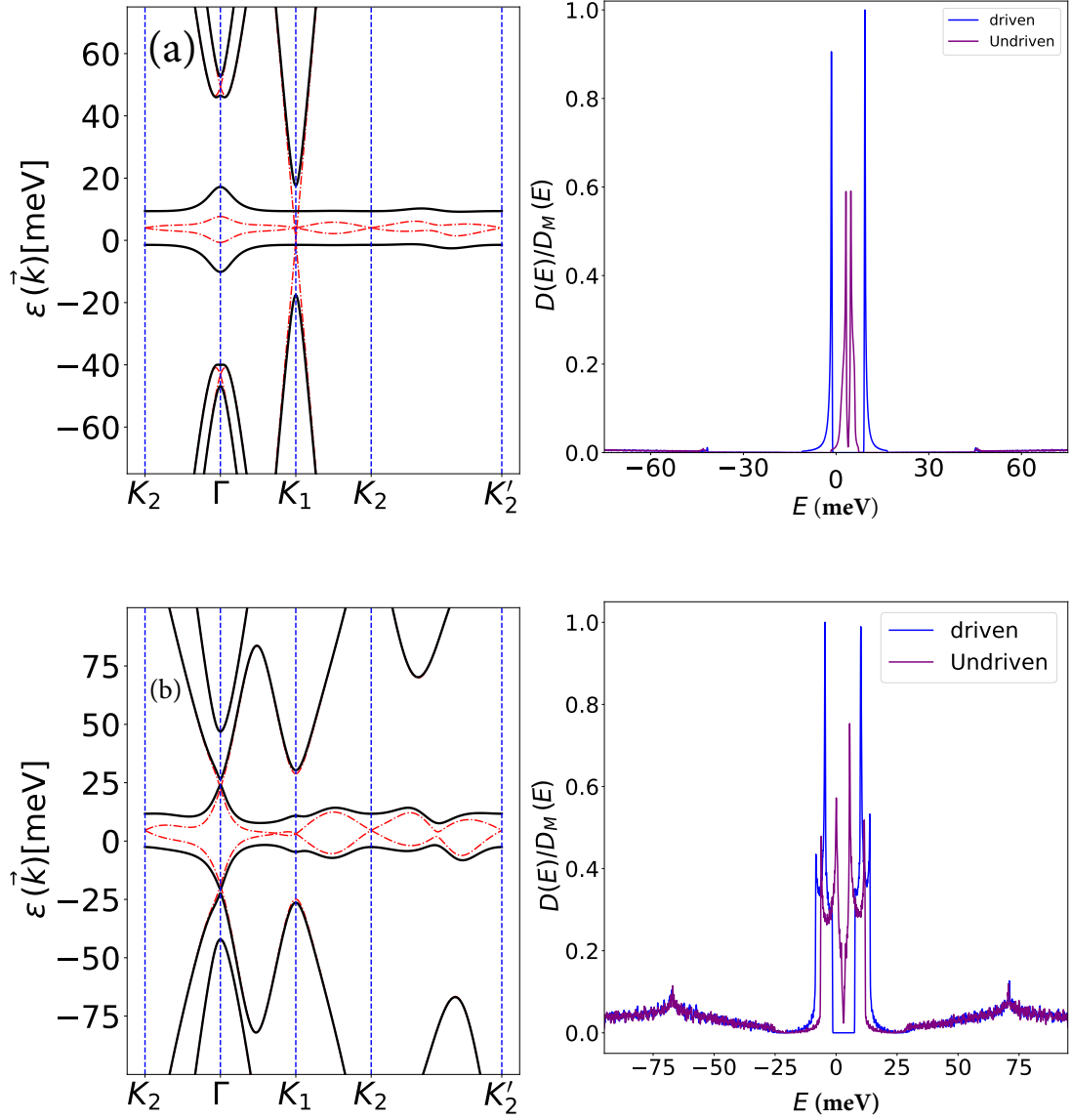


Figure 3.4: Reproduction of Fig. 3.3 for the case of middle layer twist (MLT). (a) AAA stacking with $(\theta, Aa_0, \omega) = (1.6^\circ, 0.15, 3\gamma)$, and (b) ABC configuration for the parameters $(\theta, Aa_0, \omega) = (1.6^\circ, 0.15, 3\gamma)$ [2].

we see that the two middle bands are less dispersive than their equilibrium counterparts. We observe that not all configurations in Figs. 3.3 & 3.4 yield less dispersive bands such as the case of AAA stacked top layer twist. The effect depends on the relative location of the Dirac cones, and subsequent hybridization due to interlayer couplings. In the same figure, we also plotted the density of states associated with each case. The plots reflect the flattening of the bands via the appearance of sharper peaks as can be seen in the case of AAA stacking with a middle layer twist. Moreover, Figs. 3.3 & 3.4 show the appearance of gap openings which is another rationale for using this type of light. Consequently, this opens up the possibility to discuss topological effects that are characterized by the Chern number of isolated bands. Since we work in the high frequency regime (the driving frequency is larger than the bandwidth of the model Hamiltonian) this allows access to information about topological edge states [211]. This is unlike the low frequency regime that requires the calculation of the winding numbers for a proper description of band topology - in this regime the connection between relative Chern numbers and number of edge states is not immediate anymore. Since such calculations can be computationally very expensive when working with the full quasi-energy operator, it will turn out to be convenient to rely on approximate time independent Floquet Hamiltonians that will be introduced in next two sections.

3.2.3.2 Band structure via the Van-Vleck approximation

It will be useful to linearize the Hamiltonian (3.8). However, since we want to capture the effect of periodic drive as accurately as possible instead of just linearizing by a Taylor expansion we first expand the Hamiltonian to first order in a Fourier series

and subsequently linearize it in momenta. The result is that

$$f(\vec{k} - \vec{A}) \approx a_0(k_x - ik_y)J_0(2Aa_0/3) + 3J_1(2Aa_0/3)e^{i\omega t} \quad (3.12)$$

where $J_n(x)$ is the Bessel function of the first kind. We use this approximation in (3.8) along with the second order Van-Vleck approximation (VVA) Eq. 3.7. As an illustration, we compare the results from VVA and with those obtained from truncation of Eq. 3.6 as shown in Fig.3.5.

3.2.3.3 The rotating frame effective Hamiltonian

An alternative but non-perturbative scheme is to transform to a rotating frame (RF) Hamiltonian $H_R = U(t)^\dagger(H - i\partial_t)U(t)$ that has a less important time dependence than the original Hamiltonian. A subsequent time average yields a Hamiltonian that is more accurate than the vV Hamiltonian. It cannot be stressed enough that special care has to be taken in that the rotating frame transformation is chosen such that the terms that are neglected in the time average do not cause breaking of the six-fold rotational symmetry in momentum space. Here, we provide a simple generalization of the unitary transformation that was introduced in [169] and that fulfills this property. We start with linearized dispersion $f(\vec{k})$ Eq. 3.12 in the full Hamiltonian, the time dependent Hamiltonian becomes $H(x, \vec{k}, t) = H(x, \vec{k}) + V(t)$. The unitary transformation can be proposed in the form [169] $U_R(t) = e^{-i \int dt V_1(t)} e^{-i \int dt V_2(t)}$ with a properly chosen decomposition of the time periodic part of the Hamiltonian $V(t) = V_1(t) + V_2(t)$. Here, $V_1(t)$ is the part of the Hamiltonian that is $\propto \cos(\omega t)$, while $V_2(t)$ is $\propto \sin(\omega t)$.

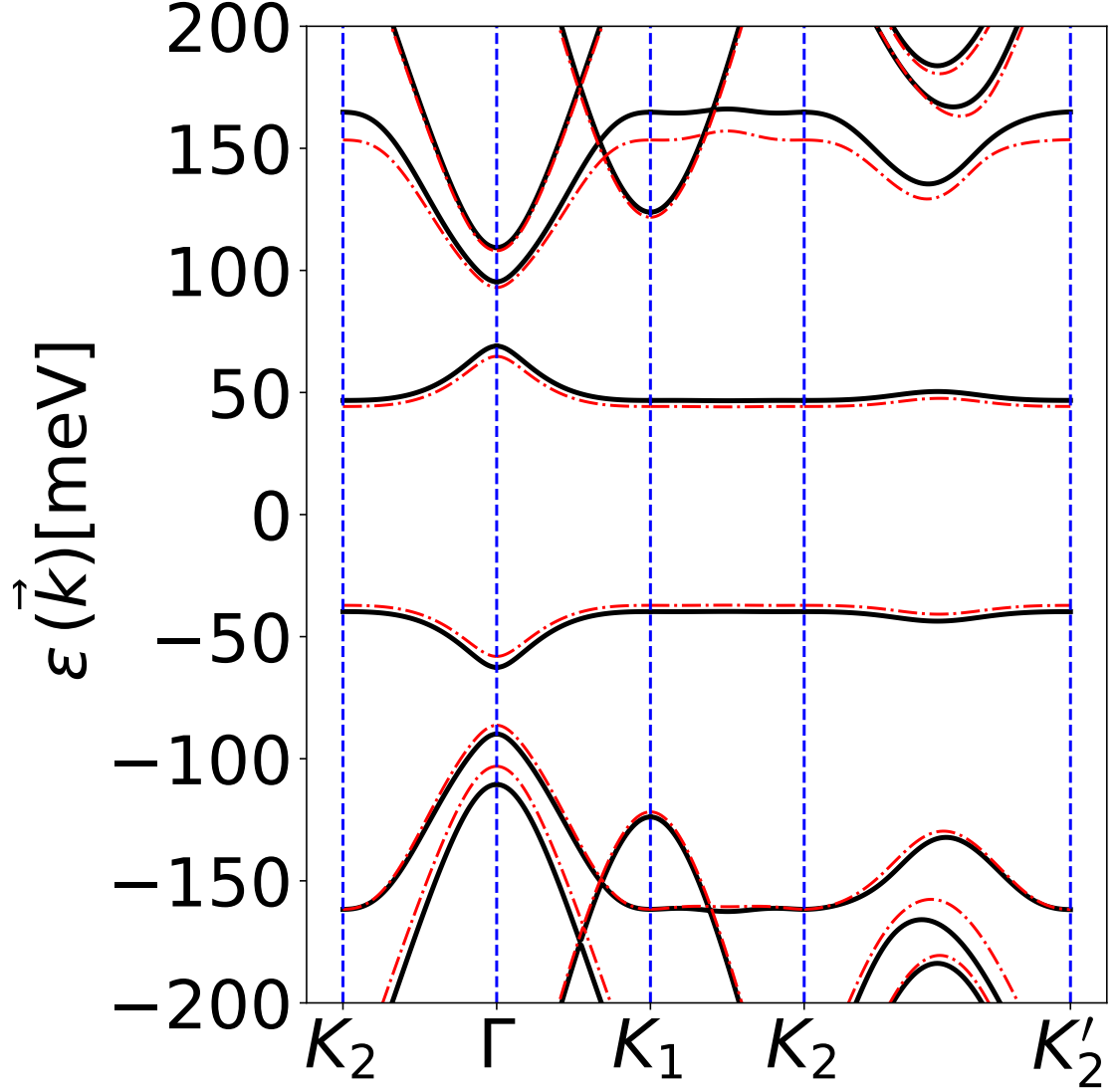


Figure 3.5: Comparison between the exact quasi-energies and the energies from the VVA for the band structure of the TTLG with AAA stacking and middle layer twisted, driven by circularly polarized light $\theta = 1.6^\circ$, $Aa_0 = 0.4$, and $\Omega = 3\gamma$. Here solid lines represent the VVA results and the dashed lines are the exact quasi-energies Eq. 3.6.

The transformation then is given as

$$\begin{aligned}
U_R(t) &= \text{diag}[u_R(\theta_1, t), u_R(\theta_2, t), u_R(\theta_2, t)] \\
u_R(\theta, t) &= u_{R,1}(\theta, t)u_{R,2}(\theta, t) \quad , \\
u_{R,n} &= \cos[\gamma_n(t)] - i \sin[\gamma_n(t)]\sigma_n^\theta
\end{aligned} \tag{3.13}$$

where $\gamma_1(t) = B_\Omega \sin(\omega t)$, $\gamma_2(t) = B_\Omega(1 - \cos(\omega t))$, $B_\Omega = 3J_1(2Aa_0/3)\gamma/\Omega$ and appropriately rotated Pauli matrices are given as $\sigma_n^\theta = e^{-i\theta/2\sigma_3}\sigma_n e^{i\theta/2\sigma_3}$.

After taking the time average we arrive at an effective Hamiltonian $H_{\text{eff}}^{(\text{bare})}$, which still has a form that is too cumbersome to display here and is hard to interpret. Therefore we apply another unitary transformation that is given by

$$R = \text{diag}[e^{iB_\Omega\sigma_2^{\theta_1}}, e^{iB_\Omega\sigma_2^{\theta_2}}, e^{iB_\Omega\sigma_2^{\theta_3}}], \tag{3.14}$$

where we used definitions for rotated Pauli matrices from above. Consequently, we calculate our effective Hamiltonian in the rotating frame as

$$H(\vec{x}, \vec{k}) = \begin{pmatrix} \tilde{h}(\theta_1, \vec{k} - \vec{\kappa}_1) & \tilde{T}_{12}(\vec{x}) & 0 \\ \tilde{T}_{12}^\dagger(\vec{x}) & \tilde{h}(\theta_2, \vec{k} - \vec{\kappa}_2) & \tilde{T}_{23}(\vec{x}) \\ 0 & \tilde{T}_{23}^\dagger(\vec{x}) & \tilde{h}(\theta_3, \vec{k} - \vec{\kappa}_3) \end{pmatrix}, \tag{3.15}$$

where the single layer graphene blocks are modified as follows

$$\tilde{h}(\theta, \vec{k}) = a_0\gamma_{\text{RF}}R(\theta)\vec{k} \cdot \vec{\sigma} - \Delta_{\text{RF}}\sigma_3, \tag{3.16}$$

the interlayer hoppings become

$$\gamma_{\text{RF}} = \gamma J_0 \left(-\frac{6\gamma}{\Omega} J_1 \left(\frac{2Aa_0}{3} \right) \right) J_0 \left(\frac{2Aa_0}{3} \right) \tag{3.17}$$

and a Dirac gap that is given as

$$\Delta_{\text{RF}} = -\frac{3\gamma}{\sqrt{2}} J_1\left(\frac{2Aa_0}{3}\right) J_1\left(-\frac{6\sqrt{2}\gamma}{\Omega} J_1\left(\frac{2Aa_0}{3}\right)\right) \quad (3.18)$$

is introduced.

The effective tunneling matrices are modified as follows: We first recognize that the original hopping matrices T_{ij} can be expressed in terms of Pauli matrices as $T_{ij} = T_{ij}^0\sigma_0 + T_{ij}^1\sigma_1 + T_{ij}^2\sigma_2 + T_{ij}^3\sigma_3$, where T_{ij}^n are expansion coefficients. The modified interlayer hopping matrices \tilde{T}_{ij} are then found if we replace the Pauli matrices by new matrices $\sigma_i \rightarrow \tilde{\sigma}_i$. That is we have $\tilde{T}_{ij} = T_{ij}^0\tilde{\sigma}_0 + T_{ij}^1\tilde{\sigma}_1 + T_{ij}^2\tilde{\sigma}_2 + T_{ij}^3\tilde{\sigma}_3$, where $\tilde{\sigma}_{1,2} = J_0(\nu)\sigma_{1,2}$ and

$$\tilde{\sigma}_0 = \sigma_0 + (J_0(\sqrt{2}\nu) - 1) \left[\sigma_0 \sin^2\left(\frac{\theta_i - \theta_j}{2}\right) - \frac{i}{2}\sigma_3 \sin(\theta_i - \theta_j) \right], \quad (3.19)$$

$$\tilde{\sigma}_3 = \sigma_3 + (J_0(\sqrt{2}\nu) - 1) \left[\sigma_3 \cos^2\left(\frac{\theta_i - \theta_j}{2}\right) + \frac{i}{2}\sigma_0 \sin(\theta_i - \theta_j) \right], \quad (3.20)$$

with $\nu = (-6\gamma/\omega)J_1(2Aa_0/3)$.

This Hamiltonian offers a huge reduction in computational cost when compared to the exact case where the quasi-energy operator - if we include a large number of Fourier modes - is very large. The approximation offers highly reliable results for the experimentally accessible range of driving strengths in the high frequency regime. For illustration, we compare the rotating frame Hamiltonian results with those obtained from Eq. 3.6 in Fig. 3.6.

Comparing Fig. 3.5 with Fig. 3.6, we find that the rotating frame effective Hamiltonian is systematically closer to the exact quasi-energy than the truncated Van Vleck Hamiltonian. To further quantify the efficiency of both approximations and get a feel

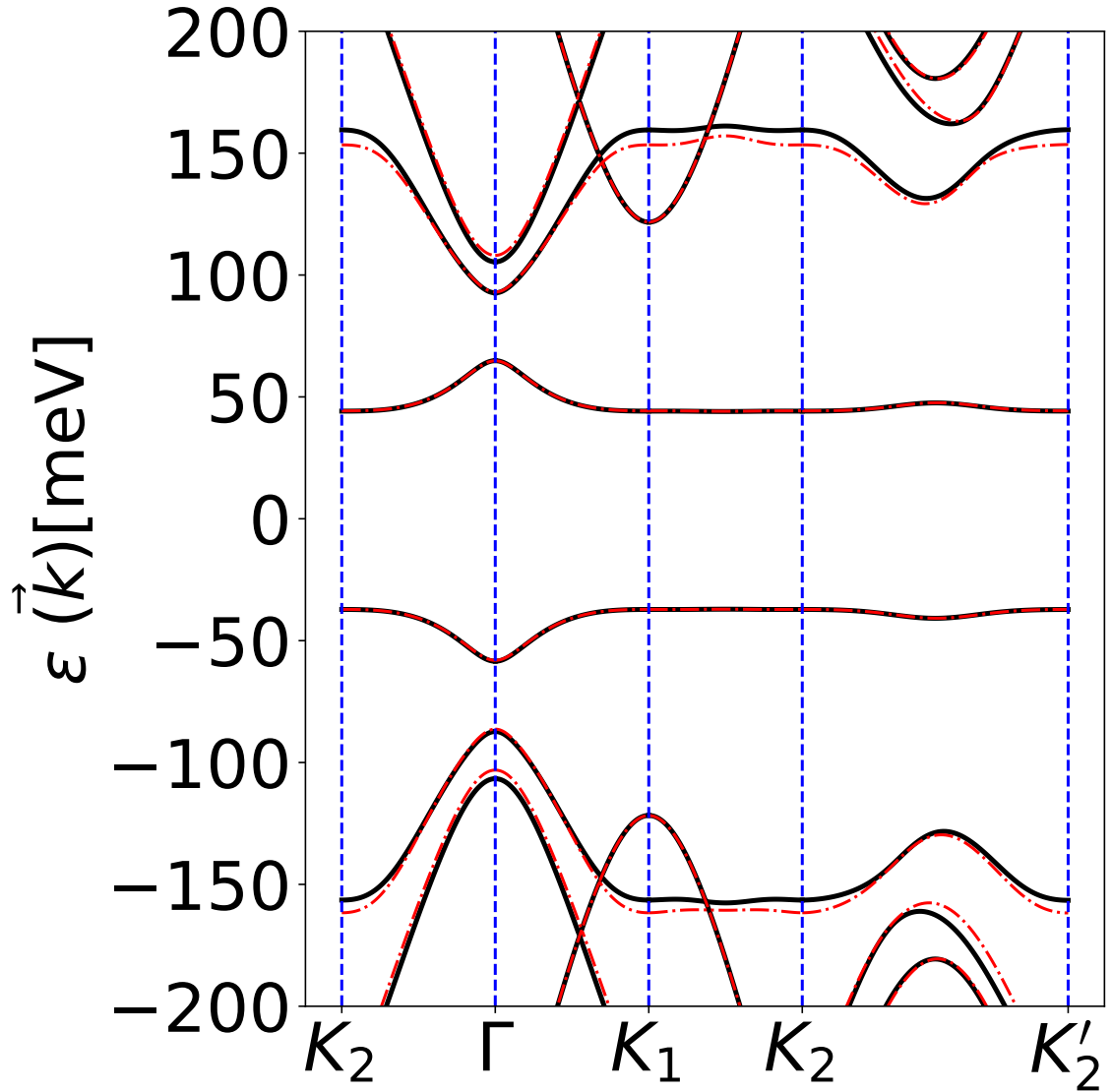


Figure 3.6: Comparison between the exact quasi-energies and the energies from the rotating frame Hamiltonians for the band structure of the TTLG with AAA stacking and middle layer twisted, driven by circularly polarized light $\theta = 1.6^\circ$, $Aa_0 = 0.4$, and $\Omega = 3\gamma$. Here, the solid lines represent rotating frame results while the dashed lines represent the *exact* results.

for their range of validity, we computed the relative error in the center gap at the K_1 point for both methods and plotted the result as a function of driving strengths and frequencies as shown in Fig. 3.7.

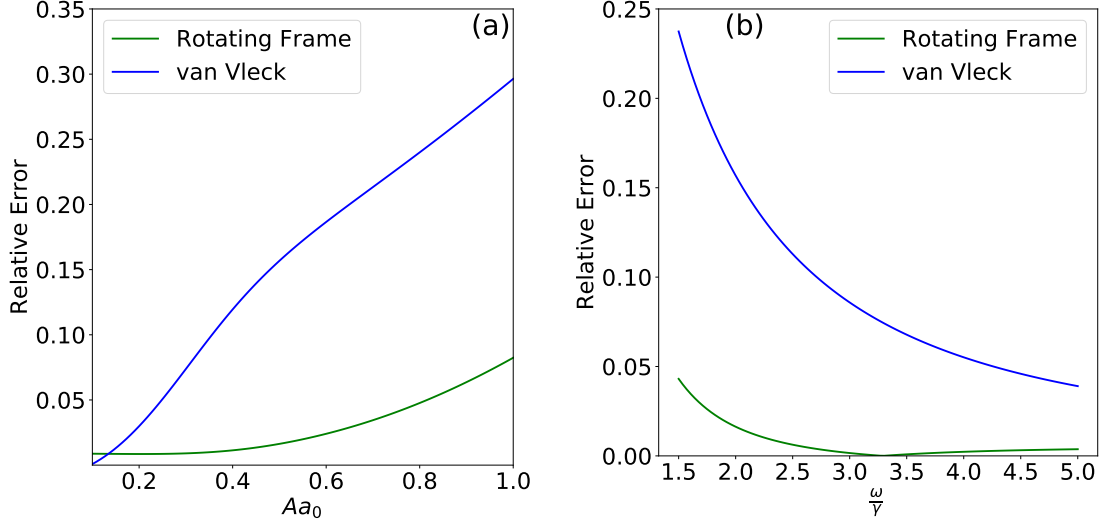


Figure 3.7: Plot of relative error for the gap at the K_1 symmetry point for the TTG system with AAA stacking and middle layer twisted driven by circularly polarized light (a) as function of Aa_0 , with $\theta = 1.6^\circ$, and $\Omega = 2\gamma$, (b) and as a function of ω/γ with $Aa_0 = 0.5$.

3.2.3.4 Topological phase diagrams

Next, we make use of the rotating frame Hamiltonian to compute maps of Chern numbers. First, however, let us give a brief summary of the algorithm due to Fukui [211] that we used in our computations.

To compute the Chern number we divide the moiré Brillouin zone into uniform small rectangles of size $dk_x \times dk_y$. Then we compute the so-called link variables $U_{\vec{k}_j \hat{u}}^{(\ell)}$ [211],

$$U_{\vec{k}_j \hat{u}}^{(\ell)} = \frac{\langle \psi^{(\ell)}(\vec{k}_j) | \psi^{(\ell)}(\vec{k}_j + \hat{u}) \rangle}{|\langle \psi^{(\ell)}(\vec{k}_j) | \psi^{(\ell)}(\vec{k}_j + \hat{u}) \rangle|} \quad (3.21)$$

where $\psi^{(\ell)}(\vec{k}_j)$ is the eigenvector of the Hamiltonian corresponding to the band with

index ℓ , and $\hat{u} := \hat{u}_x = (dk_x, 0)$ or $\hat{u} := \hat{u}_y = (0, dk_y)$. Next, we calculate the field strength [211]

$$F_{\vec{k}_j}^{(\ell)} = \ln \left[U_{\vec{k}_j \hat{u}_x}^{(\ell)} U_{\vec{k}_j + \hat{u}_x, \hat{u}_y}^{(\ell)} U_{\vec{k}_j + \hat{u}_x + \hat{u}_y, \vec{k}_j + \hat{u}_y}^{(\ell)} U_{\vec{k}_j + \hat{u}_y, \vec{k}_j}^{(\ell)} \right]. \quad (3.22)$$

Finally, the Chern number for the ℓ th band is given as

$$c_\ell = \frac{1}{2\pi i} \sum_{\vec{k}_j} F_{\vec{k}_j}^{(\ell)}, \quad (3.23)$$

where the sum is taken over all plaquettes in the Brillouin zone.

In this study, we restrict ourselves to the topology of the six central bands and we use the rotating frame Hamiltonian to be able to compute Chern numbers sufficiently quickly. We have spot-checked our results against results that we obtained when we were working with the full quasi-energy operator. Since we work in the high frequency regime, where the frequency is larger than the bandwidth of the included bands, it is sufficient to consider the Chern numbers to learn more about topological properties. We computed Chern numbers for the six central bands and for various values of the driving strength Aa_0 and the twist angle θ at a fixed driving frequency $\omega = 2\gamma$. The resulting topological phase diagrams are shown in Fig.3.8. Due to the high computational cost, we limited ourselves to driving strengths between $Aa_0 = 0$ and $Aa_0 = 0.3$ (this for frequencies larger than the bandwidth which is the experimentally favorable regime), and twist angle ranging from 1.5° to 2.85° .

Each color in the diagrams represents a list of Chern numbers for the six central bands $C = \{c_1, c_2, c_3, c_4, c_5, c_6\}$. Mathematically, if we have N bands $\{\varepsilon_i(\vec{k})\}_{i=0}^{i=N}$, then the six bands are $\varepsilon_{N/2-3}(\vec{k})$, $\varepsilon_{N/2-2}(\vec{k})$, $\varepsilon_{N/2-1}(\vec{k})$, $\varepsilon_{N/2}(\vec{k})$, $\varepsilon_{N/2+1}(\vec{k})$, and $\varepsilon_{N/2+2}(\vec{k})$. As an illustration, we plotted the band structure for the ABC stacking case with middle layer twist in Fig. 3.9, where we labeled the six central bands. We have

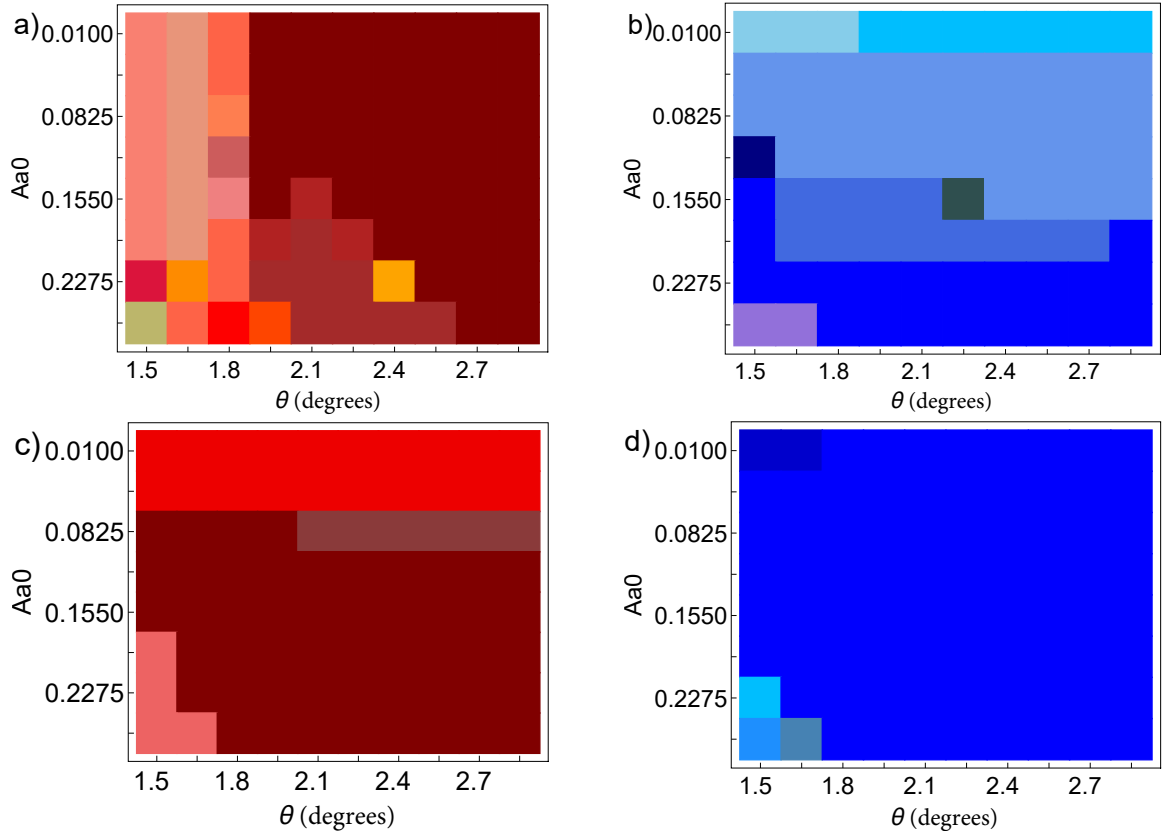


Figure 3.8: (Color online) The topological phase diagrams for the TTG system for a range of values Aa_0 and the twist angle θ with $\omega = 2\gamma$. (a) AAA stacking and top layer twist, (b) ABC stacking with top layer twisted, (c) AAA stacking with middle layer twisted, and (d) ABC stacking with middle layer twisted. Each color represents a set of values for the Chern numbers of the central six bands as indicated in Table. 3.1.

tabulated the corresponding values for each color in Table 3.1.

We find that each of the different TTLG realizations has its own unique topological structure. The bands in most cases - except for the AAA middle twist - are also found to be gapped. Quite generally, we find a rich structure of Chern numbers and for certain parameter pairs (Aa_0, θ) we find very large Chern number of 4 or 5 for some of the bands.

For all cases except the ABC top twist we find that the handedness of the incident circularly polarized light has no influence on the topological structure. In Fig.3.10 we see that for this case, however, there are large changes in the topological structure if we change from left handed (LH) to right handed (RH) circularly polarized light.

3.2.3.5 Experimental proposal

Motivated by the rich topological structure of the different types of TTGs (see Fig. 3.8), and the different responses of ABC to left and right-handed light we also propose the following experiment: For a large-enough ABC TTG sample, we shine light with opposite handedness next to each other, as depicted in Fig. 3.11. By bringing the light beam edges very close to each other, we can expect to create three distinct topological regions, one for each laser pulse and one more at the intersection between the laser pulses. From the bulk-edge correspondence, we expect edge states at the boundary between the driven and undriven regions and at boundaries between the topological regions. These boundary states, indicated in blue in Fig. 3.11, could be manifest in optical conductivity measurements [212, 213]. This measurement would require employing a pump-probe experimental setup, where the probe amplitude $a_0 A_{\text{probe}}$ is weak compared with the pump pulse $a_0 A$ employed to create the Floquet states.








































color	c_1	c_2	c_3	c_4	c_5	c_6
AAA top layer twisted						
	-5	3	-1	1	-3	5
	-5	3	-1	1	0	2
	-4	1	0	0	-1	4
	-4	1	0	0	2	1
	-4	2	-1	1	0	2
	-3	0	0	0	2	1
	-2	0	-1	1	0	2
	-2	0	2	-2	0	2
	-2	3	-1	1	-3	2
	-2	3	-1	1	0	-1
	-1	-2	0	0	2	1
	-1	-1	-1	1	1	1
	1	-3	-1	1	3	-1
	1	3	-1	1	-3	-1
	ν	ν	-1	1	0	2
AAA middle layer twisted						
	v	v	0	0	v	v
	v	v	1	-1	v	v
	v	v	1	v	v	v
	v	v	v	v	v	v
ABC top layer twisted(RH)						
	-3	0	-1	2	0	-3
	-3	0	1	0	0	-3
	-3	0	2	-1	0	-3
	-2	0	-1	2	0	-3
	-2	0	-1	2	1	-4
	0	0	-1	2	0	-3
	1	-1	0	2	-2	-1
	1	0	-1	2	1	-4
ABC top layer twisted(LH)						
	-4	1	2	-1	0	-3
	-4	1	2	-1	0	-2
	-4	1	2	-1	0	1
	-3	0	2	-1	0	-3
	-3	0	2	-1	0	0
	-1	-2	2	-1	0	1
	-1	-2	2	0	-1	1
ABC middle layer twisted						
	-1	0	1	-1	0	1
	-1	1	0	0	2	-2
	0	-1	1	-1	1	0
	0	-1	1	-1	1	ν
	2	-3	1	-1	3	-2

Table 3.1: Color codes for the topological phase diagrams Figs. 3.8&3.10. Here, the term v represents a band closing that was confirmed up to numerical accuracy. The term ν corresponds to a Chern number that did not converge even when more than 10^4 k points were used in the Chern number computation. RH: right-handed polarized light, and LH: left handed polarized light.

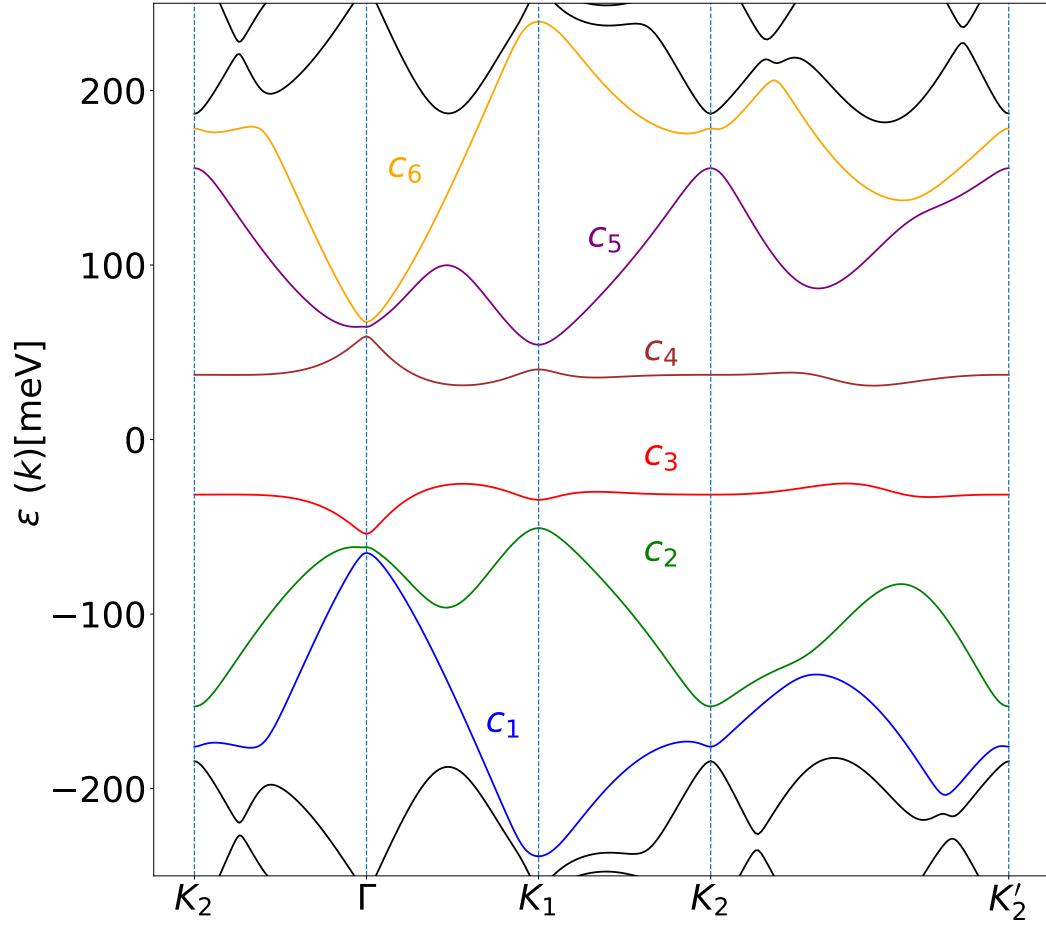


Figure 3.9: Band structure for the ABC MLT showing the six bands labeled $c_1 \rightarrow c_6$. Parameters $Aa_0 = 0.26375$, $\theta = 1.65^\circ$ and $\omega = 2\gamma$ were chosen for the plot.

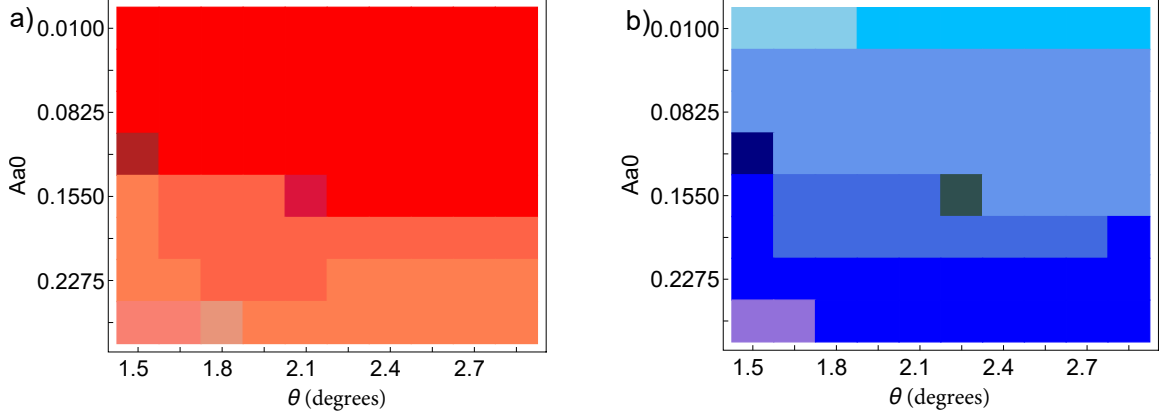


Figure 3.10: (Color online) The topological phase diagrams for the TTG system with ABC stacking and top layer twisted where (a) for the left-handed circularly polarized light and (b) the right-handed circularly polarized light, where we took $\omega = 2\gamma$. For color codes, please refer to Table. 3.1.

3.2.4 The Effect of Waveguide Light on TTLG

In this situation, we have longitudinal light coming from a waveguide. Here, the boundary conditions of a waveguide allow for light with longitudinal components to exist, which is not possible in vacuum [177]. The semi-classical Peierls substitution teaches us how to include a vector potential in a tight binding model [177]. Since our model can be derived from a tight binding model, it becomes clear that the effect of this type of light is included in the Hamiltonian via the substitution $w_0 \rightarrow w_0 e^{-ia_{AA}A \cos(\omega t)}$ and $w_1 \rightarrow w_1 e^{-ia_{AB}A \cos(\omega t)}$, where $a_{AA} = 0.36$ nm and $a_{AB} = 0.34$ nm are interlayer distances in AA and AB regions of the twisted materials [165]. The effect of this type of light therefore is to turn interlayer hoppings time-dependent.

3.2.4.1 Numerical calculations of dispersions

Following the mapping of the tunneling parameters mentioned above, we obtained the band structure numerically by solving equation (3.6) that was truncated to finite order. For all cases the resultant band structure reaches convergence when we include the first 3 Floquet copies ($n = -1, 0, 1$). In Figs.3.12 & 3.13 we plot the band structure

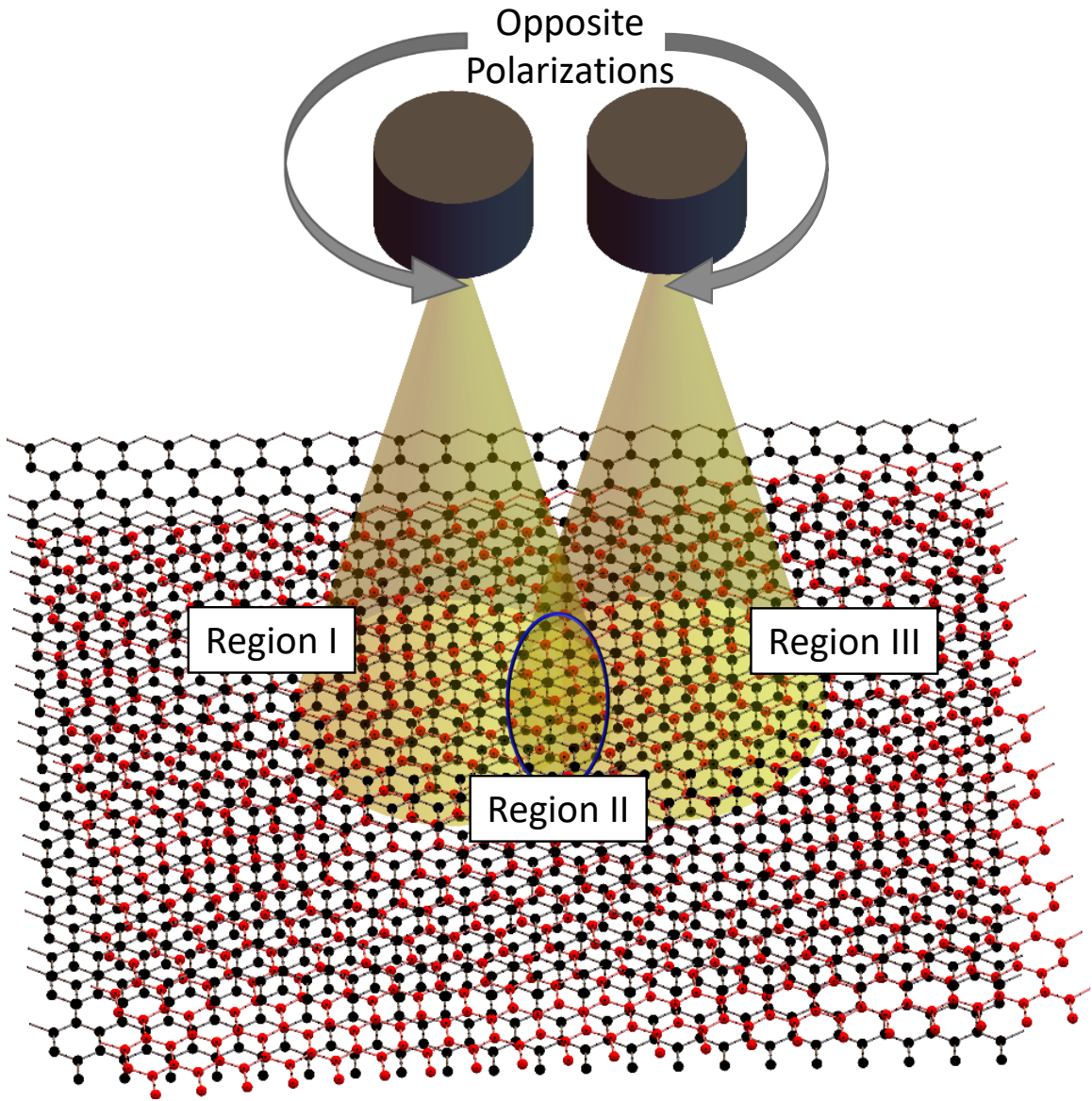


Figure 3.11: Sketch of a two laser procedure to create light-induced topological boundaries in ABC TTLG samples.

for four different configurations (AAA/ABC stacking, top and middle layer twists). For convenience we also include the undriven case for comparison plus the plots of the density of states for each case.

When comparing the ABC case (top and middle layers twists) and the AAA stacking (middle layer twisted) for the undriven (dashed lines) against the driven case (solid lines), we find that we can flatten the central bands without introducing a band opening as in the case of circularly polarized light. This means that we can tune band flatness, which can be convenient when trying to realize strongly correlated phases such as superconductivity.

To understand this effect even better, we have plotted the velocity of electrons near the K_1 symmetry point for the AAA and ABC stacking with middle layer twisted versus θ^{-1} in Fig. 3.14.

We find that the introduction of light from a waveguide can shift the magic angles. This gives us the opportunity to speculate a bit about possible applications. For instance, this observation could be useful in an experiment where one wants to realize strongly correlated phases. This is because when one produces a twisted trilayer graphene sample for use in experiments with strongly correlated phases one has to try to match the magic angle as precisely as possible. If there is a small deviation from the angle with flat bands the setup with waveguide light could be used to correct for these deviations. Alternatively it could even be possible to use light of this sort to switch between strongly correlated phases and other phases.

3.2.4.2 Exact versus Van-Vleck results

Considering the Van-Vleck approximation (Eq. 3.7), we find that in our case the term $\sum_{m \neq 0} \frac{H_m H_{-m}}{m\omega} = 0$ vanishes and therefore the Floquet Hamiltonian is given by $H_F = H_0 + \mathcal{O}(\omega^{-2})$. Consequently, the effective approximate Hamiltonian is obtained

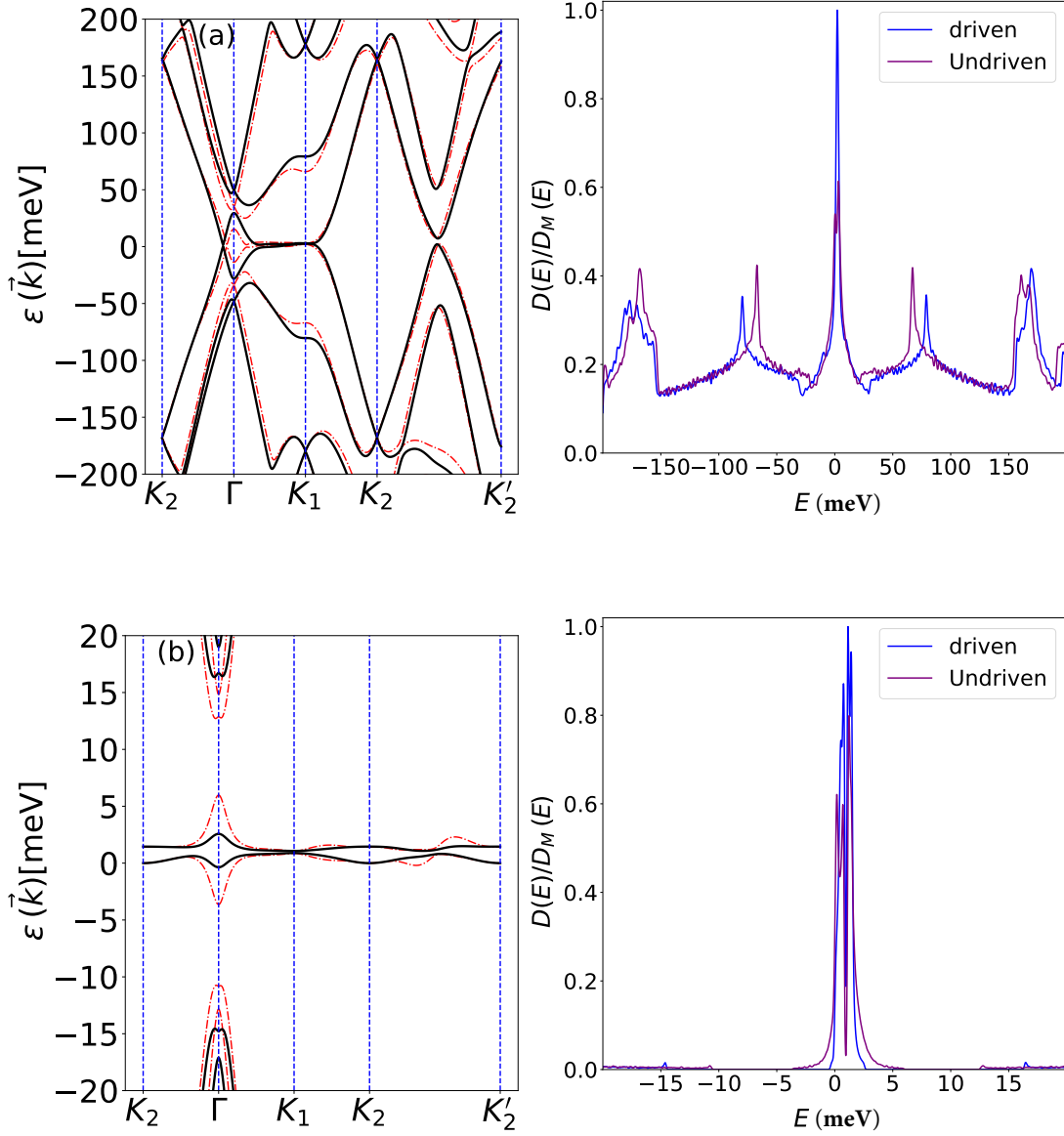


Figure 3.12: Left Column: Band structure of the TTB driven by waveguide light with $Aa_0 = 0.3$. (a) The AAA stacking with TLT and $(\theta, \omega) = (2.000^\circ, 2\gamma)$, (b) the ABC configuration with TLT and $(\theta, \omega) = (1.040^\circ, 2\gamma)$. The solid lines are for the driven and the dash-dotted lines for the undriven case. Right Column: The density of states plots associated with the configurations on the left column rescaled by the maximum value $D_M(E)$ of the driven case.

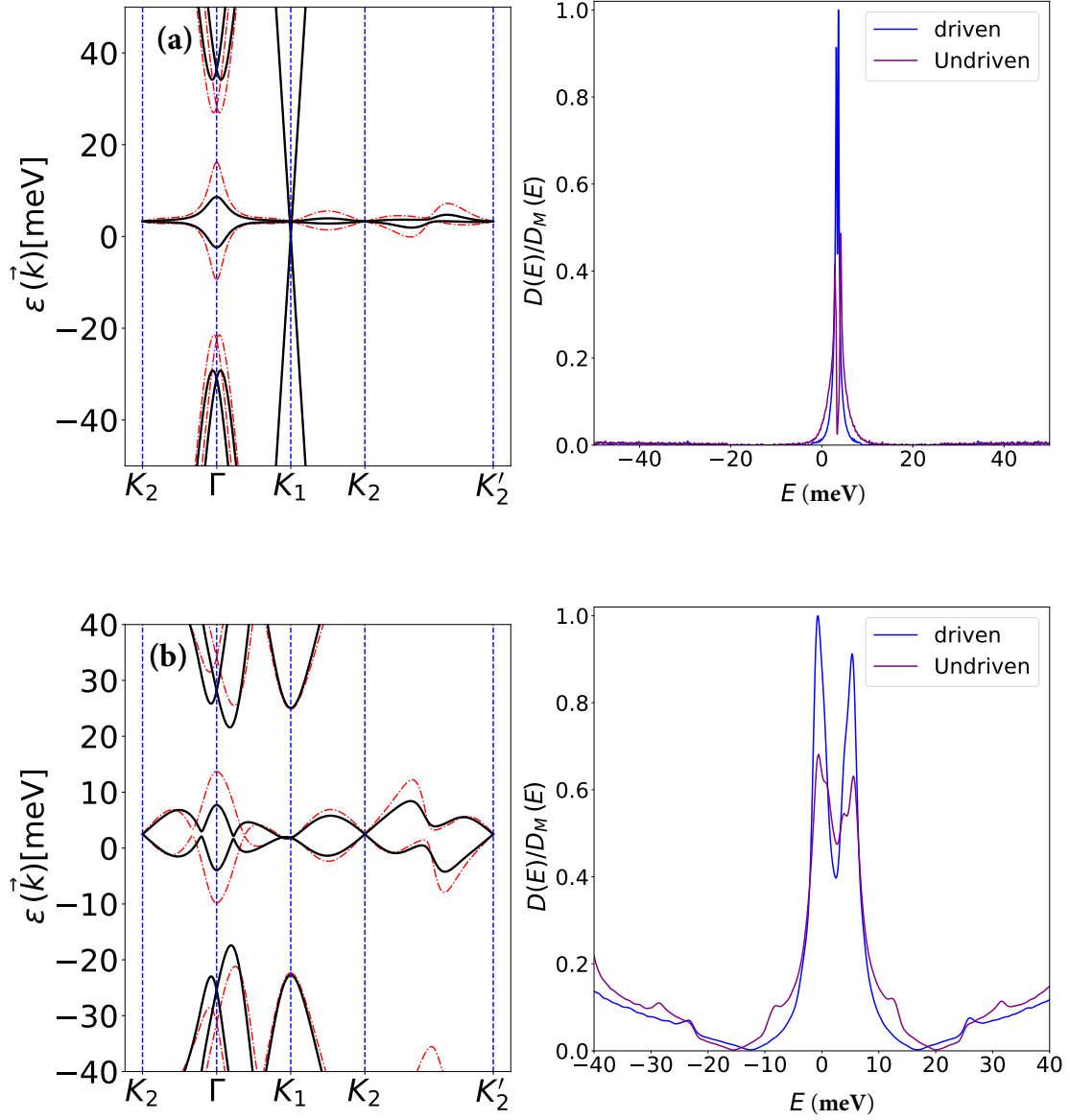


Figure 3.13: Left Column: Band structure of the TTB driven by waveguide light with $Aa_0 = 0.3$. (a) AAA with MLT and parameters $(\theta, \omega) = (1.450^\circ, 3\gamma)$, and (b) the ABC stacking with MLT and $(\theta, \omega) = (1.157^\circ, 2\gamma)$. The solid lines are for the driven and the dash-dotted lines for the undriven case. Right Column: The density of states plots associated with the configurations on the left column rescaled by the maximum value $D_M(E)$ of the driven case.

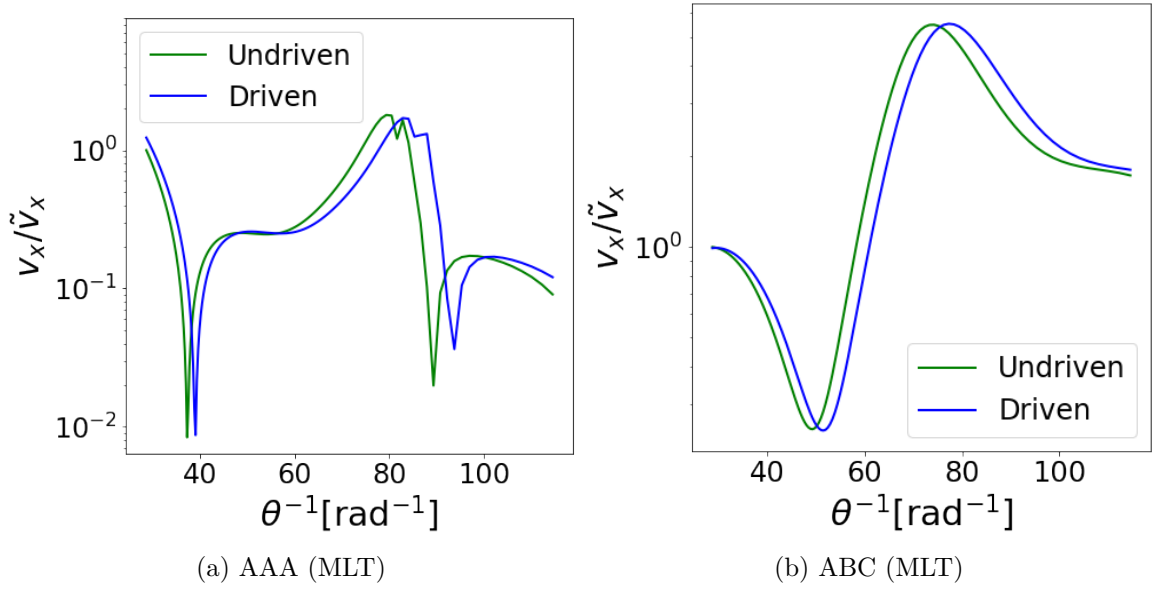


Figure 3.14: Plot of velocity as function of $1/\theta$ for the center bands near K1 in the twisted TTG system driven by waveguide light compared with the undriven case with $Aa_0 = 0.3$, and $\Omega = 3\gamma$. (a) Starting from AAA stacking middle layer twist (b) starting from ABC stacking middle layer twist. Here, \tilde{v}_x is the velocity at $\theta = 2.0^\circ$.

by simply replacing the interlayer couplings as follows

$$w_0 \rightarrow w_0 J_0(Aa_{AA}); \quad w_1 \rightarrow w_1 J_0(Aa_{AB}), \quad (3.24)$$

The interlayer hoppings are weakened by Bessel functions as it was also found in [145]. In twisted bilayer graphene it was found that the value of the magic angles was interlayer hopping dependent [214]. If we assume the same is true for twisted trilayer graphene then this explains the shift of magic angles that we observed in Fig.3.14.

Lastly, to see quantitatively how good this approximation is we have plotted both the exact quasi-energy spectrum as well as the one from this simple approximation. The result is shown in Fig. 3.15.

We find that the result even for a very large driving strength $Aa_0 = 0.8$ and relatively low frequencies $\omega = 1.5\gamma$ is almost perfect. For weaker driving strengths and higher frequencies it was even hard to see any discernible difference between the approximate and exact quasi-energies.

3.3 Haldane-Moiré Model in Driven Twisted Bilayer Graphene (TBLG)

3.3.1 Importance of Haldane Model

The quantum Hall effect is a phenomena where the Hall conductance become quantized in the corresponding physical system under applied external magnetic field [215]. This was the case until late 1980s when Duncan Haldane introduced his famous toy model (a.k.a. Haldane model) where he showed that similar features could occur without magnetic field and instead by introducing breaking time symmetry [216]. This effect is referred to by anomalous Hall effect or Chern insulator. While the

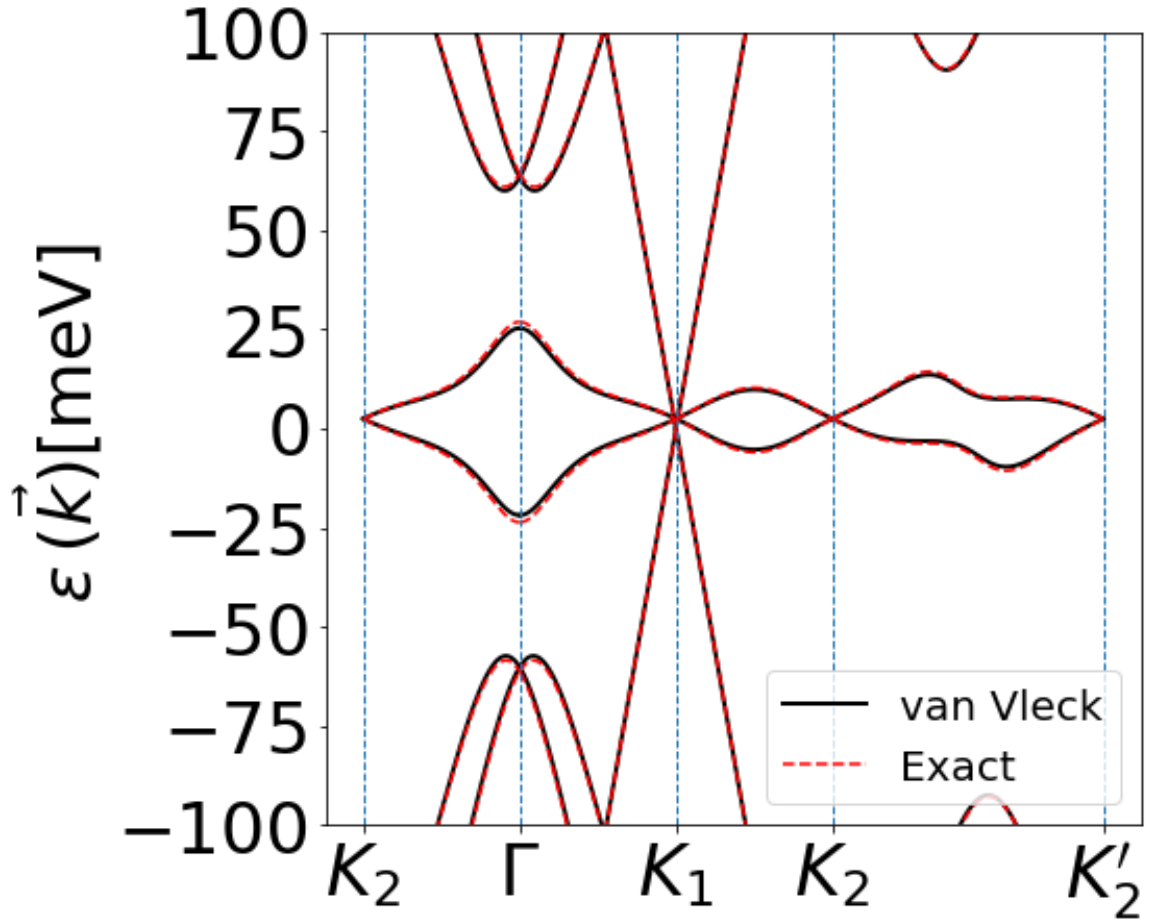


Figure 3.15: Comparison of the band structure for TTLG with ABA stacking and middle layer twisted driven by waveguide light with $\theta = 1.3^\circ$, $Aa_0 = 0.8$, and $\Omega = 1.5\gamma$. obtained via the quasi-energy operator Eq. 3.6 (dashed lines) versus the zeroth order van Vleck Hamiltonian H_0 (solid lines).

total Chern number of the two bands within this model vanishes, both bands still have nonzero Chern numbers with opposite values. One interesting thing about Haldane model is the existence of topologically protected edge states that can propagate between the valence and conduction bands. Although we don't have experimental realization of this model in real graphene, it was observed in other systems via experiments [217, 218]. Considering the importance of Haldane interactions for producing interesting topological properties, including it in twisted bilayer graphene (TBLG) is expected to yield new topological properties that were not observed in the normal TBLG [169].

In the next section, we will introduce the model within the context of twisted bilayer graphene and study the band structure. We will also consider the effect of light on this model on the band structure and identify the important features of this model in the following sections.

3.3.2 The Model

An important property of graphene tight-binding model is time-reversal symmetry which in momentum space reads

$$h^*(\vec{k}) = h(-\vec{k}) \quad (3.25)$$

where $h(\vec{k})$ is the single layer tight-binding Hamiltonian of graphene. In order to make graphene topological, Haldane suggested the inclusion of second nearest neighbor interaction that breaks time symmetry while preserving other symmetries of graphene. Haldane interaction is illustrated in Fig. 3.16.

This leads us to introduce the following equilibrium Hamiltonian that describes

the intralayer and interlayer interactions for our twisted bilayer graphene system,

$$H(\vec{x}, \vec{k}) = \begin{pmatrix} h(-\theta/2, \vec{k} - \vec{\kappa}_-) & T(\vec{x}) \\ T^\dagger(\vec{x}) & h(\theta/2, \vec{k} - \vec{\kappa}_+) \end{pmatrix}, \quad (3.26)$$

where $h(\theta, \vec{k})$ is the single layer Hamiltonian that contains the Haldane term which reads

$$h(\theta, \vec{k}) = \begin{pmatrix} M + 2t_2g(R(\theta)\vec{k}) & t_1f(R(\theta)\vec{k}) \\ t_1f^*(R(\theta)\vec{k}) & -M - 2t_2g(R(\theta)\vec{k}) \end{pmatrix}, \quad (3.27)$$

with

$$f(\vec{k}) = e^{-i(\lambda_+ + \lambda_-)} + e^{i\lambda_+} + e^{i\lambda_-}, \quad (3.28)$$

and,

$$g(\vec{k}) = -\sin(\alpha_+ + \alpha_-) + \sin\alpha_+ + \sin\alpha_-, \quad (3.29)$$

Here $\lambda_\pm = \pm \frac{a_0}{\sqrt{3}}k_x + \frac{a_0}{3}k_y \mp \frac{2\pi}{3}$, $\alpha_\pm = \frac{a_0}{\sqrt{3}}k_x \pm a_0k_y - \frac{2\pi}{3}$, $a_0 = 2.46\text{\AA}$ is the lattice constant for graphene, t_1 is the nearest neighbor hopping amplitude, M is the onsite energy (site A has M and site B has $-M$), and t_2 is the second-nearest neighbor hopping amplitude. The Haldane term is represented by the diagonal parts of Eq. 3.27. We should note that in our model we shifted the reciprocal lattice by $\kappa_\pm = \frac{k_\theta}{2}(-\sqrt{3}, \pm 1)$, where $k_\theta = (8\pi/3a_0)\sin(\theta/2)$. Finally, the interlayer tunneling matrix takes the form $T(\vec{x}) = \sum_{i=-1}^{i=+1} e^{-i\vec{b}_i \cdot \vec{x}} T_i$, where

$$T_i = w_0\mathbb{I} + w_1 \left[\cos\left(\frac{2n\pi}{3}\right) \sigma_1 + \sin\left(\frac{2n\pi}{3}\right) \sigma_2 \right] \quad (3.30)$$

with $b_{\pm 1} = \frac{k_\theta}{2}(\pm\sqrt{3}, 3)$, $\vec{b}_0 = (0, 0)$, and $w_{0,1}$ measure the strength of the interlayer hopping amplitude. As in illustration, we plot the band structure for our model in Fig.3.17.

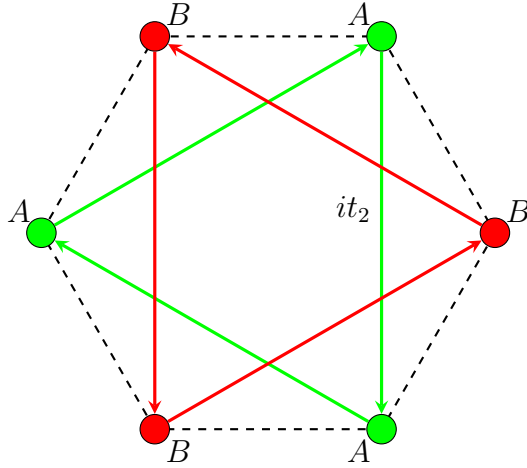


Figure 3.16: The second nearest neighbor Haldane interaction between the A and B sites in honeycomb lattice.

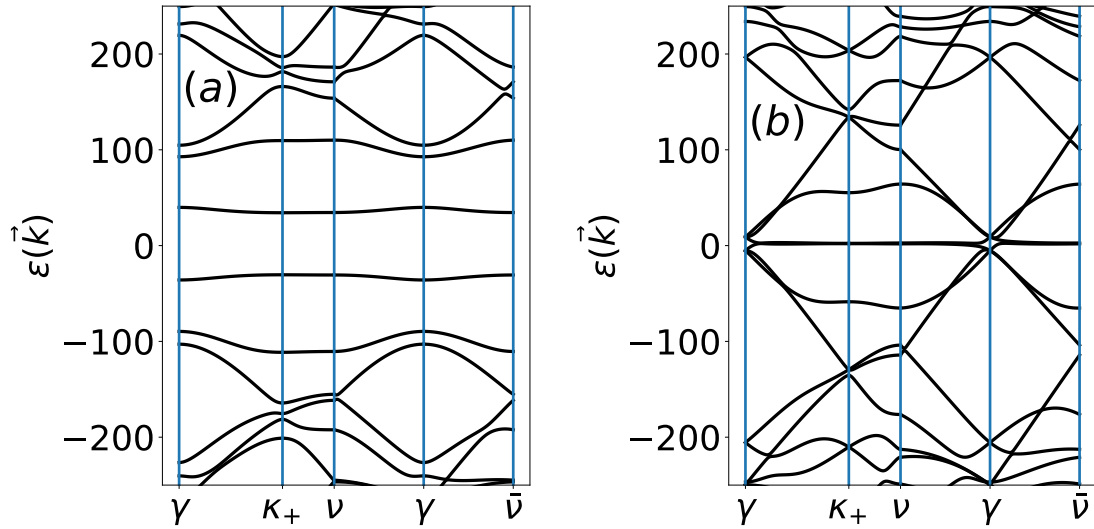


Figure 3.17: The equilibrium band structure of TBLG with Haldane interaction (a) $M = 9\sqrt{3}t_2/4$ and (b) $M = 3\sqrt{3}t_2$. Here we took $t_1 = 2360$, $t_2 = 0.05t_1$, $\theta = 1.05$, and $w_0 = w_1 = 110$

3.3.3 The Effect of Circularly Polarized Light

Following Section 3.2.3, we apply the minimal substitution to our Hamiltonian Eq. 3.26 and use the quasi-operator approach to obtain the quasi-energy. It's important to note that when doing the proper mathematical formalism, one needs to Fourier transform both $f(\vec{k})$ and $g(\vec{k})$ (Eqns. 3.28 & 3.29) and those results are shown in Appendix B. We plot the equilibrium band structure in Fig. 3.17. In this figure, we consider two values of the mass term $M = \{3\sqrt{3}t_2, 2.25\sqrt{3}t_2\}$ versus the two situations when the incident light is left handed (LH) and right handed (RH).

Two things we can take from Fig. 3.2.3. First, the mass term M when chosen arbitrarily, the physics of the system will be dominated by gaped bands that is expected from Haldane interaction, but choosing $M = 3\sqrt{3}t_2$ minimizes the effect of this term as it cancels the Haldane term at the γ point [169]. The second important finding is that the band structure is dependent of the handedness of light as shown in the same figure. This dependence on light polarization was never a feature of the regular TBLG [169], but was observed in TTLG [2]. This results in different phase diagrams as the situation in TTLG Fig.3.10, hence a similar thought out experiment as in Section 3.2.3.5 can be followed.

3.3.4 Waveguide Light

Following Sec. 3.2.4, we apply the maps $w_0 \rightarrow w_0 e^{-ia_{AA}A \cos(\omega t)}$ and $w_1 \rightarrow w_1 e^{-ia_{AB}A \cos(\omega t)}$ to Eq. 3.26. Here $a_{AA} = 0.36$ nm and $a_{AB} = 0.34$ nm are interlayer distances in AA and AB regions of the twisted materials [165]. The corresponding Fourier transformation of our Hamiltonian is obtained by the simple mapping of these hopping parameters as given in Appendix B. We plot the corresponding band structure in Fig. 3.19. Unlike circularly polarized light, waveguide light (WGL) does not cause band gap opening, a

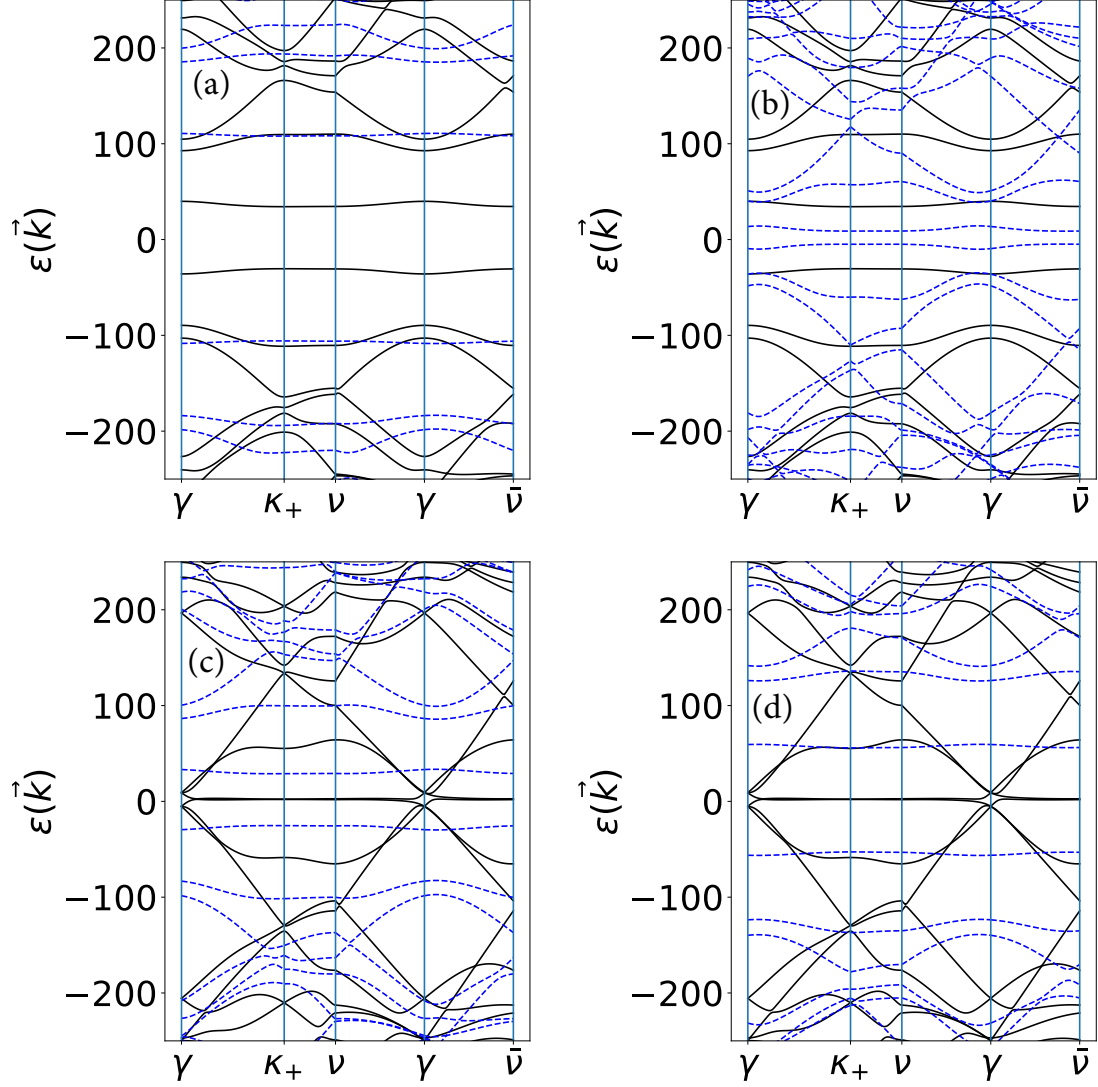


Figure 3.18: The band structure of TBLG with Haldane interaction showing the static case (solid black lines) versus the case with circularly polarized light (dashed blue lines). (a) $M = 9\sqrt{3}t_2/4$ with RH light, (b) $M = 9\sqrt{3}t_2/4$ with LH light, (c) $M = 3\sqrt{3}t_2$ for RH light and (d) $M = 3\sqrt{3}t_2$ with LH light. Here we took $Aa_0 = 0.4$, $\omega = 2t_1$ and the other values as in Fig. 3.2.

feature that is shared with other systems [2,169]. However, the WGL can be basically used to shift the magic angle of the system as observed in TTLG Fig. 3.14.

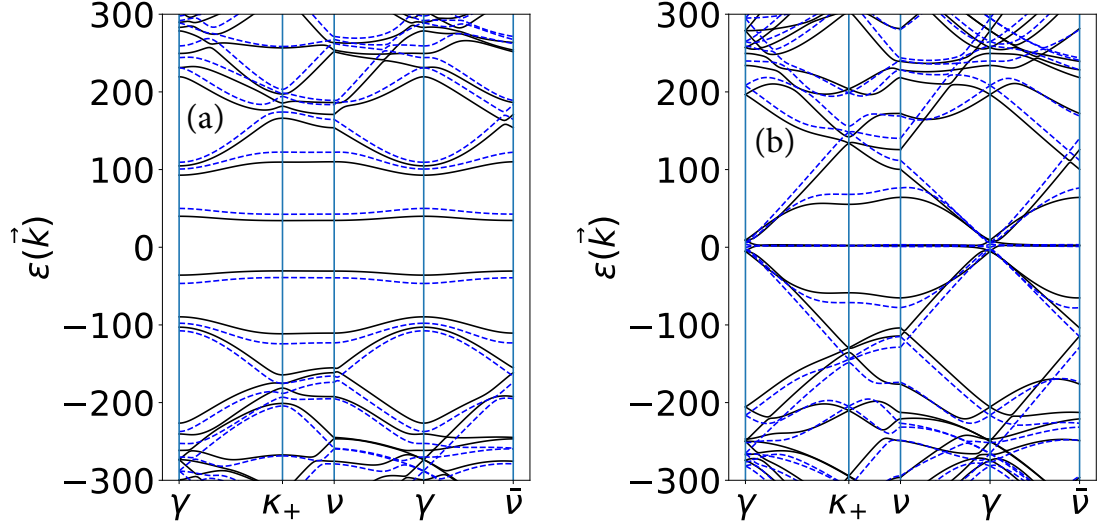


Figure 3.19: The band structure of TBLG with Haldane interaction for the static case (solid black lines) versus that with waveguide light (dashed blue lines) (a) $M = 9\sqrt{3}t_2/4$ and (b) $M = 3\sqrt{3}t_2$. Here we took $t_1 = 2360$, $t_2 = 0.05t_1$, $\theta = 1.05$, $w_0 = w_1 = 110$, $Aa_0 = 0.4$, and $\omega = 1.5t_1$.

3.4 Summary

In this chapter, we reviewed Floquet theory as an approach to study periodic time-dependent Hamiltonians with the focus on moiré materials. In Sec. 3.2, we have studied four different stacking configurations of twisted trilayer graphene (TTLG). First we reviewed the equilibrium properties and then went on to study various non-equilibrium scenarios. In the presence of a circularly polarized light, we found that we were able to flatten the two middle bands compared to the equilibrium case which could open the door to experiments with strongly correlated non-equilibrium phases. Even more exciting, is the fact that this type of light causes gap openings, which then allowed us to study the topological properties of the TTLG configurations that

are characterized by single-band Chern numbers. Here, we focused on the six middle bands and generated topological phase diagrams for a range of different values of the driving strength and the twist angle. These diagrams revealed that TTLG has a rich topological structure. Moreover, we found that the topological structure of ABC stacked TTLG with a top-layer twist is sensitive to the handedness of circularly polarized light. This is in stark contrast with the other three configurations that we have studied.

The fact that top twisted ABC stacked bilayer graphene has different topological phase diagrams depending on the the polarization of circularly polarized light led us to propose an experiment where this difference in topologies could be captured via optical conductivity measurements. Here, one takes two sources of circularly polarized light with different handedness and lets them shine on TTLG such that the two illuminated regions intersect. This creates three distinct regions of different topology, and thus edge states are expected on the boundaries between these regions and their boundary with the undriven regions. The different topological properties are expected to be measurable in optical conductivity measurements.

In addition, to circularly polarized light we also studied the effects that longitudinally polarized light, coming from a waveguide, has on the band structure. We found that the presence of this light source can make the central bands less dispersive without the introduction of band gap openings like in the case of circularly polarized light. This means that effectively we were able to shift the magic angle where flat-bands appear without introducing additional side-effects that complicate the Hamiltonian description. This observation might be useful for the realization of strongly correlated phases in TTLG that closely resemble the equilibrium case at a different twist angle.

Our second system was the twisted bilayer graphene (TBLG) with Haldane interaction driven by two different light sources. Such interaction breaks time symmetry

and results in rich topological features. We limited ourselves to band structure calculations using Floquet theory for the equilibrium and non-equilibrium situations as shown in Figures 3.17, 3.2.3 & 3.19. An interesting sign of rich topological phase diagram is the handedness dependence of band structure on the incident light as shown in Fig. 3.18. This feature was not observed on normal TBLG but was observed in TTLG system. One could generate the topological phase diagrams for our TBLG system by following the same steps mentioned in Sec. 3.2.3.4.

Chapter 4

Conclusions and future Work

In the first part of this thesis, we have introduced a novel algorithm that is able to systematically study many-body perturbative expansions on the imaginary and real frequency axes for a general two-body interaction Hamiltonian. For discrete systems such as molecular chemistry problems, our results are exact at any perturbation order regardless of the parameters and temperatures used. On the other hand, for lattice models the accuracy is directly connected to the stochastic sampling of momenta that is used in our calculations and can always be improved by increasing the sample size, hence is referred to semi-exact results. Note that this is very different from the usual diagrammatic Monte Carlo methods because we perform exact evaluation of the Matsubara summations via the algorithmic Matsubara integration (AMI) tool [88, 152, 219].

An interesting part of our symDET algorithm is the ability to study multiband systems which makes our method applicable to a larger class of Hamiltonians that are used to model wide range of real physical systems that are relevant to both physicists and chemists [1, 81, 220–226]. Nonetheless, our symDET method is equivalent to a single shot n th order Green's function method GF_n , exceeding what is currently

available [227].

While we focused solely on fermionic systems, we would like to stress that our algorithm can be easily used to study bosonic systems as well as mixed systems (i.e. fermionic and bosonic mixture). This can be essentially done in two steps. First, one needs to alter the contraction generator so that we generate the proper Wick contractions for bosons. Once this step is done, the remaining part is to modify the structure of Matsubara summations to allow us to use the AMI since its current form evaluates fermionic summations. This can be done as follows. In the perturbative expansions associated with bosons we end up with a similar Matsubara summation as in the Fermionic case

$$J_n = \frac{1}{\beta^n} \sum_{\{\omega_n\}} \prod_{i=1}^N d_i(\varepsilon_i, \vec{\alpha}_i) \quad (4.1)$$

where

$$d_i(\varepsilon_i, \vec{\alpha}_i) = \frac{1}{i\vec{\alpha}_i \cdot \vec{\nu}_\nu - \varepsilon_i} \quad (4.2)$$

is the imaginary-time bosonic free propagator in the frequency space with $\vec{\nu}_\nu = \{\nu_1, \nu_2, \dots, \nu_n, \nu_{\text{ex}}\}$ and the Matsubara frequency is $\nu_\ell = 2n\pi/\beta$. To make use of the AMI, we can express ν_ℓ in terms of the fermionic frequency $\nu_n = \Omega_n - \pi/\beta$. Consequently, the bosonic propagator is expressed as a fermionic propagator with complex energy,

$$d_i(\varepsilon_i, \vec{\alpha}_i) := g_i(\tilde{\varepsilon}_i, \vec{\alpha}_i) = \frac{1}{i\vec{\alpha}_i \cdot \vec{\Omega} - \tilde{\varepsilon}_i} \quad (4.3)$$

where $\tilde{\varepsilon}_i = \varepsilon_i + i\frac{\pi}{\beta} \sum_{j=1}^{j=n+1} \alpha_j$. Consequently, the bosonic sum in Eq. 4.1 takes the exact form of the fermionic summation in Eq. 2.31 and the AMI can now be applied easily. The construction of the frequency labels and the complex energies is done with the help of the symbolic Fourier transformation. In the case with mixed systems, one can follow the same steps and do the transformation of the bosonic propagators as explained above. A direct application of this extension would be the Bose-Hubbard

model [228–231].

Another possible application of the bosonic version of symDET could be the quantum rare-earth pyrochlores that are characterized by an effective pseudo-spin 1/2 Hamiltonian [16, 232–235]. One can simply apply exact Holstein-Primakoff for spin one-half operators that were introduced in Ref. [236] which results in an effective Hamiltonian with an extra sextic term that can be carefully included via a proper Wick contraction generator while the rest of the steps are pretty much the same.

So far, we have seen that the elements of our algorithm can be extended to study a much larger class of problems that have direct real applications. This is pretty exciting and investigating these different models would help develop deeper insights into many-body phenomena.

The second part of this thesis focused on driven twisted graphene systems and how to study their properties via Floquet theory. Twisted graphene systems are characterized by magic angles whereby the emergence of flat bands occur in the band structure. Those flat bands are a signature of strong electron-electron correlations and give rise to interesting many-body phases that make those systems so exciting. Such states could be, but not limited to, superconductivity, correlated insulators, and ferromagnetism.

As a first application, we considered twisted trilayer graphene (TTLG) driven by two types of light, circularly polarized light and waveguide light. We applied Floquet theory to study the non-equilibrium cases and obtained the associated band structures as well as the topological phase diagrams. An interesting finding was the case of ABC stacked TTLG that was shown to depend on the handedness of circularly polarized light which lead us to propose an experiment where one can verify these findings via optical conductivity measurements as discussed in Sec.3.2. The TTLG system also has rich topological phase diagrams for the different stacking configurations.

In the second example we studied the band structure of twisted bilayer graphene (TBLG) with Haldane second nearest neighbor interactions. This was motivated by the rich topological properties that emerge from the Haldane term which breaks time-reversal symmetry in the effective Hamiltonian. Similar to TTLG, we considered the two scenarios with circularly polarized light and light coming from waveguide and we generated the band structure for each case using the quasi-operator formalism. An interesting feature of the band structure in the case of circularly polarized light is the dependence of the quasi-energies on the handedness of the incident light as illustrated in Fig. 3.18. Based on our results, we expect this model to have richer topological properties that are otherwise not common in the normal TBLG without the Haldane term.

An interesting question one may ask: Is it possible to use symDET to study twisted graphene systems, or generally twisted 2D systems? To answer this question, we consider two different situations. If the twisted system is at equilibrium, then the straight answer is yes. Different Hubbard-like models were introduced to model twisted 2D systems [164, 237–239]. We should note that those models are general multiband and hence make a perfect fit for our symDET algorithm. On the other hand, the situation with periodically driven twisted systems is a little difficult but is not impossible. One needs to find the effective Floquet Hamiltonian that brings the system to an equivalent (quasi) equilibrium model which can then be analyzed via symDET. Finding the so-called Floquet Gibbs states is the central part of constructing such Hamiltonian, which can be engineered given certain boundary conditions [240–242]. Considering the exotic properties of twisted systems, it would be interesting to pursue this task in the future.

Appendix A

Steps of the SFT

A.1 Sorting Wick's contractions

An important step to perform the symbolic Fourier transformation is to sort the given Wick contraction that corresponds to a connected diagram as follows. First, let's represent the given contraction as $\mathcal{C} = [\vec{P}, s]$ where $\vec{P} = (p_1, p_2, \dots, p_{2n+1})$ is a vector of pairs representing each Fermion line with $p_j = (\tau_0^j, \tau_1^j)$, and s is the sign of the contraction. In the language of graph theory, \vec{P} contains the edges of the graph. To check if the diagram is connected or not, one can use the Depth First Search (DFS) which requires \vec{P} as an input. If \mathcal{C} is connected, then we introduce three vectors of pairs \vec{A} , \vec{B} , and \vec{C} where we store the pairs from \vec{P} into these three vectors based on the following convention. The pairs representing connection with external vertices are stored in \vec{B} and the pairs which represent loops, i.e. tadpole/clamshell structures, are stored in \vec{C} .

The next step is to reduce the number of pairs in \vec{A} to $n - 1$ which is adopted from basic graph theory fact that a given connected graph with n vertices has $n - 1$ edges connecting all the vertices together (plus the extra edges). This can be done

recursively using the DFS by removing one pair at a time from \vec{A} and applying the DFS to check if the remaining pairs keeps all the vertices connected or not. If the removal of a given pair doesn't affect the connectedness, then the pair should be added to \vec{C} , otherwise it should be put back into \vec{A} and then move to the next pair in \vec{A} and do the same steps until the number of pairs is $n - 1$. At this moment, the numbers of pairs in \vec{C} is n , with the total number of pairs in all the three vectors is $2n + 1$ as expected. The contraction \mathcal{C} will have the form

$$\mathcal{C} = [\vec{A}, \vec{B}, \vec{C}, s] \tag{A.1}$$

A.2 Array representation of the non-interacting Green's function

Let us assume that the fermionic line connecting two vertices τ_i and τ_j in an n^{th} order Feynman diagram is represented by a Green's function of the form $g(\eta; \tau_i - \tau_j)$ where η is a set of quantum labels attached to the corresponding Green's function. We introduce the following useful array representation of $g(\eta; \tau_i - \tau_j)$

$$g(\eta; \tau_i - \tau_j) = [V_j(1 - \delta_{ij}), \eta], \tag{A.2}$$

where $V_j \in \mathbb{R}^n$ is an n -dimensional vector defined in the following way:

- If the fermionic line is connecting two different internal vertices, then V_j has +1 at the i^{th} row, -1 at the j^{th} row, and zeros elsewhere.
- V_j is the n -dimensional zero vector if $\tau_i = \tau_j$. This is guaranteed by δ_{ij} in the equation above.

- The two external fermionic lines are represented with n -dimensional vector with only one nonzero entry ± 1 . Basically, when τ_j external time and τ_i is internal time then V_j has entry of $+1$ at the i^{th} row and zeros elsewhere. On the other hand, if τ_i is the external time, and τ_j is an internal time then V_j is an entry -1 at the i^{th} row and zeros elsewhere.

Following this notation, we can represent a Wick contraction (A.1) as

$$\mathcal{C} = [M, s] \tag{A.3}$$

where $M = (A|B|C)$ is an $n \times 2n + 1$ matrix obtained by mapping the pairs in $\{\vec{A}, \vec{B}, \vec{C}\}$ into column vectors using the convention explained above. Basically, the $n - 1$ pairs in \vec{A} form an $n \times (n - 1)$ matrix A , the 2 pairs in \vec{B} form an $n \times 2$ matrix B , and the n pairs in \vec{C} form an $n \times n$ matrix C . In the next section, we will use this result to obtain the Fourier transformation of the contraction \mathcal{C} .

A.3 The Symbolic Fourier Transform (SFT)

Let us assume that the fermionic lines whose vectors stored in A has the dependent Matsubara frequencies $\{\omega_1, \omega_2, \dots, \omega_{n-1}\}$, the ones stored in B has the external frequency ω_{ex} , and the vectors stored in C has the independent Matsubara frequencies $\{\Omega_1, \Omega_2, \dots, \Omega_n\}$. Defining $\vec{\Omega} = (\omega_1, \omega_2, \dots, \omega_{n-1}, \omega_{\text{ex}}, \omega_{\text{ex}}, \Omega_1, \Omega_2, \dots, \Omega_n)^t$, then one can show that the equation that connects all the frequencies together is

$$M\vec{\Omega} = \vec{0}. \tag{A.4}$$

The above equation is thought of as the set of delta functions which act to enforce conservation laws at each vertex so long as Eq. A.4 is satisfied. Our task is to represent

the dependent frequencies in terms of the other frequencies which is obtained using the above equation, giving

$$\begin{pmatrix} \omega_1 \\ \omega_2 \\ \omega_3 \\ \vdots \\ \omega_{n-1} \end{pmatrix} = \alpha \omega_{\text{ex}} + \beta \begin{pmatrix} \Omega_1 \\ \Omega_2 \\ \vdots \\ \Omega_n \end{pmatrix}, \quad (\text{A.5})$$

where

$$\alpha = -J^{-1} A^T B \begin{pmatrix} 1 \\ 1 \end{pmatrix}, \beta = -J^{-1} A^T C \quad (\text{A.6})$$

with $J = A^T A$ is an $n - 1 \times n - 1$ matrix. The above Eq. A.5 gives a unique representation of the frequency labels which satisfies the conservation laws at all internal vertices. Using this notation, a Green's function with a dependent frequency ω_j , i.e. $g(\eta; \omega_j)$, will be represented as

$$g_k(\eta_k; \omega_j) = \frac{1}{i\beta_j \cdot \vec{\Omega}_{\text{ind}} + i\alpha_j \omega_{\text{ex}} - \varepsilon_{\eta_k}} \quad (\text{A.7})$$

where β_j is the j th row in β , α_j is the j th entry in α , and $\vec{\Omega}_{\text{ind}} = (\Omega_1, \Omega_2, \dots, \Omega_n)^t$. Consequently, we introduce the Fourier transformation of the Wick contraction (A.1) as

$$\mathcal{F}[\mathcal{C}] := [g_A, g_B, g_C, s], \quad (\text{A.8})$$

where

$$g_A = [g_1(\eta_1; \omega_1), g_2(\eta_2; \omega_2), \dots, g_{n-1}(\eta_{n-1}; \omega_{n-1})] \quad (\text{A.9})$$

$$g_B = [g_n(\eta_n; \omega_{\text{ex}}), g_2(\eta_{n+1}; \omega_{\text{ex}})] \quad (\text{A.10})$$

and

$$g_C = [g_{n+2}(\eta_{n+2}; \Omega_1), \dots, g_{2n+1}(\eta_{2n+1}; \Omega_n)] \quad (\text{A.11})$$

where the Fourier transformed Green's functions in $\{g_B, g_C\}$ takes the following simple form

$$g_\ell(\eta_\ell; \omega) = \frac{1}{i\omega - \varepsilon_{\eta_\ell}} \quad (\text{A.12})$$

Finally, the AMI frequency input will simply be

$$\omega_{\text{AMI}} = \left(\begin{array}{c|c} \beta & \alpha \\ \hline I_n & 0 \end{array} \right) \quad (\text{A.13})$$

where I_n is an $n \times n$ identity matrix and 0 here represents an n -dimensional zero vector.

Theorem A.3.1. *Let M be an $n \times (2n + 1)$ matrix representing one particular contraction belonging to specific topology \mathcal{T} with M satisfying (A.4), then the frequency matrix ω_{AMI} (A.13) is unique for all contractions belonging to the same \mathcal{T} .*

Proof. We know that there are $2^n n!$ contractions per topology \mathcal{T} at n^{th} order. The factor 2^n coming from inverting the interaction line at each vertex which essential keeps M invariant. The factorial part coming from relabelling the vertices which is equivalent to re-arranging the rows in M . Let P be an $n \times n$ orthogonal matrix that permutes the rows in M bringing it to a new matrix $\tilde{M} := (\tilde{A}|\tilde{B}|\tilde{C}) = PM$. This is equivalent to setting $\tilde{A} = PA$, $\tilde{B} = PB$, and $\tilde{C} = PC$. Clearly, $\tilde{J} = \tilde{A}^T \tilde{A} = J$, $\tilde{A}^T \tilde{B} = A^T B$ and $\tilde{A}^T \tilde{C} = A^T C$. Thus, $\tilde{\alpha} = \alpha$ and $\tilde{\beta} = \beta$. \square

The frequency labels can be not unique for a given diagram due to the several possible options of our choice of A and equivalently C . In graph theory language, this has to do with the existence of several *directed trees* that are consisting of $n - 1$

edges connecting the n vertices. Regardless of this starting choice, the above theorem implies that all of the sibling diagrams in the same topology will always have the same frequency labels once the labels are fixed for one diagram (the AMI input matrix Eq. A.13).

Appendix B

Fourier Transform of Haldane-Moiré Bilayer Graphene Hamiltonian

The Fourier transform of a function $W(\vec{k}, t)$ is defined as

$$W_n(\vec{k}) = T^{-1} \int_0^T dt e^{-in\omega t} W(\vec{k}, t) \quad (\text{B.1})$$

where T is the period and n is an integer (Fourier mode). Applying this definition to Eqns. 3.28 & 3.29, we obtain the following Fourier transforms

$$f_n(\vec{k}) = e^{in\theta} \left\{ e^{-i\frac{2a_0}{3}k_y} + 2e^{i\frac{a_0}{3}k_y} e^{-in\pi} \sin \left[\frac{a_0}{\sqrt{3}}k_x - \frac{\pi}{6} + \frac{n\pi}{3} \right] \right\} J_n \left(\frac{2Aa_0}{3} \right) \quad (\text{B.2})$$

and

$$g_n(\vec{k}) = e^{in\theta} \left\{ \sin \left[-\frac{2a_0k_x}{\sqrt{3}} + \frac{4\pi}{3} + \frac{n\pi}{2} \right] + e^{-in\pi} e^{ia_0k_y} \sin \left[\frac{a_0}{\sqrt{3}}k_x - \frac{2\pi}{3} + \frac{n\pi}{6} \right] \right\}$$

$$+ e^{-ia_0k_y} \sin \left[\frac{a_0}{\sqrt{3}}k_x - \frac{2\pi}{3} - \frac{n\pi}{6} \right] \Big\} J_n \left(\frac{2Aa_0}{\sqrt{3}} \right) \quad (\text{B.3})$$

where $J_n(x)$ is Bessel function of second kind. Those functions are very important for the circularly polarized light case. However, for the waveguide light situation, the Fourier transform of our Haldane TBLG Hamiltonian is obtained by the simple replacement

$$w_0 \rightarrow w_0 J_0(Aa_{AA}); \quad w_1 \rightarrow w_1 J_0(Aa_{AB}), \quad (\text{B.4})$$

Bibliography

- [1] J. Li, M. Wallerberger, and E. Gull. Diagrammatic Monte Carlo method for impurity models with general interactions and hybridizations. *Phys. Rev. Res.*, 2:033211, doi:10.1103/PhysRevResearch.2.033211.
- [2] I. A. Assi, J. P. F. LeBlanc, M. Rodriguez-Vega, H. Bahlouli, and M. Vogl. Floquet engineering and nonequilibrium topological maps in twisted trilayer graphene. *Phys. Rev. B*, 104:195429, doi:10.1103/PhysRevB.104.195429.
- [3] J. Bardeen, L. N. Cooper, and J. R. Schrieffer. Theory of Superconductivity. *Phys. Rev.*, 108:1175–1204, doi:10.1103/PhysRev.108.1175.
- [4] N. W. Ashcroft. Metallic Hydrogen: A High-Temperature Superconductor? *Phys. Rev. Lett.*, 21:1748–1749, doi:10.1103/PhysRevLett.21.1748.
- [5] J. M. McMahon, M. A. Morales, C. Pierleoni, and D. M. Ceperley. The properties of hydrogen and helium under extreme conditions. *Rev. Mod. Phys.*, 84:1607–1653, doi:10.1103/RevModPhys.84.1607.
- [6] F. Peng, Y. Sun, C. J. Pickard, R. J. Needs, Q. Wu, and Y. Ma. Hydrogen Clathrate Structures in Rare Earth Hydrides at High Pressures: Possible Route to Room-Temperature Superconductivity. *Phys. Rev. Lett.*, 119:107001, doi:10.1103/PhysRevLett.119.107001.

- [7] A. P. Drozdov, P. P. Kong, V. S. Minkov, S. P. Besedin, M. A. Kuzovnikov, S. Mozaffari, L. Balicas, F. F. Balakirev, D. E. Graf, V. B. Prakapenka, E. Greenberg, D. A. Knyazev, M. Tkacz, and M. I. Eremets. Superconductivity at 250 K in lanthanum hydride under high pressures. *Nature*, 569(7757):528–531, doi:10.1038/s41586-019-1201-8.
- [8] M. Somayazulu, M. Ahart, A. K. Mishra, Z. M. Geballe, M. Baldini, Y. Meng, V. V. Struzhkin, and R. J. Hemley. Evidence for Superconductivity above 260 K in Lanthanum Superhydride at Megabar Pressures. *Phys. Rev. Lett.*, 122:027001, doi:10.1103/PhysRevLett.122.027001.
- [9] B. Bireckoven and J. Wittig. A diamond anvil cell for the investigation of superconductivity under pressures of up to 50 GPa: Pb as a low temperature manometer. *Journal of Physics E: Scientific Instruments*, 21(9):841, doi:10.1088/0022-3735/21/9/004.
- [10] A. Lazicki, C.-S. Yoo, H. Cynn, W. J. Evans, W. E. Pickett, J. Olamit, K. Liu, and Y. Ohishi. Search for superconductivity in LiBC at high pressure: Diamond anvil cell experiments and first-principles calculations. *Phys. Rev. B*, 75:054507, doi:10.1103/PhysRevB.75.054507.
- [11] Y. A. Timofeev, V. V. Struzhkin, R. J. Hemley, H.-k. Mao, and E. A. Gregoryanz. Improved techniques for measurement of superconductivity in diamond anvil cells by magnetic susceptibility. *Review of Scientific Instruments*, 73(2):371–377, doi:10.1063/1.1431257.
- [12] R. Sibille, E. Lhotel, V. Pomjakushin, C. Baines, T. Fennell, and M. Kenzelmann. Candidate Quantum Spin Liquid in the Ce^{3+} Pyrochlore Stannate $\text{Ce}_2\text{Sn}_2\text{O}_7$. *Phys. Rev. Lett.*, 115:097202, doi:10.1103/PhysRevLett.115.097202.

- [13] L. Savary and L. Balents. Disorder-Induced Quantum Spin Liquid in Spin Ice Pyrochlores. *Phys. Rev. Lett.*, 118:087203, doi:10.1103/PhysRevLett.118.087203.
- [14] S. Sanyal, K. Dhochak, and S. Bhattacharjee. Interplay of uniform $U(1)$ quantum spin liquid and magnetic phases in rare-earth pyrochlore magnets: A fermionic parton approach. *Phys. Rev. B*, 99:134425, doi:10.1103/PhysRevB.99.134425.
- [15] A. G. D. Maestro and M. J. P. Gingras. Quantum spin fluctuations in the dipolar Heisenberg-like rare earth pyrochlores. *Journal of Physics: Condensed Matter*, 16(20):3339, doi:10.1088/0953-8984/16/20/005.
- [16] Y.-P. Huang, G. Chen, and M. Hermele. Quantum Spin Ices and Topological Phases from Dipolar-Octupolar Doublets on the Pyrochlore Lattice. *Phys. Rev. Lett.*, 112:167203, doi:10.1103/PhysRevLett.112.167203.
- [17] J. P. Eisenstein and A. H. MacDonald. Bose–Einstein condensation of excitons in bilayer electron systems. *Nature*, 432(7018):691–694, doi:10.1038/nature03081.
- [18] H. Min, R. Bistritzer, J.-J. Su, and A. H. MacDonald. Room-temperature superfluidity in graphene bilayers. *Phys. Rev. B*, 78:121401, doi:10.1103/PhysRevB.78.121401.
- [19] K. Seo, V. N. Kotov, and B. Uchoa. Ferromagnetic Mott state in Twisted Graphene Bilayers at the Magic Angle. *Phys. Rev. Lett.*, 122:246402, doi:10.1103/PhysRevLett.122.246402.
- [20] K. Tamura and H. Katsura. Ferromagnetism in the $SU(n)$ Hubbard model with a nearly flat band. *Phys. Rev. B*, 100:214423, doi:10.1103/PhysRevB.100.214423.

- [21] H. Komatsu, Y. Nonomura, and M. Nishino. Phase diagram of the dipolar Ising ferromagnet on a kagome lattice. *Phys. Rev. B*, 106:014402, doi:10.1103/PhysRevB.106.014402.
- [22] E. H. Lieb and F. Y. Wu. Absence of Mott Transition in an Exact Solution of the Short-Range, One-Band Model in One Dimension. *Phys. Rev. Lett.*, 21:192–192, doi:10.1103/PhysRevLett.21.192.2.
- [23] N. Kawakami. Asymptotic Bethe ansatz: Application to the one-dimensional t-J model with long-range exchange and transfer. *Phys. Rev. B*, 45:7525–7528, doi:10.1103/PhysRevB.45.7525.
- [24] P. Scholl and R. Orús. Kitaev honeycomb tensor networks: Exact unitary circuits and applications. *Phys. Rev. B*, 95:045112, doi:10.1103/PhysRevB.95.045112.
- [25] R. K. Pathria and P. D. Beale. Phase Transitions: Criticality, Universality, and Scaling. In *Statistical Mechanics*, pages 401–469. Elsevier, 2011.
- [26] S. Galam. Self-consistency and symmetry in d dimensions. *Phys. Rev. B*, 54:15991–15996, doi:10.1103/PhysRevB.54.15991.
- [27] V. Janiš. A new construction of thermodynamic mean-field theories of itinerant fermions: application to the Falicov-Kimball model. *Z. Physik B - Condensed Matter*, 83(2):227–235, June 1991.
- [28] A. Georges and G. Kotliar. Hubbard model in infinite dimensions. *Physical Review B*, 45(12):6479–6483, 1992.

- [29] A. Georges, G. Kotliar, W. Krauth, and M. J. Rozenberg. Dynamical mean-field theory of strongly correlated fermion systems and the limit of infinite dimensions. *Rev. Mod. Phys.*, 68:13–125, doi:10.1103/RevModPhys.68.13.
- [30] G. Kotliar and D. Vollhardt. Strongly correlated materials: Insights from dynamical mean-field theory. *Phys. Today*, 57(3):53–59, March 2004.
- [31] M. H. Hettler, A. N. Tahvildar-Zadeh, M. Jarrell, T. Pruschke, and H. R. Krishnamurthy. Nonlocal dynamical correlations of strongly interacting electron systems. *Phys. Rev. B*, 58:R7475–R7479, doi:10.1103/PhysRevB.58.R7475.
- [32] M. H. Hettler, M. Mukherjee, M. Jarrell, and H. R. Krishnamurthy. Dynamical cluster approximation: Nonlocal dynamics of correlated electron systems. *Phys. Rev. B*, 61:12739–12756, doi:10.1103/PhysRevB.61.12739.
- [33] T. Maier, M. Jarrell, T. Pruschke, and M. H. Hettler. Quantum cluster theories. *Rev. Mod. Phys.*, 77:1027–1080, doi:10.1103/RevModPhys.77.1027.
- [34] H. Q. Lin. Exact diagonalization of quantum-spin models. *Phys. Rev. B*, 42:6561–6567, doi:10.1103/PhysRevB.42.6561.
- [35] D. J. Luitz, N. Laflorencie, and F. Alet. Extended slow dynamical regime close to the many-body localization transition. *Phys. Rev. B*, 93:060201, doi:10.1103/PhysRevB.93.060201.
- [36] C. Kollath, A. M. Läuchli, and E. Altman. Quench Dynamics and Nonequilibrium Phase Diagram of the Bose-Hubbard Model. *Phys. Rev. Lett.*, 98:180601, doi:10.1103/PhysRevLett.98.180601.
- [37] C. WEI and S. H. Curnoe. Exact diagonalization for a 16-site spin-1/2 pyrochlore cluster. *Journal of Physics: Condensed Matter*, 2023.

- [38] S. R. White. Density matrix formulation for quantum renormalization groups. *Phys. Rev. Lett.*, 69:2863–2866, doi:10.1103/PhysRevLett.69.2863.
- [39] S. R. White. Density-matrix algorithms for quantum renormalization groups. *Phys. Rev. B*, 48:10345–10356, doi:10.1103/PhysRevB.48.10345.
- [40] E. M. Stoudenmire and S. R. White. Real-space parallel density matrix renormalization group. *Phys. Rev. B*, 87:155137, doi:10.1103/PhysRevB.87.155137.
- [41] T. Serwatka and P.-N. Roy. Ground state of asymmetric tops with DMRG: Water in one dimension. *The Journal of Chemical Physics*, 156(4), doi:10.1063/5.0078770.
- [42] E. M. Stoudenmire, L. O. Wagner, S. R. White, and K. Burke. One-Dimensional Continuum Electronic Structure with the Density-Matrix Renormalization Group and Its Implications for Density-Functional Theory. *Phys. Rev. Lett.*, 109:056402, doi:10.1103/PhysRevLett.109.056402.
- [43] J. Lee, S. Sachdev, and S. R. White. Electronic quasiparticles in the quantum dimer model: Density matrix renormalization group results. *Phys. Rev. B*, 94:115112, doi:10.1103/PhysRevB.94.115112.
- [44] S. R. White and A. L. Chernyshev. Néel Order in Square and Triangular Lattice Heisenberg Models. *Phys. Rev. Lett.*, 99:127004, doi:10.1103/PhysRevLett.99.127004.
- [45] M. Q. Weng, D. N. Sheng, Z. Y. Weng, and R. J. Bursill. Spin-liquid phase in an anisotropic triangular-lattice Heisenberg model: Exact diagonalization and density-matrix renormalization group calculations. *Phys. Rev. B*, 74:012407, doi:10.1103/PhysRevB.74.012407.

- [46] H. C. Jiang, Z. Y. Weng, and D. N. Sheng. Density Matrix Renormalization Group Numerical Study of the Kagome Antiferromagnet. *Phys. Rev. Lett.*, 101:117203, doi:10.1103/PhysRevLett.101.117203.
- [47] E. Stoudenmire and S. R. White. Studying Two-Dimensional Systems with the Density Matrix Renormalization Group. *Annual Review of Condensed Matter Physics*, 3(1):111–128, doi:10.1146/annurev-conmatphys-020911-125018.
- [48] F. Verstraete, M. M. Wolf, D. Perez-Garcia, and J. I. Cirac. Criticality, the Area Law, and the Computational Power of Projected Entangled Pair States. *Phys. Rev. Lett.*, 96:220601, doi:10.1103/PhysRevLett.96.220601.
- [49] M. Scheb and R. M. Noack. Finite projected entangled pair states for the Hubbard model. *Phys. Rev. B*, 107:165112, doi:10.1103/PhysRevB.107.165112.
- [50] Q. Yang, X.-Y. Zhang, H.-J. Liao, H.-H. Tu, and L. Wang. Projected d -wave superconducting state: A fermionic projected entangled pair state study. *Phys. Rev. B*, 107:125128, doi:10.1103/PhysRevB.107.125128.
- [51] V. Murg, F. Verstraete, and J. I. Cirac. Variational study of hard-core bosons in a two-dimensional optical lattice using projected entangled pair states. *Phys. Rev. A*, 75:033605, doi:10.1103/PhysRevA.75.033605.
- [52] V. Murg, F. Verstraete, and J. I. Cirac. Exploring frustrated spin systems using projected entangled pair states. *Phys. Rev. B*, 79:195119, doi:10.1103/PhysRevB.79.195119.
- [53] M. Lubasch, J. I. Cirac, and M.-C. Bañuls. Algorithms for finite projected entangled pair states. *Phys. Rev. B*, 90:064425, doi:10.1103/PhysRevB.90.064425.

- [54] G. Vidal. Class of Quantum Many-Body States That Can Be Efficiently Simulated. *Phys. Rev. Lett.*, 101:110501, doi:10.1103/PhysRevLett.101.110501.
- [55] G. Evenbly and G. Vidal. Algorithms for entanglement renormalization. *Phys. Rev. B*, 79:144108, doi:10.1103/PhysRevB.79.144108.
- [56] G. Evenbly, R. N. C. Pfeifer, V. Picó, S. Iblisdir, L. Tagliacozzo, I. P. McCulloch, and G. Vidal. Boundary quantum critical phenomena with entanglement renormalization. *Phys. Rev. B*, 82:161107, doi:10.1103/PhysRevB.82.161107.
- [57] R. Orús. A practical introduction to tensor networks: Matrix product states and projected entangled pair states. *Annals of Physics*, 349:117–158, doi:<https://doi.org/10.1016/j.aop.2014.06.013>.
- [58] Y.-Y. Shi, L.-M. Duan, and G. Vidal. Classical simulation of quantum many-body systems with a tree tensor network. *Phys. Rev. A*, 74:022320, doi:10.1103/PhysRevA.74.022320.
- [59] P. Silvi, V. Giovannetti, S. Montangero, M. Rizzi, J. I. Cirac, and R. Fazio. Homogeneous binary trees as ground states of quantum critical Hamiltonians. *Phys. Rev. A*, 81:062335, doi:10.1103/PhysRevA.81.062335.
- [60] P. Czarnik and J. Dziarmaga. Variational approach to projected entangled pair states at finite temperature. *Phys. Rev. B*, 92:035152, doi:10.1103/PhysRevB.92.035152.
- [61] U. Schollwöck. The density-matrix renormalization group in the age of matrix product states. *Annals of Physics*, 326(1):96–192, doi:<https://doi.org/10.1016/j.aop.2010.09.012>.

- [62] F. Verstraete, J. J. García-Ripoll, and J. I. Cirac. Matrix Product Density Operators: Simulation of Finite-Temperature and Dissipative Systems. *Phys. Rev. Lett.*, 93:207204, doi:10.1103/PhysRevLett.93.207204.
- [63] N. Chepiga and S. R. White. Comb tensor networks. *Phys. Rev. B*, 99:235426, doi:10.1103/PhysRevB.99.235426.
- [64] R. A. Jishi. *Feynman diagram techniques in condensed matter physics*. Cambridge University Press, Cambridge, England, September 2014.
- [65] P. Coleman. *Introduction to many-body physics*. Cambridge University Press, Cambridge, England, August 2015.
- [66] A. Altland and B. D. Simons. *Condensed matter field theory*. Cambridge University Press, 2 edition, May 2014.
- [67] R. D. Mattuck. *A guide to Feynman diagrams in the many-body problem*. Dover Publications, August 2012.
- [68] F. Harris. *Algebraic and diagrammatic methods in many-fermion theory*. Dover Publications, Mineola, NY, February 2020.
- [69] G. D. Mahan. *Many-Particle Physics*. Springer, New York, NY, 2000.
- [70] A. L. Fetter and J. D. Walecka. *Quantum theory of many particle systems New York*. 1971.
- [71] E. G. C. P. van Loon, M. Rösner, M. I. Katsnelson, and T. O. Wehling. Random phase approximation for gapped systems: Role of vertex corrections and applicability of the constrained random phase approximation. *Phys. Rev. B*, 104:045134, doi:10.1103/PhysRevB.104.045134.

- [72] J. Schirmer. Beyond the random-phase approximation: A new approximation scheme for the polarization propagator. *Phys. Rev. A*, 26:2395–2416, doi:10.1103/PhysRevA.26.2395.
- [73] L. Hedin. New Method for Calculating the One-Particle Green’s Function with Application to the Electron-Gas Problem. *Phys. Rev.*, 139:A796–A823, doi:10.1103/PhysRev.139.A796.
- [74] F. Aryasetiawan and O. Gunnarsson. The GW method. *Reports on Progress in Physics*, 61(3):237, doi:10.1088/0034-4885/61/3/002.
- [75] N. V. Prokof’ev and B. V. Svistunov. Bold diagrammatic Monte Carlo: A generic sign-problem tolerant technique for polaron models and possibly interacting many-body problems. *Phys. Rev. B*, 77:125101, doi:10.1103/PhysRevB.77.125101.
- [76] K. Van Houcke, F. Werner, E. Kozik, N. Prokof’ev, B. Svistunov, M. J. H. Ku, A. T. Sommer, L. W. Cheuk, A. Schirotzek, and M. W. Zwierlein. Feynman diagrams versus Fermi-gas Feynman emulator. *Nat. Phys.*, 8(5):366–370, May 2012.
- [77] B. D. E. McNiven, G. T. Andrews, and J. P. F. LeBlanc. Single particle properties of the two-dimensional Hubbard model for real frequencies at weak coupling: Breakdown of the Dyson series for partial self-energy expansions. *Phys. Rev. B*, 104:125114, doi:10.1103/PhysRevB.104.125114.
- [78] E. Kozik, K. V. Houcke, E. Gull, L. Pollet, N. Prokof’ev, B. Svistunov, and M. Troyer. Diagrammatic Monte Carlo for correlated fermions. *Europhysics Letters*, 90(1):10004, doi:10.1209/0295-5075/90/10004.

- [79] A. N. Rubtsov, V. V. Savkin, and A. I. Lichtenstein. Continuous-time quantum Monte Carlo method for fermions. *Phys. Rev. B*, 72:035122, doi:10.1103/PhysRevB.72.035122.
- [80] E. Burovski, N. Prokof'ev, B. Svistunov, and M. Troyer. Critical Temperature and Thermodynamics of Attractive Fermions at Unitarity. *Phys. Rev. Lett.*, 96:160402, doi:10.1103/PhysRevLett.96.160402.
- [81] E. Gull, A. J. Millis, A. I. Lichtenstein, A. N. Rubtsov, M. Troyer, and P. Werner. Continuous-time Monte Carlo methods for quantum impurity models. *Rev. Mod. Phys.*, 83:349–404, doi:10.1103/RevModPhys.83.349.
- [82] R. Rossi. Determinant Diagrammatic Monte Carlo Algorithm in the Thermodynamic Limit. *Phys. Rev. Lett.*, 119:045701, doi:10.1103/PhysRevLett.119.045701.
- [83] A. Moutenet, W. Wu, and M. Ferrero. Determinant Monte Carlo algorithms for dynamical quantities in fermionic systems. *Phys. Rev. B*, 97:085117, doi:10.1103/PhysRevB.97.085117.
- [84] F. Š. IV and M. Ferrero. Fast principal minor algorithms for diagrammatic Monte Carlo. *Physical Review B*, 105(12), doi:10.1103/physrevb.105.125104.
- [85] R. Levy, J. LeBlanc, and E. Gull. Implementation of the maximum entropy method for analytic continuation. *Computer Physics Communications*, 215:149–155, doi:https://doi.org/10.1016/j.cpc.2017.01.018.
- [86] H. J. Vidberg and J. W. Serene. Solving the Eliashberg equations by means of N-point Pade approximants. *J. Low Temp. Phys.*, 29(3-4):179–192, November 1977.

- [87] J. Fei, C.-N. Yeh, D. Zgid, and E. Gull. Analytical continuation of matrix-valued functions: Carathéodory formalism. *Phys. Rev. B*, 104:165111, doi:10.1103/PhysRevB.104.165111.
- [88] A. Taheridehkordi, S. H. Curnoe, and J. P. F. LeBlanc. Algorithmic Matsubara integration for Hubbard-like models. *Phys. Rev. B*, 99:035120, doi:10.1103/PhysRevB.99.035120.
- [89] A. Taheridehkordi, S. H. Curnoe, and J. P. F. LeBlanc. Optimal grouping of arbitrary diagrammatic expansions via analytic pole structure. *Phys. Rev. B*, 101:125109, doi:10.1103/PhysRevB.101.125109.
- [90] A. Taheridehkordi, S. H. Curnoe, and J. P. F. LeBlanc. Algorithmic approach to diagrammatic expansions for real-frequency evaluation of susceptibility functions. *Phys. Rev. B*, 102:045115, doi:10.1103/PhysRevB.102.045115.
- [91] M. D. Burke, M. Grandadam, and J. P. F. LeBlanc. Renormalized perturbation theory for fast evaluation of Feynman diagrams on the real frequency axis. *Phys. Rev. B*, 107:115151, doi:10.1103/PhysRevB.107.115151.
- [92] I. S. Tupitsyn, A. M. Tsvelik, R. M. Konik, and N. V. Prokof'ev. Real-Frequency Response Functions at Finite Temperature. *Phys. Rev. Lett.*, 127:026403, doi:10.1103/PhysRevLett.127.026403.
- [93] J. P. F. LeBlanc, K. Chen, K. Haule, N. V. Prokof'ev, and I. S. Tupitsyn. Dynamic Response of an Electron Gas: Towards the Exact Exchange-Correlation Kernel. *Phys. Rev. Lett.*, 129:246401, doi:10.1103/PhysRevLett.129.246401.
- [94] I. Assi and J. P. F. LeBlanc. Symbolic determinant construction of perturbative expansions. *ArXiv*, 2305.09103, doi:https://doi.org/10.48550/arXiv.2305.09103.

- [95] D. N. Basov, R. D. Averitt, and D. Hsieh. "Towards properties on demand in quantum materials". *Nat. Mater.*, 16(11):1077–1088, October 2017.
- [96] J. H. Mentink and M. Eckstein. Ultrafast Quenching of the Exchange Interaction in a Mott Insulator. *Phys. Rev. Lett.*, 113:057201, doi:10.1103/PhysRevLett.113.057201.
- [97] A. Cavalleri. Photo-induced superconductivity. *Contemporary Physics*, 59(1):31–46, doi:10.1080/00107514.2017.1406623.
- [98] S. Choi, J. Choi, R. Landig, G. Kucsko, H. Zhou, J. Isoya, F. Jelezko, S. Onoda, H. Sumiya, V. Khemani, C. von Keyserlingk, N. Y. Yao, E. Demler, and M. D. Lukin. Observation of discrete time-crystalline order in a disordered dipolar many-body system. *Nature*, 543(7644):221–225, March 2017.
- [99] D. V. Else, B. Bauer, and C. Nayak. Prethermal Phases of Matter Protected by Time-Translation Symmetry. *Phys. Rev. X*, 7:011026, doi:10.1103/PhysRevX.7.011026.
- [100] V. Khemani, A. Lazarides, R. Moessner, and S. L. Sondhi. Phase Structure of Driven Quantum Systems. *Phys. Rev. Lett.*, 116:250401, doi:10.1103/PhysRevLett.116.250401.
- [101] A. C. Potter, T. Morimoto, and A. Vishwanath. Classification of Interacting Topological Floquet Phases in One Dimension. *Phys. Rev. X*, 6:041001, doi:10.1103/PhysRevX.6.041001.
- [102] J. W. McIver, B. Schulte, F.-U. Stein, T. Matsuyama, G. Jotzu, G. Meier, and A. Cavalleri. Light-induced anomalous Hall effect in graphene. *Nat. Phys.*, 16(1):38–41, January 2020.

- [103] L. Stojchevska, I. Vaskivskiy, T. Mertelj, P. Kusar, D. Svetin, S. Brazovskii, and D. Mihailovic. Ultrafast switching to a stable hidden quantum state in an electronic crystal. *Science*, 344(6180):177–180, April 2014.
- [104] Y. A. Gerasimenko, P. Karpov, I. Vaskivskiy, S. Brazovskii, and D. Mihailovic. Intertwined chiral charge orders and topological stabilization of the light-induced state of a prototypical transition metal dichalcogenide. *Npj Quantum Mater.*, 4(1), June 2019.
- [105] P. Helms and G. K.-L. Chan. Dynamical Phase Transitions in a 2D Classical Nonequilibrium Model via 2D Tensor Networks. *Phys. Rev. Lett.*, 125:140601, doi:10.1103/PhysRevLett.125.140601.
- [106] D. M. Fugger, D. Bauernfeind, M. E. Sorantin, and E. Arrigoni. Nonequilibrium pseudogap Anderson impurity model: A master equation tensor network approach. *Phys. Rev. B*, 101:165132, doi:10.1103/PhysRevB.101.165132.
- [107] T. Prosen. Exact Nonequilibrium Steady State of a Strongly Driven Open XXZ Chain. *Phys. Rev. Lett.*, 107:137201, doi:10.1103/PhysRevLett.107.137201.
- [108] E. Gillman, F. Carollo, and I. Lesanovsky. Numerical simulation of quantum nonequilibrium phase transitions without finite-size effects. *Phys. Rev. A*, 103:L040201, doi:10.1103/PhysRevA.103.L040201.
- [109] A. M. Alhambra and J. I. Cirac. Locally Accurate Tensor Networks for Thermal States and Time Evolution. *PRX Quantum*, 2:040331, doi:10.1103/PRXQuantum.2.040331.
- [110] M. Brenes, J. J. Mendoza-Arenas, A. Purkayastha, M. T. Mitchison, S. R. Clark, and J. Goold. Tensor-Network Method to Simulate

- Strongly Interacting Quantum Thermal Machines. *Phys. Rev. X*, 10:031040, doi:10.1103/PhysRevX.10.031040.
- [111] Y. Yoo, J. Lee, and B. Swingle. Nonequilibrium steady state phases of the interacting Aubry-André-Harper model. *Phys. Rev. B*, 102:195142, doi:10.1103/PhysRevB.102.195142.
- [112] S. R. White and A. E. Feiguin. Real-Time Evolution Using the Density Matrix Renormalization Group. *Phys. Rev. Lett.*, 93:076401, doi:10.1103/PhysRevLett.93.076401.
- [113] A. J. Daley, C. Kollath, U. Schollwöck, and G. Vidal. Time-dependent density-matrix renormalization-group using adaptive effective Hilbert spaces. *Journal of Statistical Mechanics: Theory and Experiment*, 2004(04):P04005, doi:10.1088/1742-5468/2004/04/P04005.
- [114] P. Schmitteckert. Nonequilibrium electron transport using the density matrix renormalization group method. *Phys. Rev. B*, 70:121302, doi:10.1103/PhysRevB.70.121302.
- [115] D. N. Basov, R. D. Averitt, D. van der Marel, M. Dressel, and K. Haule. Electrodynamics of correlated electron materials. *Rev. Mod. Phys.*, 83:471–541, doi:10.1103/RevModPhys.83.471.
- [116] C. Giannetti, M. Capone, D. Fausti, M. Fabrizio, F. Parmigiani, and D. Mihailovic. Ultrafast optical spectroscopy of strongly correlated materials and high-temperature superconductors: a non-equilibrium approach. *Adv. Phys.*, 65(2):58–238, March 2016.
- [117] J. Zhang and R. D. Averitt. Dynamics and control in complex transition metal oxides. *Annu. Rev. Mater. Res.*, 44(1):19–43, July 2014.

- [118] V. Špička, P. D. Keefe, and T. M. Nieuwenhuizen. Non-equilibrium systems and foundations of quantum physics. *Eur. Phys. J. Spec. Top.*, 230(4):729–731, June 2021.
- [119] S. R. Barone, M. A. Narcowich, and F. J. Narcowich. Floquet theory and applications. *Phys. Rev. A*, 15:1109–1125, doi:10.1103/PhysRevA.15.1109.
- [120] W. Magnus. On the exponential solution of differential equations for a linear operator. *Commun. Pure Appl. Math.*, 7(4):649–673, November 1954.
- [121] M. M. Maricq. Application of average Hamiltonian theory to the NMR of solids. *Phys. Rev. B*, 25:6622–6632, doi:10.1103/PhysRevB.25.6622.
- [122] T. Mikami, S. Kitamura, K. Yasuda, N. Tsuji, T. Oka, and H. Aoki. Brillouin-Wigner theory for high-frequency expansion in periodically driven systems: Application to Floquet topological insulators. *Phys. Rev. B*, 93:144307, doi:10.1103/PhysRevB.93.144307.
- [123] S. Rahav, I. Gilary, and S. Fishman. Effective Hamiltonians for periodically driven systems. *Phys. Rev. A*, 68:013820, doi:10.1103/PhysRevA.68.013820.
- [124] S. Blanes, F. Casas, J. A. Oteo, and J. Ros. The Magnus expansion and some of its applications. *Phys. Rep.*, 470(5-6):151–238, January 2009.
- [125] M. S. Rudner and N. H. Lindner. Floquet topological insulators: from band structure engineering to novel non-equilibrium quantum phenomena, 2019.
- [126] Z. Gu, H. A. Fertig, D. P. Arovas, and A. Auerbach. Floquet spectrum and transport through an irradiated graphene ribbon. June 2011.
- [127] T. Oka and H. Aoki. Photovoltaic Hall effect in graphene. *Phys. Rev. B*, 79:081406, doi:10.1103/PhysRevB.79.081406.

- [128] G. Usaj, P. M. Perez-Piskunow, L. E. F. Foa Torres, and C. A. Balseiro. Irradiated graphene as a tunable Floquet topological insulator. *Phys. Rev. B*, 90:115423, doi:10.1103/PhysRevB.90.115423.
- [129] A. K. Geim and I. V. Grigorieva. Van der Waals heterostructures. *Nature*, 499(7459):419–425, July 2013.
- [130] K. S. Novoselov, A. Mishchenko, A. Carvalho, and A. H. C. Neto. 2D materials and van der Waals heterostructures. August 2016.
- [131] D. V. Chichinadze, L. Classen, and A. V. Chubukov. Nematic superconductivity in twisted bilayer graphene. *Phys. Rev. B*, 101:224513, doi:10.1103/PhysRevB.101.224513.
- [132] Y.-Z. Chou, Y.-P. Lin, S. Das Sarma, and R. M. Nandkishore. Superconductor versus insulator in twisted bilayer graphene. *Phys. Rev. B*, 100:115128, doi:10.1103/PhysRevB.100.115128.
- [133] E. Codecido, Q. Wang, R. Koester, S. Che, H. Tian, R. Lv, S. Tran, K. Watanabe, T. Taniguchi, F. Zhang, M. Bockrath, and C. N. Lau. Correlated insulating and superconducting states in twisted bilayer graphene below the magic angle. *Science Advances*, 5(9):eaaw9770, doi:10.1126/sciadv.aaw9770.
- [134] H. C. Po, L. Zou, A. Vishwanath, and T. Senthil. Origin of Mott Insulating Behavior and Superconductivity in Twisted Bilayer Graphene. *Phys. Rev. X*, 8:031089, doi:10.1103/PhysRevX.8.031089.
- [135] S. Ray, J. Jung, and T. Das. Wannier pairs in superconducting twisted bilayer graphene and related systems. *Phys. Rev. B*, 99:134515, doi:10.1103/PhysRevB.99.134515.

- [136] Y. Saito, J. Ge, K. Watanabe, T. Taniguchi, and A. F. Young. Independent superconductors and correlated insulators in twisted bilayer graphene. *Nat. Phys.*, 16(9):926–930, September 2020.
- [137] Y. Sherkunov and J. J. Betouras. Electronic phases in twisted bilayer graphene at magic angles as a result of Van Hove singularities and interactions. *Phys. Rev. B*, 98:205151, doi:10.1103/PhysRevB.98.205151.
- [138] J. W. F. Venderbos and R. M. Fernandes. Correlations and electronic order in a two-orbital honeycomb lattice model for twisted bilayer graphene. *Phys. Rev. B*, 98:245103, doi:10.1103/PhysRevB.98.245103.
- [139] G. E. Volovik. Graphite, graphene, and the flat band superconductivity. *JETP Lett.*, 107(8):516–517, April 2018.
- [140] M. Yankowitz, S. Chen, H. Polshyn, Y. Zhang, K. Watanabe, T. Taniguchi, D. Graf, A. F. Young, and C. R. Dean. Tuning superconductivity in twisted bilayer graphene. *Science*, 363(6431):1059–1064, doi:10.1126/science.aav1910.
- [141] R. Bistritzer and A. H. MacDonald. Moiré bands in twisted double-layer graphene. *Proceedings of the National Academy of Sciences*, 108(30):12233–12237, doi:10.1073/pnas.1108174108.
- [142] D. Weckbecker, S. Shallcross, M. Fleischmann, N. Ray, S. Sharma, and O. Pankratov. Low-energy theory for the graphene twist bilayer. *Phys. Rev. B*, 93:035452, doi:10.1103/PhysRevB.93.035452.
- [143] G. E. Topp, G. Jotzu, J. W. McIver, L. Xian, A. Rubio, and M. A. Sentef. Topological Floquet engineering of twisted bilayer graphene. *Phys. Rev. Res.*, 1:023031, doi:10.1103/PhysRevResearch.1.023031.

- [144] Y. Li, H. A. Fertig, and B. Seradjeh. Floquet-engineered topological flat bands in irradiated twisted bilayer graphene. *Phys. Rev. Res.*, 2:043275, doi:10.1103/PhysRevResearch.2.043275.
- [145] M. Vogl, M. Rodriguez-Vega, and G. A. Fiete. Floquet engineering of interlayer couplings: Tuning the magic angle of twisted bilayer graphene at the exit of a waveguide. *Phys. Rev. B*, 101:241408, doi:10.1103/PhysRevB.101.241408.
- [146] M. Vogl, M. Rodriguez-Vega, B. Flebus, A. H. MacDonald, and G. A. Fiete. Floquet engineering of topological transitions in a twisted transition metal dichalcogenide homobilayer. *Phys. Rev. B*, 103:014310, doi:10.1103/PhysRevB.103.014310.
- [147] M. Vogl, S. Chaudhary, and G. A. Fiete. Light driven magnetic transitions in transition metal dichalcogenide heterobilayers. *Journal of Physics: Condensed Matter*, 35(9):095801, doi:10.1088/1361-648X/acab49.
- [148] G.-B. Zhu, H.-M. Yang, and J. Yang. Longitudinal conductivity in ABC-stacked trilayer graphene under irradiating of linearly polarized light. *Chinese Physics B*, 31(8):088102, doi:10.1088/1674-1056/ac7205.
- [149] Y. Li, A. Eaton, H. A. Fertig, and B. Seradjeh. Dirac Magic and Lifshitz Transitions in AA-Stacked Twisted Multilayer Graphene. *Phys. Rev. Lett.*, 128:026404, doi:10.1103/PhysRevLett.128.026404.
- [150] K. Van Houcke, F. Werner, E. Kozik, N. Prokof'ev, B. Svistunov, M. J. H. Ku, A. T. Sommer, L. W. Cheuk, A. Schirotzek, and M. W. Zwierlein. *Nature Physics*, 8:366, 2012.

- [151] K. Chen and K. Haule. A combined variational and diagrammatic quantum Monte Carlo approach to the many-electron problem. *Nature communications*, 10(1):3725–3725, doi:10.1038/s41467-019-11708-6.
- [152] H. Elazab, B. McNiven, and J. LeBlanc. LIBAMI: Implementation of algorithmic Matsubara integration. *Computer Physics Communications*, 280:108469, doi:https://doi.org/10.1016/j.cpc.2022.108469.
- [153] B. D. E. McNiven, H. Terletska, G. T. Andrews, and J. P. F. LeBlanc. One- and two-particle properties of the weakly interacting two-dimensional Hubbard model in proximity to the van Hove singularity. *Phys. Rev. B*, 106:035145, doi:10.1103/PhysRevB.106.035145.
- [154] R. Levy, J. P. F. LeBlanc, and E. Gull. Implementation of the Maximum Entropy Method for Analytic Continuation. *Comp. Phys. Comm.*, 215:149, doi:10.1016/j.cpc.2017.01.018.
- [155] F. Šimkovic, J. P. F. LeBlanc, A. J. Kim, Y. Deng, N. V. Prokof'ev, B. V. Svistunov, and E. Kozik. Extended Crossover from a Fermi Liquid to a Quasiantiferromagnet in the Half-Filled 2D Hubbard Model. *Phys. Rev. Lett.*, 124:017003, doi:10.1103/PhysRevLett.124.017003.
- [156] R. Rossi, F. Werner, N. Prokof'ev, and B. Svistunov. Shifted-action expansion and applicability of dressed diagrammatic schemes. *Phys. Rev. B*, 93:161102, doi:10.1103/PhysRevB.93.161102.
- [157] R. Rossi, T. Ohgoe, K. Van Houcke, and F. Werner. Resummation of Diagrammatic Series with Zero Convergence Radius for Strongly Correlated Fermions. *Phys. Rev. Lett.*, 121:130405, doi:10.1103/PhysRevLett.121.130405.

- [158] S. Hirata, M. R. Hermes, J. Simons, and J. V. Ortiz. General-Order Many-Body Green’s Function Method. *Journal of Chemical Theory and Computation*, 11(4):1595–1606, doi:10.1021/acs.jctc.5b00005.
- [159] Kris Van Houcke and Evgeny Kozik and N. Prokof’ev and B. Svistunov. *Physics Procedia*, 6:95–105, 2010.
- [160] K. Van Houcke and F. Werner and E. Kozik and N. Prokof’ev and B. Svistunov and M. J. H. Ku and A. T. Sommer and L. W. Cheuk and A. Schirotzek and M. W. Zwierlein . *Nature Physics*, 8:366, 2012.
- [161] Q. Sun, T. C. Berkelbach, N. S. Blunt, G. H. Booth, S. Guo, Z. Li, J. Liu, J. D. McClain, E. R. Sayfutyarova, S. Sharma, S. Wouters, and G. K.-L. Chan. PySCF: the Python-based simulations of chemistry framework. *WIREs Computational Molecular Science*, 8(1):e1340, doi:https://doi.org/10.1002/wcms.1340.
- [162] A. Fischer, Z. A. H. Goodwin, A. A. Mostofi, J. Lischner, D. M. Kennes, and L. Klebl. Unconventional superconductivity in magic-angle twisted trilayer graphene. *Npj Quantum Mater.*, 7(1), January 2022.
- [163] A. Ramires and J. L. Lado. Emulating Heavy Fermions in Twisted Trilayer Graphene. *Phys. Rev. Lett.*, 127:026401, doi:10.1103/PhysRevLett.127.026401.
- [164] M. Koshino, N. F. Q. Yuan, T. Koretsune, M. Ochi, K. Kuroki, and L. Fu. Maximally Localized Wannier Orbitals and the Extended Hubbard Model for Twisted Bilayer Graphene. *Phys. Rev. X*, 8:031087, doi:10.1103/PhysRevX.8.031087.
- [165] M. Rodriguez-Vega, M. Vogl, and G. A. Fiete. Low-frequency and Moiré–Floquet engineering: A review. *Annals of Physics*, 435:168434, doi:https://doi.org/10.1016/j.aop.2021.168434.

- [166] F. Mahmood, C.-K. Chan, Z. Alpichshev, D. Gardner, Y. Lee, P. A. Lee, and N. Gedik. Selective scattering between Floquet–Bloch and Volkov states in a topological insulator. *Nat. Phys.*, 12(4):306–310, April 2016.
- [167] Y. H. Wang, H. Steinberg, P. Jarillo-Herrero, and N. Gedik. Observation of Floquet-Bloch states on the surface of a topological insulator. *Science*, 342(6157):453–457, October 2013.
- [168] A. Eckardt and E. Anisimovas. High-frequency approximation for periodically driven quantum systems from a Floquet-space perspective. *New Journal of Physics*, 17(9):093039, doi:10.1088/1367-2630/17/9/093039.
- [169] M. Vogl, M. Rodriguez-Vega, and G. A. Fiete. Effective Floquet Hamiltonians for periodically driven twisted bilayer graphene. *Phys. Rev. B*, 101:235411, doi:10.1103/PhysRevB.101.235411.
- [170] W.-J. Zuo, J.-B. Qiao, D.-L. Ma, L.-J. Yin, G. Sun, J.-Y. Zhang, L.-Y. Guan, and L. He. Scanning tunneling microscopy and spectroscopy of twisted trilayer graphene. *Phys. Rev. B*, 97:035440, doi:10.1103/PhysRevB.97.035440.
- [171] R. Bistritzer and A. H. MacDonald. Moiré bands in twisted double-layer graphene. *Proc. Natl. Acad. Sci. U. S. A.*, 108(30):12233–12237, July 2011.
- [172] J. Custers, P. Gegenwart, H. Wilhelm, K. Neumaier, Y. Tokiwa, O. Trovarelli, C. Geibel, F. Steglich, C. Pépin, and P. Coleman. The break-up of heavy electrons at a quantum critical point. *Nature*, 424(6948):524–527, July 2003.
- [173] T.-H. Han, J. S. Helton, S. Chu, D. G. Nocera, J. A. Rodriguez-Rivera, C. Broholm, and Y. S. Lee. Fractionalized excitations in the spin-liquid state of a kagome-lattice antiferromagnet. *Nature*, 492(7429):406–410, December 2012.

- [174] A. Mazurenko, C. S. Chiu, G. Ji, M. F. Parsons, M. Kanász-Nagy, R. Schmidt, F. Grusdt, E. Demler, D. Greif, and M. Greiner. A cold-atom Fermi-Hubbard antiferromagnet. *Nature*, 545(7655):462–466, May 2017.
- [175] Y. Cao, V. Fatemi, S. Fang, K. Watanabe, T. Taniguchi, E. Kaxiras, and P. Jarillo-Herrero. Unconventional superconductivity in magic-angle graphene superlattices. *Nature*, 556(7699):43–50, April 2018.
- [176] Y. Cao, D. Rodan-Legrain, O. Rubies-Bigorda, J. M. Park, K. Watanabe, T. Taniguchi, and P. Jarillo-Herrero. Tunable correlated states and spin-polarized phases in twisted bilayer-bilayer graphene. *Nature*, 583(7815):215–220, July 2020.
- [177] C. Shen, Y. Chu, Q. Wu, N. Li, S. Wang, Y. Zhao, J. Tang, J. Liu, J. Tian, K. Watanabe, T. Taniguchi, R. Yang, Z. Y. Meng, D. Shi, O. V. Yazyev, and G. Zhang. Correlated states in twisted double bilayer graphene. *Nat. Phys.*, 16(5):520–525, May 2020.
- [178] X. Liu, Z. Hao, E. Khalaf, J. Y. Lee, Y. Ronen, H. Yoo, D. Haei Najafabadi, K. Watanabe, T. Taniguchi, A. Vishwanath, and P. Kim. Tunable spin-polarized correlated states in twisted double bilayer graphene. *Nature*, 583(7815):221–225, July 2020.
- [179] N. R. Chebrolu, B. L. Chittari, and J. Jung. Flat bands in twisted double bilayer graphene. *Phys. Rev. B*, 99:235417, doi:10.1103/PhysRevB.99.235417.
- [180] M. Koshino. Band structure and topological properties of twisted double bilayer graphene. *Phys. Rev. B*, 99:235406, doi:10.1103/PhysRevB.99.235406.

- [181] J. Y. Lee, E. Khalaf, S. Liu, X. Liu, Z. Hao, P. Kim, and A. Vishwanath. Theory of correlated insulating behaviour and spin-triplet superconductivity in twisted double bilayer graphene. *Nat. Commun.*, 10(1):5333, November 2019.
- [182] F. Haddadi, Q. Wu, A. J. Kruchkov, and O. V. Yazyev. Moiré Flat Bands in Twisted Double Bilayer Graphene. *Nano Letters*, 20(4):2410–2415, doi:10.1021/acs.nanolett.9b05117.
- [183] F. J. Culchac, R. R. Del Grande, R. B. Capaz, L. Chico, and E. S. Morell. Flat bands and gaps in twisted double bilayer graphene. *Nanoscale*, 12(8):5014–5020, February 2020.
- [184] Y.-H. Zhang, D. Mao, Y. Cao, P. Jarillo-Herrero, and T. Senthil. Nearly flat Chern bands in moiré superlattices. *Phys. Rev. B*, 99:075127, doi:10.1103/PhysRevB.99.075127.
- [185] A. Kerelsky, C. Rubio-Verdú, L. Xian, D. M. Kennes, D. Halbertal, N. Finney, L. Song, S. Turkel, L. Wang, K. Watanabe, T. Taniguchi, J. Hone, C. Dean, D. N. Basov, A. Rubio, and A. N. Pasupathy. Moiréless correlations in ABCA graphene. *Proc. Natl. Acad. Sci. U. S. A.*, 118(4):e2017366118, January 2021.
- [186] C. Rubio-Verdú, S. Turkel, L. Song, L. Klebl, R. Samajdar, M. S. Scheurer, and Pasupathy. *Universal moiré nematic phase in twisted graphitic systems*. 2020.
- [187] D. Halbertal, N. R. Finney, S. S. Sunku, A. Kerelsky, C. Rubio-Verdú, S. Shabani, L. Xian, S. Carr, S. Chen, C. Zhang, L. Wang, D. Gonzalez-Acevedo, A. S. McLeod, D. Rhodes, K. Watanabe, T. Taniguchi, E. Kaxiras, C. R. Dean, J. C. Hone, A. N. Pasupathy, D. M. Kennes, A. Rubio, and D. N. Basov. Moiré metrology of energy landscapes in van der Waals heterostructures. *Nat. Commun.*, 12(1):242, January 2021.

- [188] M. Christos, S. Sachdev, and M. S. Scheurer. Correlated Insulators, Semimetals, and Superconductivity in Twisted Trilayer Graphene. *Phys. Rev. X*, 12:021018, doi:10.1103/PhysRevX.12.021018.
- [189] E. Codecido, Q. Wang, R. Koester, S. Che, H. Tian, R. Lv, S. Tran, K. Watanabe, T. Taniguchi, F. Zhang, M. Bockrath, and C. N. Lau. Correlated insulating and superconducting states in twisted bilayer graphene below the magic angle. *Sci. Adv.*, 5(9):eaaw9770, September 2019.
- [190] D. Wong, K. P. Nuckolls, M. Oh, B. Lian, Y. Xie, S. Jeon, K. Watanabe, T. Taniguchi, B. A. Bernevig, and A. Yazdani. Cascade of electronic transitions in magic-angle twisted bilayer graphene. *Nature*, 582(7811):198–202, June 2020.
- [191] X. Lu, P. Stepanov, W. Yang, M. Xie, M. A. Aamir, I. Das, C. Urgell, K. Watanabe, T. Taniguchi, G. Zhang, A. Bachtold, A. H. MacDonald, and D. K. Efetov. Superconductors, orbital magnets and correlated states in magic-angle bilayer graphene. *Nature*, 574(7780):653–657, October 2019.
- [192] A. L. Sharpe, E. J. Fox, A. W. Barnard, J. Finney, K. Watanabe, T. Taniguchi, M. A. Kastner, and D. Goldhaber-Gordon. Emergent ferromagnetism near three-quarters filling in twisted bilayer graphene. *Science*, 365(6453):605–608, doi:10.1126/science.aaw3780.
- [193] T. Oka and S. Kitamura. Floquet engineering of quantum materials. *Annu. Rev. Condens. Matter Phys.*, 10(1):387–408, March 2019.
- [194] M. S. Rudner and N. H. Lindner. Band structure engineering and non-equilibrium dynamics in Floquet topological insulators. *Nat. Rev. Phys.*, 2(5):229–244, May 2020.

- [195] N. H. Lindner, G. Refael, and V. Galitski. Floquet topological insulator in semiconductor quantum wells. *Nat. Phys.*, 7(6):490–495, June 2011.
- [196] M. Luo. Tuning of a bilayer graphene heterostructure by horizontally incident circular polarized light. *Phys. Rev. B*, 103:195422, doi:10.1103/PhysRevB.103.195422.
- [197] O. V. Kibis, S. Morina, K. Dini, and I. A. Shelykh. Magneto-electronic properties of graphene dressed by a high-frequency field. *Phys. Rev. B*, 93:115420, doi:10.1103/PhysRevB.93.115420.
- [198] M. Bukov, L. D’Alessio, and A. Polkovnikov. Universal high-frequency behavior of periodically driven systems: from dynamical stabilization to Floquet engineering. *Adv. Phys.*, 64(2):139–226, March 2015.
- [199] E. Fel’dman. On the convergence of the magnus expansion for spin systems in periodic magnetic fields. *Physics Letters A*, 104(9):479–481, doi:https://doi.org/10.1016/0375-9601(84)90027-6.
- [200] D. A. Abanin, W. De Roeck, W. W. Ho, and F. m. c. Huveneers. Effective Hamiltonians, prethermalization, and slow energy absorption in periodically driven many-body systems. *Phys. Rev. B*, 95:014112, doi:10.1103/PhysRevB.95.014112.
- [201] A. Gómez-León and G. Platero. Floquet-Bloch Theory and Topology in Periodically Driven Lattices. *Phys. Rev. Lett.*, 110:200403, doi:10.1103/PhysRevLett.110.200403.
- [202] M. Vogl, P. Laurell, A. D. Barr, and G. A. Fiete. Flow Equation Approach to Periodically Driven Quantum Systems. *Phys. Rev. X*, 9:021037, doi:10.1103/PhysRevX.9.021037.

- [203] O. Katz, G. Refael, and N. H. Lindner. Optically induced flat bands in twisted bilayer graphene. *Phys. Rev. B*, 102:155123, doi:10.1103/PhysRevB.102.155123.
- [204] M. Rodriguez-Vega, M. Vogl, and G. A. Fiete. Floquet engineering of twisted double bilayer graphene. *Phys. Rev. Res.*, 2:033494, doi:10.1103/PhysRevResearch.2.033494.
- [205] M. Lu, J. Zeng, H. Liu, J.-H. Gao, and X. C. Xie. Valley-selective Floquet Chern flat bands in twisted multilayer graphene. *Phys. Rev. B*, 103:195146, doi:10.1103/PhysRevB.103.195146.
- [206] J. M. Park, Y. Cao, K. Watanabe, T. Taniguchi, and P. Jarillo-Herrero. Tunable strongly coupled superconductivity in magic-angle twisted trilayer graphene. *Nature*, 590(7845):249–255, February 2021.
- [207] E. Khalaf, A. J. Kruchkov, G. Tarnopolsky, and A. Vishwanath. Magic angle hierarchy in twisted graphene multilayers. *Phys. Rev. B*, 100:085109, doi:10.1103/PhysRevB.100.085109.
- [208] X. Li, F. Wu, and A. H. MacDonald. Electronic Structure of Single-Twist Trilayer Graphene, 2019.
- [209] E. McCann. *Electronic Properties of Monolayer and Bilayer Graphene*, pages 237–275. Springer Berlin Heidelberg, Berlin, Heidelberg, 2012.
- [210] P. Kumar, T. M. Herath, and V. Apalkov. Bilayer graphene in strong ultrafast laser fields. *J. Phys. Condens. Matter*, 33(33):335305, June 2021.
- [211] T. Fukui, Y. Hatsugai, and H. Suzuki. Chern numbers in discretized brillouin zone: Efficient method of computing (spin) hall conductances. *J. Phys. Soc. Jpn.*, 74(6):1674–1677, June 2005.

- [212] H. Dehghani, T. Oka, and A. Mitra. Out-of-equilibrium electrons and the Hall conductance of a Floquet topological insulator. *Phys. Rev. B*, 91:155422, doi:10.1103/PhysRevB.91.155422.
- [213] A. Kumar, M. Rodriguez-Vega, T. Pereg-Barnea, and B. Seradjeh. Linear response theory and optical conductivity of Floquet topological insulators. *Phys. Rev. B*, 101:174314, doi:10.1103/PhysRevB.101.174314.
- [214] G. Tarnopolsky, A. J. Kruchkov, and A. Vishwanath. Origin of Magic Angles in Twisted Bilayer Graphene. *Phys. Rev. Lett.*, 122:106405, doi:10.1103/PhysRevLett.122.106405.
- [215] K. v. Klitzing, G. Dorda, and M. Pepper. New Method for High-Accuracy Determination of the Fine-Structure Constant Based on Quantized Hall Resistance. *Phys. Rev. Lett.*, 45:494–497, doi:10.1103/PhysRevLett.45.494.
- [216] F. D. M. Haldane. Model for a Quantum Hall Effect without Landau Levels: Condensed-Matter Realization of the "Parity Anomaly". *Phys. Rev. Lett.*, 61:2015–2018, doi:10.1103/PhysRevLett.61.2015.
- [217] C.-Z. Chang, J. Zhang, X. Feng, J. Shen, Z. Zhang, M. Guo, K. Li, Y. Ou, P. Wei, L.-L. Wang, Z.-Q. Ji, Y. Feng, S. Ji, X. Chen, J. Jia, X. Dai, Z. Fang, S.-C. Zhang, K. He, Y. Wang, L. Lu, X.-C. Ma, and Q.-K. Xue. Experimental observation of the quantum anomalous Hall effect in a magnetic topological insulator. *Science*, 340(6129):167–170, April 2013.
- [218] G. Jotzu, M. Messer, R. Desbuquois, M. Lebrat, T. Uehlinger, D. Greif, and T. Esslinger. Experimental realization of the topological Haldane model with ultracold fermions. *Nature*, 515(7526):237–240, November 2014.

- [219] K. Van Houcke, E. Kozik, N. Prokof'ev, and B. Svistunov. Diagrammatic Monte Carlo. *Physics Procedia*, 6:95–105, doi:<https://doi.org/10.1016/j.phpro.2010.09.034>.
- [220] Y. Zhang and J. Callaway. Extended Hubbard model in two dimensions. *Phys. Rev. B*, 39:9397–9404, doi:10.1103/PhysRevB.39.9397.
- [221] H. Terletska, T. Chen, and E. Gull. Charge ordering and correlation effects in the extended Hubbard model. *Phys. Rev. B*, 95:115149, doi:10.1103/PhysRevB.95.115149.
- [222] F. Ferrari, F. Becca, and R. Valentí. Charge density waves in kagome-lattice extended Hubbard models at the van Hove filling. *Phys. Rev. B*, 106:L081107, doi:10.1103/PhysRevB.106.L081107.
- [223] K. Ferhat and A. Ralko. Phase diagram of the $\frac{1}{3}$ -filled extended Hubbard model on the kagome lattice. *Phys. Rev. B*, 89:155141, doi:10.1103/PhysRevB.89.155141.
- [224] P. Pokhilko, C.-N. Yeh, and D. Zgid. Iterative subspace algorithms for finite-temperature solution of Dyson equation. *The Journal of Chemical Physics*, 156(9), doi:10.1063/5.0082586.
- [225] P. Pokhilko, S. Iskakov, C.-N. Yeh, and D. Zgid. Evaluation of two-particle properties within finite-temperature self-consistent one-particle Green's function methods: Theory and application to GW and GF2. *The Journal of Chemical Physics*, 155(2), doi:10.1063/5.0054661.
- [226] G. Bighin, Q. P. Ho, M. Lemeshko, and T. V. Tscherbul. Diagrammatic Monte Carlo for electronic correlation in molecules: high-order many-body perturbation theory with low scaling, 2022.

- [227] S. Hirata, M. R. Hermes, J. Simons, and J. V. Ortiz. General-order many-body green's function method. *J. Chem. Theory Comput.*, 11(4):1595–1606, April 2015.
- [228] N. Elstner and H. Monien. Dynamics and thermodynamics of the Bose-Hubbard model. *Phys. Rev. B*, 59:12184–12187, doi:10.1103/PhysRevB.59.12184.
- [229] B. Capogrosso-Sansone, i. m. c. G. m. c. Söyler, N. Prokof'ev, and B. Svistunov. Monte Carlo study of the two-dimensional Bose-Hubbard model. *Phys. Rev. A*, 77:015602, doi:10.1103/PhysRevA.77.015602.
- [230] D. Rossini and R. Fazio. Phase diagram of the extended Bose-Hubbard model. *New Journal of Physics*, 14(6):065012, doi:10.1088/1367-2630/14/6/065012.
- [231] C. Kollath, G. Roux, G. Biroli, and A. M. Läuchli. Statistical properties of the spectrum of the extended Bose-Hubbard model. *Journal of Statistical Mechanics: Theory and Experiment*, 2010(08):P08011, doi:10.1088/1742-5468/2010/08/P08011.
- [232] S. H. Curnoe. Exchange interactions in two-state systems: rare earth pyrochlores. *Journal of Physics: Condensed Matter*, 30(23):235803, doi:10.1088/1361-648X/aac061.
- [233] S. H. Curnoe. Structural distortion and the spin liquid state in $\text{Tb}_2\text{Ti}_2\text{O}_7$. *Phys. Rev. B*, 78:094418, doi:10.1103/PhysRevB.78.094418.
- [234] S. Onoda and Y. Tanaka. Quantum Melting of Spin Ice: Emergent Cooperative Quadrupole and Chirality. *Phys. Rev. Lett.*, 105:047201, doi:10.1103/PhysRevLett.105.047201.

- [235] J. G. Rau and M. J. Gingras. Frustrated Quantum Rare-Earth Pyrochlores. *Annual Review of Condensed Matter Physics*, 10(1):357–386, doi:10.1146/annurev-conmatphys-022317-110520.
- [236] M. Vogl, P. Laurell, H. Zhang, S. Okamoto, and G. A. Fiete. Resummation of the Holstein-Primakoff expansion and differential equation approach to operator square roots. *Phys. Rev. Res.*, 2:043243, doi:10.1103/PhysRevResearch.2.043243.
- [237] H. Pan, F. Wu, and S. Das Sarma. Quantum phase diagram of a Moiré-Hubbard model. *Phys. Rev. B*, 102:201104, doi:10.1103/PhysRevB.102.201104.
- [238] F. Wu, T. Lovorn, E. Tutuc, and A. H. MacDonald. Hubbard Model Physics in Transition Metal Dichalcogenide Moiré Bands. *Phys. Rev. Lett.*, 121:026402, doi:10.1103/PhysRevLett.121.026402.
- [239] N. Morales-Durán, N. C. Hu, P. Potasz, and A. H. MacDonald. Nonlocal Interactions in Moiré Hubbard Systems. *Phys. Rev. Lett.*, 128:217202, doi:10.1103/PhysRevLett.128.217202.
- [240] T. Shirai, J. Thingna, T. Mori, S. Denisov, P. Hänggi, and S. Miyashita. Effective Floquet–Gibbs states for dissipative quantum systems. *New Journal of Physics*, 18(5):053008, doi:10.1088/1367-2630/18/5/053008.
- [241] T. N. Ikeda, K. Chinzei, and M. Sato. Nonequilibrium steady states in the Floquet-Lindblad systems: van Vleck’s high-frequency expansion approach. *SciPost Phys. Core*, 4:033, doi:10.21468/SciPostPhysCore.4.4.033.
- [242] G. Engelhardt, G. Platero, and J. Cao. Discontinuities in Driven Spin-Boson Systems due to Coherent Destruction of Tunneling: Break-

down of the Floquet-Gibbs Distribution. *Phys. Rev. Lett.*, 123:120602,
doi:10.1103/PhysRevLett.123.120602.